Thesis

Phonon and electronic structure of monolayer graphite formed on transition-metal carbide and metal surfaces

和訳: 遷移金属炭化物および金属の表面上に形成された単原子層グラファイトのフォノン及び電子構造の研究

1994

Takashi Aizawa

相澤 俊

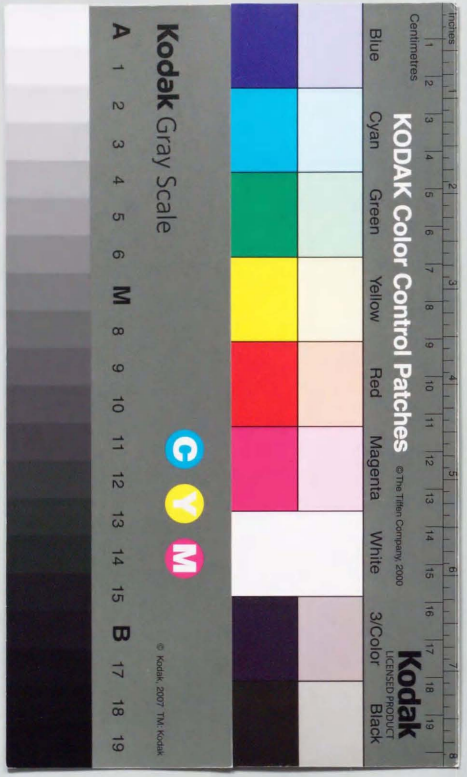

Phonon and electronic structure of monolayer graphite formed on transition-metal carbide and metal surfaces

Takashi Aizawa

National Institute for Research in Inorganic Materials
1-1 Namiki, Tsukuba, Ibaraki 305, JAPAN

Contents

1. Introduction

1.1. General backgrounds

Carbon is a key element that enables much variety in the material world. For example, a full variety of exquisite "molecular machines" in an organic life comes from flexibility of carbon. The flexibility means that carbon can make various types of bonds, i.e. covalent bond through sp^3 hybrid orbital and that through sp^2 orbital, representatively. In contrast with carbon, silicon or germanium usually makes only the sp^3 bond, although they belong to the same IV_b group in the periodic table. Concretely as a result, carbon crystallizes in some allotropic forms; typically diamond and graphite.

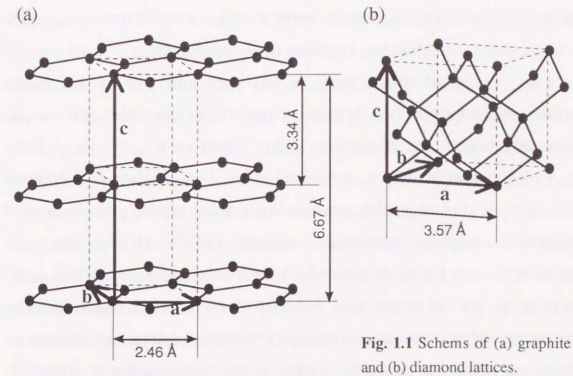

Fig. 1.1 Schems of (a) graphite and (b) diamond lattices.

Diamond is the hardest material known and valuable not only as a jewel but also as an industrial material. On the other hand, graphite is one of typical soft materials although the nearest neighbor C–C bond in

graphite is rather stronger than in diamond. This difference is caused by their structures shown in Fig. 1.1. In diamond, carbon makes a three-dimensional network of covalent bonds, so that diamond is hard and isotropic. In graphite, a covalent-bonds' network spreads two-dimensionally and carbon atoms make a basal plane of honeycomb lattice. The individual sheets are bound rather weakly and forms graphite crystal.[1)]

Graphite as a mineral was already known in prehistoric ages. Its nature and identity began to be recognized in the later 18th century, and it was named "graphite" for it has been used as substance in drawing from the Middle Ages. Now graphite plays a very important role in our industrialized society as material of electrodes, crucibles, lubricant, moderators and so on. For these applications, chemical stability of graphite is one of important features. Graphite is fairly resistant to chemical attack in severe conditions, because sp^2 orbital makes σ bond and p_z makes π bond so that no dangling bond remains in the basal plane.

As mentioned above, graphite has very long history and much importance in applications. Moreover, graphite and its sisters still supply interesting subjects worth studying. In fact, it was not long ago the exciting discovery of several kinds of fullerene[2)] and carbon nanotubes[3)], which are principally a kind of graphitic carbon. Another interesting graphite-related material is a graphite intercalation compound (GIC)[4-6)]. Graphite can intercalate other atoms, ions or molecules between the basal sheets. This intercalation is one of remarkable features of the layered materials. The graphite sheet then exchanges electrons with the intercalant and changes its electronic properties. In a GIC system, however, we cannot so arbitrarily control physical parameters, because GIC grows spontaneously under thermal equilibrium conditions. Then we naturally wish we could get and examine one isolated layer of graphite. Unfortunately, it is yet impossible to get the monolayer of graphite in free space. But we can get it on a

surface of some other materials.

1.2. Background concerning carbon chemistry on metal surfaces

Interaction of carbon with some transition metal surfaces has been extensively studied, because the knowledge about it is very important to understand catalysis of these metals in methanation and other organic reactions. On the way, monolayer graphite is found on the surface in some specific conditions. For example, let us see briefly the carbon behavior on nickel surfaces: one of most extensively studied systems.[7-16)]

Two adsorption states are known about C on Ni; one is carbide-like and the other is graphite-like.[7,9,13)] The carbidic phase, which is formed when the clean surface is exposed to hydrocarbon or carbon monoxide below 630 K, shows 2×2 p4g and very complicated patterns in low-energy electron diffraction (LEED) on (001) and (111) surfaces, respectively. Then a carbon *KVV* peak profile is specific to metal carbide in Auger electron spectroscopy (AES). On the other hand, the graphitic phase, which is formed at higher temperature, shows a clear 1×1 [on (111)] or a ring [on (001)] pattern in LEED and graphite-like AES profile.The graphitic phase condensation was observed also on the C-doped sample surfaces.[8)] The graphitic phase on nickel surfaces is recognized to be monolayer graphite by studies using AES,[8)] LEED, ultra-violet photoemission spectroscopy (UPS),[10,13,14,15)] and surface extended electron energy loss fine structure (SEELFS).[11,12)] It has been revealed that the lattice constant of the monolayer graphite is the same as the Ni–Ni distance (2.49 Å) and that the electronic band structure is similar to pristine graphite except for some energy shift. Therefore, this monolayer graphite has been thought to be similar to pristine graphite, although the other features are little known. In this study, it will be revealed that the band energy shift has an important meaning related with the bond weakening.

Besides on Ni, graphitic phase was found on Pt,[17,22] Pd,[17] Co,[17] Rh,[18] Ru,[19] Ir,[20] Re,[21] etc. In these cases, overlayer is not commensurate with the substrate and has almost random orientations, so that "graphite" is identified only by the lattice constant of the ring-like LEED pattern and by the graphitic AES peak profile, and "monolayer" is estimated only by the AES intensity. In this study, the monolayer will be proved more clearly by the softened phonon structure in the graphite layer.

1.3. Progress of experimental technique

In this section, recent progress of experimental techniques of high-resolution electron energy loss spectroscopy (HR-EELS) is briefly introduced.

In 1967, Propst and Piper firstly showed the capability of electron energy loss spectroscopy for study of surface vibration.[23] They used an energy monochromator and an energy analyzer each of one-stage 127° cylindrical electrostatic deflector type.

In the seventies, many groups has improved this technique. Ibach's group in Germany used the same type of construction but improved resolution better than 10 meV.[24,25] Andersson used another type of spectrometer: an single-stage cylindrical mirror type of monochromator and the same type of analyzer.[26,27] In the eighties, HR-EELS spectrometer of one or two-stage 127° cylindrical deflector type becomes commercially available from several companies. Ho *et al.* developed time-resolved HR-EELS by combining a position sensitive detector and a big hemispherical electrostatic analyzer, which can take one spectrum for less than 1 sec.[28,29] Recently, Ibach *et al.* have proceeded with the new constructions, and have reached the best resolution of 1 meV.[30,31] Thus many groups are improving the technique and the HR-EELS has been established as a novel method of detecting surface vibrations of adsorbed species, surface phonon

dispersions, surface polaritons, etc.

A spectrometer used in this work is designed and constructed by Dr. C. Oshima in 1984 in our laboratory.[32,33] It consists of a tandem 127° cylindrical electrostatic deflector type of monochromator and the same type of analyzer. The best resolution of the apparatus is 3 meV at the sample current of about 1×10^{-10} A. A detailed description of the apparatus will be given in the section 2.1.

1.4. Concerns of this study

It is natural to apply the new method HR-EELS to the important carbon materials. Especially for graphite, knowledge of lattice dynamics from the inelastic neutron scattering,[34] He-atom scattering,[35] infrared[36,37] and Raman[38] spectroscopies was restricted within lower energy region or long wave-length region. However, the phonon energy spreads into fairly higher energy in entire Brillouin zone (BZ) as a result of light mass of carbon and strong interatomic bonds. HR-EELS is able to detect even such a mode as the highest energy at any wave length, although the resolution does not yet reach neutron scattering, He atom scattering, light scattering or light absorption method. We[39] and Wilkes *et al.*[40] have separately applied HR-EELS to graphite single crystal for the first time, and succeeded in measuring its entire phonon dispersion relations along $[10\bar{1}0]$ in 1987.

I began this study separately to investigate chemical reactions of light element on transition metal carbide (TMC) surfaces. On the course of it, I found that carbon makes an epitaxial layer on some transition metal carbide surfaces although incommensurate to the substrate. The layer has hexagonal lattice like graphite and shows graphitic Auger profile, but it indicates fairly modified phonon dispersion compared with pristine graphite. This phonon softening can prove the overlayer to be the

monolayer. So I was very interested in this "monolayer graphite" and changed my main theme to studying its feature. In the literature, monolayer graphite phase is known on some metal surfaces, but its properties are little known. I found for the first time in the world that the interatomic bond is sometimes softened in this monolayer graphite relating to the electronic band shift.[1-5] In that case, the interaction between the monolayer graphite and the substrate was revealed to be stronger than the interlayer interaction of bulk graphite. The main subject of this thesis is, therefore, to show proper condition of making monolayer graphite, to investigate the bond softening and the electronic band shift on various substrates, to give evidence of monolayer graphite, and to propose possible mechanisms by relating the phonon structure to the electronic band structure.

It is also revealed that the monolayer graphite remains a property of graphite: chemical stability. The inertness of the monolayer graphite is expected to be useful in many applications. For example, the surface process empirically used for a field emitter made of TMC[41] is performed just in the same condition as making monolayer graphite.[6] When a clean TMC tip is used, the emission current fluctuates largely even in a vacuum of 10^{-8} Pa range. After the surface process, emission current is dramatically stabilized. This owes to less reaction rate of residual gas on the graphite covered surface.

The monolayer graphite resembles the GIC systems. Moreover, the substrate properties will possibly be changed more than those of intercalant. The monolayer graphite has possibilities of showing new properties of a graphitic layer which is hidden in the GIC systems. For example, the most doped system in the GIC is LiC_6, in which the transferred charge is 0.166··· per one C atom if Li is perfectly ionized. The phonon frequency and the lattice constant of the monolayer graphite

on TaC(111) or on NbC(111) changes more than LiC_6.

In this study, HR-EELS and angle-resolved UPS (ARUPS) are extensively applied to the monolayer graphite on some TMC and pure metal surfaces. The next chapter describes the experimental apparatus used in this study. Chapter 3 deals with the experimental conditions of making monolayer graphite on some transition metal carbide and pure metal surfaces, in addition with lattice parameters and orientations of the products. The experimental results of HR-EELS are presented in Chapter 4 and the obtained phonon dispersion relations of monolayer graphite are analysed by the force constant model. The analysis reveals the phonon softening related to the π bond. The ARUPS results for the electronic band structures of the monolayer graphite are given in Chapter 5. In electronic band dispersion relations, the π bond is found to be fairly affected by the substrate corresponding to the phonon softening. Chapter 6 deals with the molecular adsorption on the TMC surfaces. The adsorbed molecule showed significant softening within the molecule. In Chapter 7, the discovered bond softening and the electronic band shift in the monolayer graphite is discussed on the bases of charge transfer into the antibonding π^* band in comparison with molecular adsorption and graphite intercalation. Recent works concerning monolayer graphite published by other groups are also introduced. Chapter 8 is the summary.

2. Experimental apparatus

2.1. Apparatus for HR-EELS

2.1.1. Vacuum system

In Fig. 2.1, the schematic view is shown of an ultra-high vacuum (UHV) chamber for HR-EELS spectrometer made by Kyowa shinku Co. Ltd. The chamber is evacuated by a polyphenylether-oil diffusion pump with a liquid-nitrogen cooled trap (VG CCT-100) and a Ti sublimation pump equipped with a liquid-nitrogen shroud. On a bench, infrared heaters are set which have a total power of 4.5 kW, so that the whole system above the bench can be baked up to 200°C by covering it with an oven box made of Al. After 24–36 hours of baking at temperatures up to 180°C, base pressure around 2×10^{-8} Pa is routinely obtained, and has reached 5×10^{-9} Pa in the best condition. In the pressure region below 1×10^{-8} Pa, only the liquid-nitrogen cooled sublimation pump is used efficiently.

As the spectrometer deals with very low energy electron beams, field-free space is required. Especially, residual magnetic field is the problem. All the chamber is made of SUS316L stainless steel, and non-magnetic materials are carefully selected, of which the spectrometer and a sample holder are made. The main chamber has a triple magnetic shield made of 1 mm-thick metal of high permeability (permalloy), and the residual magnetic field is reduced less than 1/100 of the natural magnetic field of the earth (0.45–0.5 gauss).

Above the main chamber, a small chamber exists in which a sample is prepared by heating, gas treatment, and ion bombardment, and is characterized by LEED and AES. The section view of this stage is shown in Fig. 2.2.

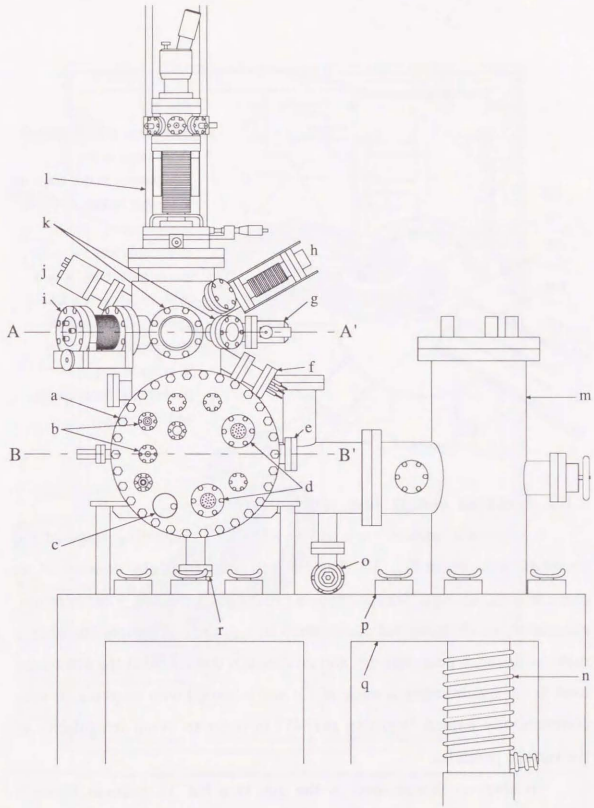

Fig. 2.1 High resolution electron energy loss spectrometer outer view. a: main flange, b: channeltron signal connector, c: rotary feedthrough for monochromator rotation, d: connectors for spectrometer electrodes, e: view port, f: ion bomberdment gun, g: gas introduction, h: retractable filement for H dissociation, i: retractable cylindrical morror analyser for AES, j: electron gun for AES, k: view port, l: sample manipurator, m: liquid-nitrogen cooled trap, n: oil diffusion pump, o: valve for rough pumping, p: baking heater, q: bench, r: ionization vacuum gauge.

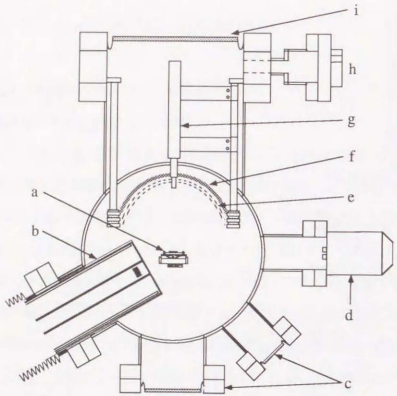

Fig. 2.2
Schematic section view of A–A' stage in Fig. 2.1. Equipments in this stage are a: sample holder, b: CMA, c: view ports, d: variable leak valve for gas introduction, e: two grids for backview LEED system, f: glass made phosphorescent screen, g: electron gun, h: electrical feedthrough, and i: view port.

2.1.2. Electron energy loss spectrometer

A schematic section view of the HR-EELS measuring stage of the chamber is shown in Fig. 2.3. The HR-EELS spectrometer consists of an electron gun, an input lens system, a pre-monochromator, a main monochromator, acceleration and deceleration lens systems, a sample chamber, a main analyzer, a post-analyzer and an electron detector. All the electrodes used in the spectrometer is made of Cu and is coated with graphitic powder commercially named "aquadag (#154)" in order to avoid irregularity of the surface potential.

An electron source used in the gun is a hot Ta cathode filament (ϕ0.2–0.25 mm) having a point tip made of thoriated tungsten (ϕ0.125 mm). Electron emitted from the tip is accelerated and focused by a repeller electrode surrounding the filament and an input einzel lens made of three plates. The first and the third electrodes in the lens are each divided into up and down parts, and the second one is divided right and left, so that they

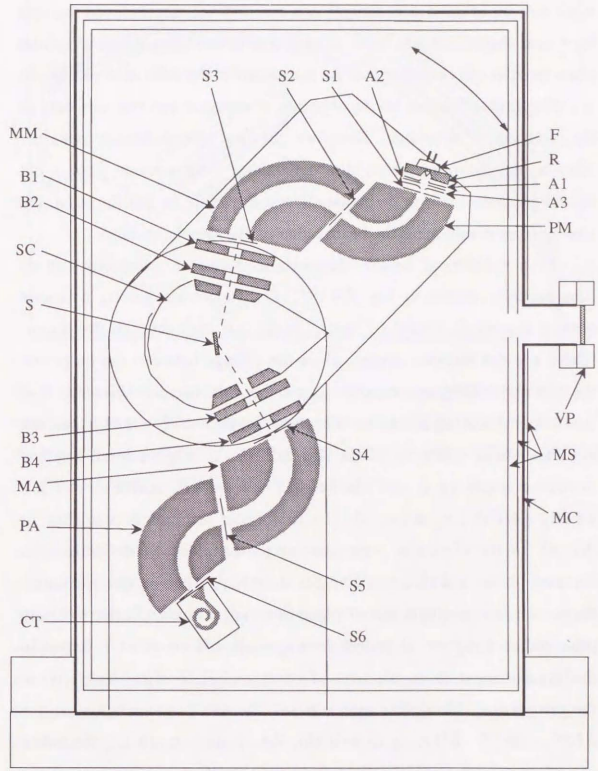

Fig. 2.3
Schematic section view of B–B' stage in Fig. 2.1. F: cathode filament, R: repeller, A1–A3: input lens, PM: pre-monochromator, MM: main monochromator, S1–S3: slits, B1 & B2: acceleration lens, SC: sample chamber, S: sample, B3 & B4: deceleration lens, MA: main analyser, PA: post-analyser, S4–S6: slits, CT: channeltron, VP: view port, MS: magnetic shield, MC: main chamber.

work as a set of deflectors as well as a lens. All the electrodes in the lens have oval shaped holes in order to have a different focus in the horizontal plane from in the vertical plane. As mentioned in the following paragraph, a 127° cylindrical sector has focal points on entrance and exit slits only in the direction of deflection. Therefore, the lens system has to focus the beam on the slit in the direction of deflection (the horizontal plane), but should not focus on it in the perpendicular direction. In that direction, the lens systems should focus the beam rather on the sample position.

In a cylindrical sector electrostatic deflector, electrons run as schematically shown in Fig. 2.4.[42-44] Only electrons having a kinetic energy around $E_0 = e\Delta V \,/\, 2\log(r_{out} / r_{in})$ can pass through the sector, where e is the electron charge, ΔV is the voltage between the inner and the outer cylinders, and r_{in} and r_{out} are the radii of each cylinders. The first order focusing exists in the plane at $\Phi = \pi/\sqrt{2} \sim 127°$; i.e. the electron, which enters the sector at a radius r_0 having an small in-plane incidence angle of α and energy of $E = E_0 + \Delta E$, reaches $r = (1 + \Delta E/E_0 - 4\alpha^2/3) r_0$ at that Φ; the first order term of α vanishes at that Φ. In the direction perpendicular to the plane of deflection, no focusing occurs and electrons diverges straightly. When an electron enters the sector at an small out-of-plane incidence angle β, the velocity projected on the plane of deflection is $v_0 \cos\beta$, and therefore, it moves in the same manner as an electron of energy of $E_0 \cos^2\beta \sim E_0 (1-\beta^2)$ in the projection. Taking this into account, the electron reaches $r = (1 + \Delta E/E_0 - 4\alpha^2/3 - \beta^2) r_0$ at an exit slit. When the exit slit has the width of s, electrons can exit if the next condition is satisfied.

$$| \Delta E/E_0 - 4\alpha^2/3 - \beta^2 | < s/2r_0$$

In a real system, there also exists a slit at the entrance so that the condition is written as follows;

$$-s/r_0 < \Delta E/E_0 - 4\alpha^2/3 - \beta^2 < s/r_0,$$

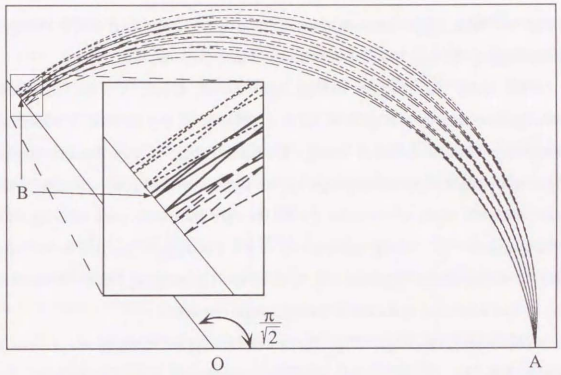

Fig. 2.4 Schematic electron trajectories in a cylindrical electrostatic field. Electrons starting at the input slit A at in-plane angle deviations of $\alpha = \pm 6°, \pm 3°$ and $\alpha = 0°$ focus on the output slit B. Solid curves correponds to the appropreate kinetic energy E_0. Broken and dotted curves are for 0.98 E_0 and 1.02 E_0, respectively.

and then the energy resolution is given as;

$$\Delta E/E_0 < s/r_0 + 4\alpha^2/3 + \beta^2.$$

In this expression, α and β represent the beam divergence. In the real system, β is fairly small because the slit height is very small compared with the pass length. But α and s must not be too small to get reasonable transmission. So we should reduce the pass energy E_0 in order to get small ΔE.

In this theory, ideal cylindrical field is assumed. But in the real system, field distortion exists near the entrance and exit slits. This effect is known as a fringing field effect and some correction rules have been used. Oshima *et al.* calculated electron trajectories in the field containing the fringes exactly, and find the optimum angle of the deflector electrodes is

126.5°.[33] The angle between the entrance slit and the exit slit is changed according to the gap length between the inner and outer cylinders.

In order to reduce background noise level, a fine sawtooth corrugation pattern is engraved on the surfaces of the cylinders. Electrons which have much different energy from the tuned energy deviate largely from the center path and impinge on the cylinder wall. If the cylinder wall were smooth, some of them would be forward reflected, pass thorough the exit slit, and make background noise or any ghost peaks in the worst case. On the sawtooth corrugated surface, almost all impinging electrons must be backward scattered and cannot pass through the sector.

The spectrometer used in this work has actual dimensions shown in Table 2.1. The slit width is 0.3 mm and its length is 4 mm. Both up and down sides of the cylinder electrodes, plate electrodes are arranged. These electrodes are biased negatively and repel the divergent electrons in the vertical direction. In other words, the plates work as a lens in that direction, and as a deflector additionally.

The pre-monochromator operates under higher pass energy (0.8-1.5 eV) and briefly selects the beam energy, because a space charge effect is so large in this stage that the passing current unpractically reduces when the pass energy is lowered. The electron current measured at the slit s_2 is

Table 2.1 Dimensions of the spectrometer. r_{in} and r_{out} are the radii of the inner and outer cylinder. r_0 is the radius of the electron path.

	Pre-monochromator	Main monochromator	Main analyser	Post-analyser
r_{in} [mm]	22	31	31	22
r_{out} [mm]	27	42.5	42.5	28
r_0 [mm]	25	36	36	25

about 3-10 μA. Almost all electrons are cut by this slit and the beam current is reduced by about 1/1000 measured at s_3. The main monochromator is used at the pass energy of 0.3–0.5 eV in order to obtain a highly monochromated beam. The current at the slit s_3 is about 3 nA and the current at the sample position is 0.1–0.2 nA. The main and post analyzers operate under the similar condition to the main monochromator. The energy analysed electron is finally detected by a "channeltron" electron multiplier (Phillips B419BL) and counted. When the monochromated beam is directly put into the analyzer, the electron current at the channeltron head is about 0.01 nA.

In order to get high resolution, the pass energy in the monochromator and the analyzer is maintained at a constant low value. On the other hand, an incident beam on a sample must have energy as high as a few tens of eV to measure phonon dispersions in the whole BZ. Therefore, the beam exiting the monochromator must be accelerated to desired energy and focused on the sample by the lens system, and scattered electrons are decelerated and focused before entering the analysing sector. The each lens system consists of three plates of about 6 mm in thickness. The outermost one is earthed, the middle one is biased much positively (10–50 V), and the inner one is slightly negative-biased. The inner plate is divided into up and down parts in order to deflect the beam. Each plate has a long hexagonal hole to have different focus between horizontal and vertical directions. In this system, energy scanning is made under the constant pass-energy mode; the retarding voltage of the analyzer is scanned to get an energy spectrum.

A sample is placed in the sample chamber between the monochromator and the analyzer. This area is roughly surrounded by permalloy metal to reduce disturbances from the outside. A stage on which the monochromator is set is rotatable around the sample chamber from 0°, at which angle the monochromated beam directly aims at the analyzer, to 90°.

In measuring a phonon dispersion relation, the incidence angle is changed by rotating the monochromator.

After all, this spectrometer routinely achieves an overall resolution power of 4–5 meV for a metallic sample. The beam current at the sample position is $1–2 \times 10^{-10}$ A and the count rate of an elastic peak is typically more than 2×10^5 c/s. The best resolution value has been less than 3 meV.

2.1.3. Power supply and data acquisition system

Figure 2.5 shows a block diagram of a control system of the spectrometer, and Fig. 2.6 shows the circuit's detail of the main controller. The system consists of regulated DC power supplies, a noise-cut transformer, potentiometers, low-pass filters, a computer-controlled scanning power supply, and an acceleration voltage power supply. The data acquisition system consists of pre and main amplifiers, a single channel pulse height analyzer, a rate meter, a counter and a personal computer.

In order to get high resolution power, the applied voltage must be highly stabilized. As a commercial AC line contains a fair amount of high-frequency noise, it must be firstly filtered by the noise-cut transformer (Denkenseiki NCT-6). Using this clean AC, some DC is produced by regulated power modules. These DC lines are divided by potentiometers, filtered by capacitors, and connected to the spectrometer by using two sets of shielded computer cables having 28 pin connectors. Between the spectrometer chamber and the controller, only one earth line is connected not to make a ground loop. In this state, the noise level at the connector position of the spectrometer is at most 3 mV peak to peak. Low-pass filters consisting of ceramic condensers and ferrite beads are inserted at this connector, and then the noise level is reduced to less than 1 mV.

Pulses from the channeltron are amplified by the preamplifier (ORTEC 142PC) and the main amplifier (ORTEC 572). Low height noise

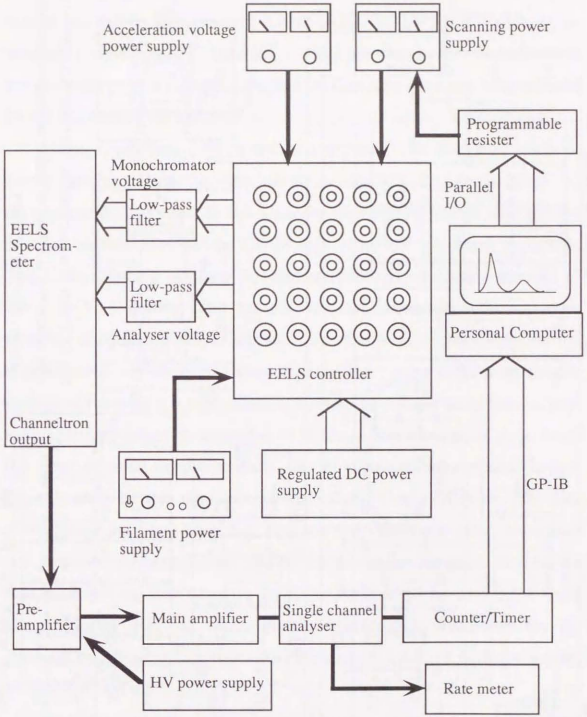

Fig. 2.5 Block diagram of the high resolution electron energy loss spectrometer control system.

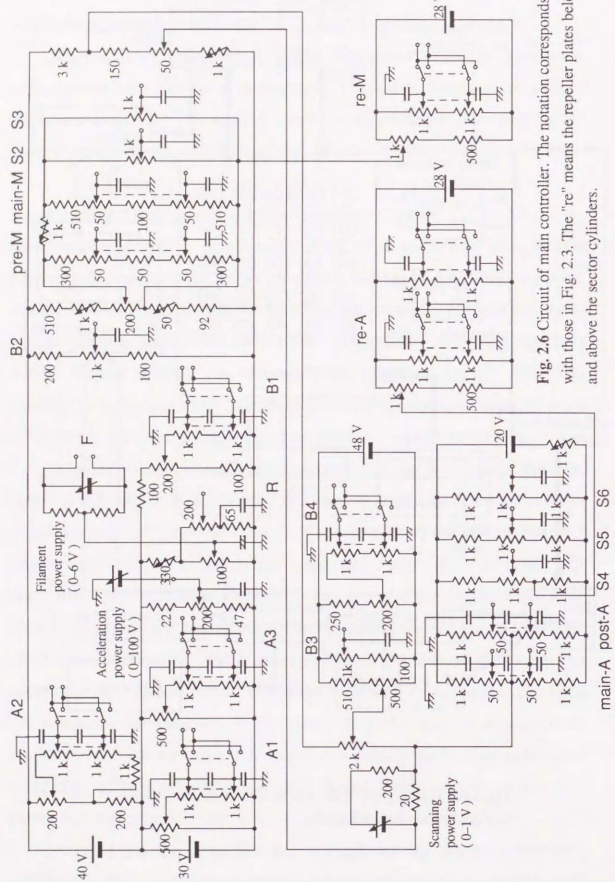

Fig. 2.6 Circuit of main controller. The notation corresponds with those in Fig. 2.3. The "re" means the repeller plates below and above the sector cylinders.

pulses are cut by the pulse height analyzer (ORTEC 550), and the signal is then counted by the counter (CANBERRA 2071A) and is took in the personal computer (NEC PC-9801). The high voltage bias is supplied to the channeltron by a CANBERRA 2861A. Counting rates can be monitored by the ratemeter (ORTEC 449).

Energy spectra are taken by the computer. The computer sends at first a floating voltage between the monochromator and the analyzer by using a parallel I/O port to the scanning power supply, and then get the counted number through a GP-IB bus from the counter. Typically, 100–1000 channels are used for one spectrum at an energy interval of 0.5–2 meV. Counting time per one channel is usually 1–2 sec. for a specular condition and 10–300 sec. for off-specular conditions. In my experimental environment, external pulse-like noises sometimes disturb data at an interval of a few minutes. In order to remove these noises, data acquisition procedure is improved as follows. The scanning is done fast (0.5–5 sec./channel) and repeatedly, and an acquired datum of one channel is compared to the expected mean value calculated from the data accumulated until last time. If it deviates from the mean value more than 3–4 times of the standard deviation, the datum for the channel is again measured. In the first scan we have no standard to be compared with. Usually, after first 1–3 scans, manual correction is necessary for the channels including noises. After that, the above mentioned noise-correction system works well.

Graphite covered surfaces studied in this work is so inert that long time measurement is possible. The noise-correction procedure was very useful in the long time data accumulation to get high S/N ratio in phonon measurements. On the other hand, this procedure is beneficial to measuring a very active surface. Such a surface remains clean only for a few tens of minutes even in a vacuum of 10^{-8} Pa. As it must be cleaned every one or

two scans, which take 10–20 minutes, the repeated rapid scanning is very useful.

2.1.4. Sample manipulator

A manipulator used in this study has 5-axis motion; strokes of ±10 mm along x- and y-direction in the horizontal plane and 300 mm in z- (the vertical) axis, and rotations around the z-axis (θ) and around the normal axis to a sample surface (ϕ). The precision is 0.01 mm in x and y axis, 0.5 mm in z axis, and 0.5° in θ axis. All flanges and bellows are made of stainless steel, and the transfer mechanism outside the vacuum is made of Al alloy.

Figure 2.7 shows a schematic view of the sample holder. A carbide or boride sample is held with Ta thin metal of a 0.1–0.15 mm thickness, and attached to the sample holder. A Ta filament (ϕ 0.2–0.3 mm) is set behind the sample, which is used to heat the sample by electron bombardment. The

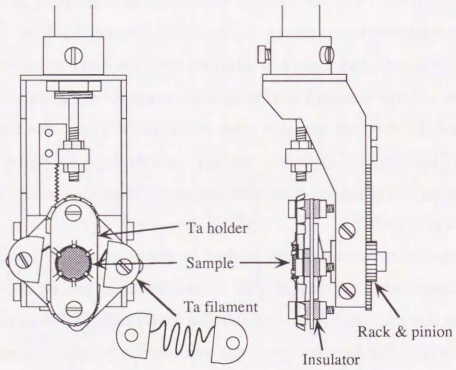

Fig. 2.7 Schematic view of the sample holder.

sample and the filament is insulated by alumina ceramics. Other parts of the sample holder is made of Mo and beryllium copper. In the electron bombardment, the sample is floated at +500–1000 V and a current of about 3–5 A is passed through the filament to emit thermal electrons of 1–200 mA. Then the sample is heated even above 2000°C. Metal samples (Ni and Pt) were held in another way; a sample is spot welded to two Ta wires (ϕ 0.2–0.3 mm) in the both side, and is attached to the holder suspended by the wires. The sample is heated by directly passing a current of 3–15 A through those wires.

The sample temperature is measured by two-color optical pyrometers (Chino IR-Q2C: λ = 0.85/1.00 μm in 800–1600°C and IR-Q4C: 0.50/0.58 μm in 1500–3500°C) and an infrared optical pyrometer (Chino IR-P2C: λ = 2.0 μm in 300–800°C).

2.1.5. LEED optics

On the upper stage, a two-grid back-view LEED optics (Omicron spectaLEED) is equipped. This LEED optics has a small electron gun using a LaB_6 emitter, two hemispherical grids and a glass-made fluorescent screen to realize observation from the backside.

A controller power supply is designed by our group and constructed in Tsuji densi Co. Ltd. In order to get a focused beam while changing an acceleration voltage, every potential applied to an einzel lens traces linearly the acceleration voltage. The offsets and the ratios are separately adjustable.

2.1.6. Cylindrical mirror analyzer for AES

A small cylindrical mirror analyzer (CMA) made by Yamamoto shinku Co. Ltd. and a grazing incidence electron gun (Phi model 04-015) are equipped in the same stage as the LEED optics. The CMA is attached to

a ϕ114 flange through a linear transfer mechanism and is retractable. Usually a 1.5 keV primary beam is used for excitation in AES measurements.

An Auger spectrum is acquired with dN/dE mode by using a locking amplifier (PAR Model 126). A reference signal produced by the lock-in amplifier modulates an applied voltage to the outer cylinder through an insulating transformer so that the pass energy is modulated. The electrons are detected and amplified by a ceratron electron multiplier in a current mode, and an AC component of the amplified current is inputted to the lock-in amplifier through a ceramic condenser.

2.1.7. Ion bombardment gun and gas introduction system

On the upper stage, a hand-made ion gun of B-A gauge type exists. In this study, Xe ion bombardment was applied only to Ni samples in order to remove sulfur impurity. The ion gun can produce a Xe^+ ion beam (~200 eV) of 0.5–1 μA in Xe gas of the pressure range of 10^{-3} Pa. Ion acceleration voltage (500–1000 V) is usually applied to a sample.

In this study, ethylene gas is used for making the monolayer graphite. Oxygen and Xenon are used in cleaning metal samples. Additionally H_2, CO and N_2 are used in the adsorption experiment described in the section 6.2. These gases (Matheson research grade gas) are purchased in the form of glass ampules. They are individually connected to variable leak valves (Anelva 951-7172) and attached to the main chamber.

2.2. Apparatus for ARUPS

2.2.1. Vacuum system

In the experiment of ARUPS, a commercially available ESCA system (VG scientific ADES-400) is used. The main chamber has a diameter of 370 mm and 500 mm height, and is magnetically shielded with mu-metal.

It is evacuated by the same system (an oil diffusion pump & a liquid-nitrogen cooled trap & a Ti sublimation pump) as the EELS chamber and obtains a base pressure of 1×10^{-8} Pa routinely. It is equipped with a LEED optics, gas introduction systems, a low energy ion gun, an ultraviolet lamp, a sample loading chamber, and a spherical-sector electrostatic analyzer. The sample loading chamber is connected to the main chamber through a gate valve and separately evacuated by another diffusion pump. It enables rapid introducing a sample into the main chamber without breaking a vacuum.

2.2.2. Spherical-sector energy analyzer

On a base flange of the main chamber, there is a turn table, on which a spherical-sector electrostatic analyzer exists. It has a resolution power of $\Delta E/E \sim 0.01$. In the UPS experiment, the pass energy of 20 eV was adopted, and then the resolution power is about 0.2 eV. This analyzer is used in ion scattering spectroscopy (ISS) experiments. In that case, a pass energy of 200 eV (the resolution of ~2 eV) is usually used to get higher transmittance, because the ion beam intensity is weaker and its energy spread is wider compared with electron.

The analysed electron is detected by a channeltron electron multiplier, and energy spectra are collected by a personal computer. The energy scanning is done by the constant pass energy mode like the case of EELS.

2.2.3. Ultraviolet light source

As a light source in the UPS experiment, a UV lamp made by VG was used. The UV lamp consists of two differentially pumped stages. High purity He gas is introduced through a variable leak valve into the first stage, which is pumped out by a rotary pump through another port. On that stage, ceramic discharge cell is attached and high voltage DC is applied

on the other side of the cell. A collimator having a pin hole is put between the first stage and the second stage. The second stage is differentially pumped by a diffusion pump. Between the second stage and the main chamber, there is a quarts pipe for collimation of the light and differential pumping.

He II emission (40.8 eV) is used in the UPS experiment. The intensity of the He II emission largely depends on the He gas pressure in the lamp. Principally, the lower the pressure is, the higher the intensity becomes. But the discharge stops in too low pressure. When the pressure is high, the discharge cell looks bright orange from the outside. In such a case, He II light is hardly emitted. The pressure reduction changes the color to dark violet. In the best condition, it is difficult to know whether the cell shines or not without darkening the room. In that case, the pressure in the main chamber remains in the 10^{-8} Pa range. The discharge current and voltage were 60 mA and 600 V, respectively.

3. Formation of monolayer graphite

3.1. Preparation of the substrate

3.1.1. NaCl-type transition metal carbide (TMC) surfaces

In this study, substrates TaC(111), TaC(001), HfC(111), HfC(001), NbC(111), NbC(001) and TiC(111) were used. These IV_a- and V_a-group transition-metal carbides are very hard crystals having a structure of NaCl type (Fig. 3.1).[45] They have metallic conductivity as they have metallic (TaC and NbC) or semimetallic (TiC and HfC) electronic structure. The melting points are very high (3000–4000°C). Single crystals were grown in our laboratory by using the RF-heated zone-leveling floating zone (FZ) method.[46-49] The grown crystals have rod shapes of 6–9 mm in diameter. They are oriented by using reflection Laue X-ray diffraction method, and cut by spark erosion method in a disk-shape of 6–9 mm in diameter and 0.5–1.5 mm in thickness. One side of disks are mechanically polished roughly with B_4C powder (at first #120 and finally #1200) on a glass plate, and finally with diamond paste (1 μm) on a polishing cloth to a mirror finish. They are ultrasonically cleaned with acetone and attached to sample holders made of Ta sheet (0.1–0.15 mm in thickness).

In a vacuum, a sample is firstly degassed at a temperature of about 1200°C until the pressure decreases to lower 10^{-7} Pa range. The sample is heated by an electron bombardment on the backside. Next, the sample is repeatedly flash heated to 1800°C (TiC) – 2100°C (the others). The temperature should be gradually increased spending 1–2 minutes. The flashing temperature is kept for about 10 sec. If the temperature is increased too rapidly, the sample would possibly be broken by thermal stress.

After the heating procedure, the sample becomes clean; LEED shows

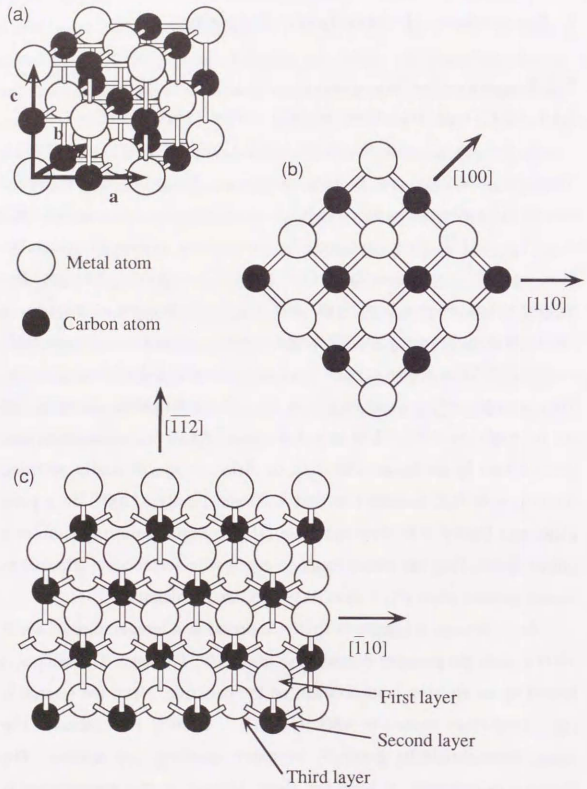

Fig. 3.1 Structural model of NaCl-type transition metal carbide: (a) unit cell, (b) (001) surface, and (c) (111) surface.

(a)

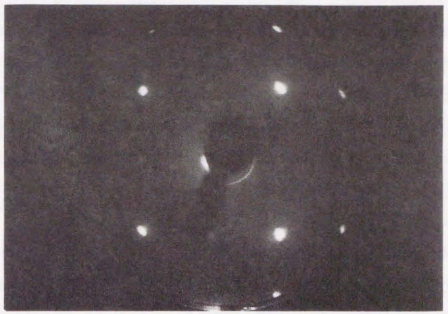

(b)

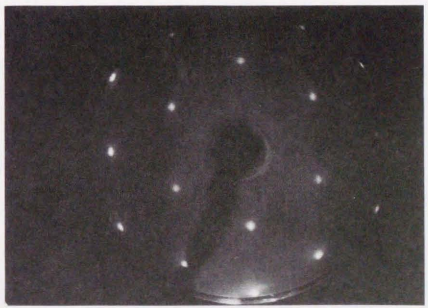

Fig. 3.2 LEED patterns of (a) clean TiC(001) and (b) TiC(111). Primary electron energies for each patterns are 204.9 eV and 229.1 eV, respectively.

a clear 1 × 1 pattern and no impurity is detected in AES. For example, LEED patterns of TiC clean surfaces are shown in Fig. 3.2. Previous investigations using the impact-collision ion scattering spectroscopy (ICISS) revealed that truncated bulk structures take place in these surfaces; Only metal atoms appear in the outmost layer on the clean (111) surfaces of these NaCl-type TMC, while the clean (001) surfaces are composed of alternate arrangement of the metal atoms and carbon atoms at almost the same height.[50-54]

3.1.2. WC(0001) and WC(10$\bar{1}$0)

Single crystals of WC is grown by the boron doped floating zone method in our laboratory.[55] WC has a hexagonal structure as shown in Fig. 3.3. Surfaces of (0001) and (10$\bar{1}$0) are prepared by the same method as mentioned above. Although WC(11$\bar{2}$0) was prepared, it went to facets of (10$\bar{1}$0) and (01$\bar{1}$0) planes under heating.

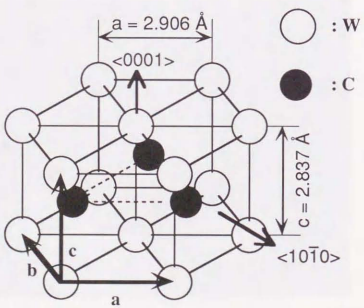

Fig. 3.3 Structure of WC.

When the WC(0001) is heated in a vacuum up to 1500°C, an LEED pattern appears as shown in Fig. 3.4, which shows existence of an incommensurate epitaxial graphite layer on the surface. It was reported in the literature that WC(0001) surface is covered by graphite when heated in vacuum.[56] This structure remains unchanged under heating up to 1800°C. This surface is measured here as a graphite covered WC(0001) surface.

Heating this surface in oxygen atmosphere of 10^{-4} Pa for 1 hour, however, results in the structural change into very complex (Fig. 3.5) and finally $\sqrt{13} \times \sqrt{13}$ (R±13.9°) (Fig. 3.6) structures in LEED. This structure is reproducible and thought to be the reconstruction of the clean WC(0001) surface, although the atomic structure of this reconstructed surface is not yet clear. When this WC(0001) $\sqrt{13} \times \sqrt{13}$ (R±13.9°) surface is exposed to 100×10^{-4} Pa·s of oxygen at room temperature, it changes 1 × 1.

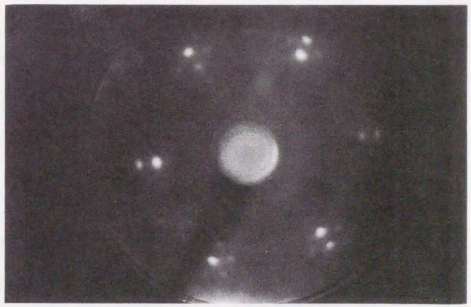

Fig. 3.4 LEED pattern of graphite covered WC(0001). E_0 = 176.1 eV.

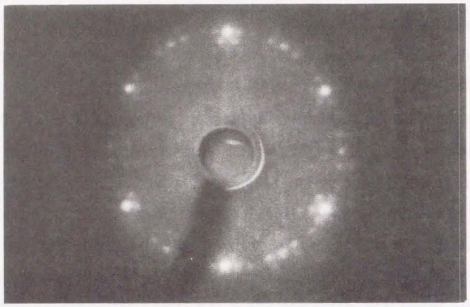

Fig. 3.5 Complex LEED pattern on the way of cleaning WC(0001). E_0 = 200.3 eV.

Fig. 3.6 LEED pattern of clean WC(0001)$\sqrt{13} \times \sqrt{13}$ (R±13.9°). E_0 = 166.4 eV.

On the other hand, WC(10$\bar{1}$0) can be cleaned only by heating in vacuum up to 2000°C. After degassed at 1500°C, a fairly sharp 1 × 1 pattern is observed in LEED. When the sample is flash heated above 2000°C, a mixed LEED pattern of 2 × 2 and streak along c axis or the <0001> direction appears as shown in Fig. 3.7. This surface having 2 × 2 and 1 × n mixed structure is considered to be the clean surface rather than the 1 × 1 observed after the degassing. Because of possible stacking faults, a crystal of WC-type structure can have two equivalent grain in it. The "(10$\bar{1}$0) surface" named here may have in fact two domains of (10$\bar{1}$0) and ($\bar{1}$010). Probably this is the reason of the mixed structure observed in the LEED pattern. The atomic structure is not yet clear in the each domain.

Fig. 3.7 LEED of clean WC(10$\bar{1}$0). E_0 = 223.2 eV.

3.1.3. Metal surfaces

Ni crystal used in the UPS experiment is also grown in our laboratory using a conventional FZ method by RF heating. Ni(111) and Ni(001)

crystals used in the EELS experiment were supplied from ISSP*. Pt (111) single crystal (one surface is polished, ϕ 8 mm $\times$ t 1 mm) was purchased from Johnson Matthey Chemicals Limited.

The metallic samples were spot welded to two Ta wires (ϕ 0.3 mm) and attached to the sample holder. The sample is heated by passing current directly through the wires.

The Ni(111) sample used in the UPS experiment is prepared as follows; Firstly it is oriented by the X-ray Laue method, then cut by the spark erosion method in a disk shape (ϕ 8 mm $\times$ t 1 mm) and mechanically polished with alumina powder (2 μm) on a polishing cloth to a mirror finish. Secondly the sample is electrochemically polished in a mixture of HNO_3 and CH_3OH (1:2 in volume). The current is 2–3 A for about 10 min. (The sample is positive.) When such a prepared sample is degassed in a vacuum at about 600°C, LEED shows a sharp 1 $\times$ 1 pattern. Without the electrochemical polishing, it is difficult to get a well ordered surface within such a short time by using vacuum process.

After the Ni sample is degassed, the impurity level is checked by AES or ISS. If yet contaminated, especially by S, it is finally cleaned by an ion bombardment (Xe^+, 1–1.5 keV, ~0.5 μA, 10 min.) and subsequent annealing (~700°C) in a vacuum. Then clean well-ordered 1 $\times$ 1 surfaces of Ni(111) and Ni(001) are obtained.

Pt(111) is easier to be cleaned than Ni. After the sample is heated in a vacuum, the last remaining contamination was C in the case of Pt(111). In order to remove the C contamination, the sample is heated at about 1000°C in oxygen of 10^{-4} Pa for several hours. Then the sample is flash heated in a vacuum up to 1100°C to remove oxygen. A clean well-ordered Pt(111) 1 $\times$ 1 surface appears after that.

*The samples were what had been used in Ref. 16.

3.2. Results of the monolayer-graphite formation

After getting the clean surfaces, graphite is formed by cracking hydrocarbon molecule; The sample is heated in ethylene gas in this study. The appropriate conditions are different for each sample. Immediately after the exposure, the C_2H_4 gas is evacuated and the sample is cooled to room temperature. Then the surface is checked by LEED. If the graphite spots does not appear, the exposure process is repeated under a different condition. All measurements are done in the vacuum at room temperature.

3.2.1. Monolayer graphite on TaC(111), HfC(111), TiC(111) and NbC(111)

The clean TaC(111) is exposed to 240 $\times$ 10^{-4} Pa·s of ethylene gas while the sample is kept at 1000°C. Then the LEED pattern showed two-domain graphite layer as shown in Fig. 3.8. In Fig. 3.9, the schematic view of the LEED pattern is shown. Vectors $\mathbf{s}_1$ and $\mathbf{s}_2$ represent the unit vectors of the substrate's two-dimensional reciprocal lattice. $\mathbf{g}_1$, $\mathbf{g}_2$, $\mathbf{h}_1$ and $\mathbf{h}_2$ are those of the overlayer graphite. Epitaxial relationships are $(0001)_C \parallel (111)_{TaC}$ and $[10\bar{1}0]_C \parallel [1\bar{1}0]_{TaC}$ for the domain of $\mathbf{g}_1$ and $\mathbf{g}_2$, and $(0001)_C \parallel (111)_{TaC}$ and $[11\bar{2}0]_C \parallel [1\bar{1}0]_{TaC}$ for $\mathbf{h}_1$ and $\mathbf{h}_2$. When the graphite is formed at this temperature (1000°C), these two domains coexist although the one domain ($\mathbf{g}_1$ and $\mathbf{g}_2$) is stronger. When the exposure is done at lower temperature (~800°C), the domain of $\mathbf{h}_1$ and $\mathbf{h}_2$ is hardly observed and one domain ($\mathbf{g}_1$ and $\mathbf{g}_2$) structure is obtained, but slight higher background in LEED indicates the lower quality of the overlayer graphite. On the contrary, the $\mathbf{h}_1$ and $\mathbf{h}_2$ domain dominates in higher-temperature (>1200°C) processing. The lattice constant a of the overlayer is estimated at 2.53 $\pm$ 0.02 Å from the LEED patterns by comparing with the substrate (3.15 Å). This value is about 3 % larger than the bulk graphite (a = 2.46 Å). The positions of other spots appearing in the LEED pattern are

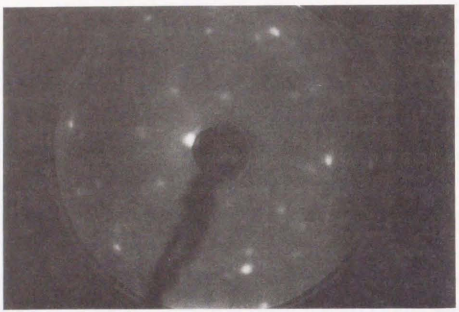

Fig. 3.8 LEED pattern of graphite covered TaC(111). E_0 = 143.0 eV.

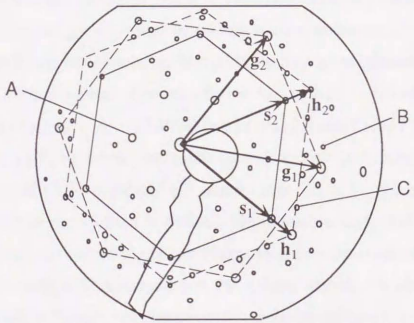

Fig. 3.9 Schematic view of Fig. 3.8. Vector $\mathbf{s}_1$ and $\mathbf{s}_2$ are the unit vectors for the substrate. $\{\mathbf{g}_1, \mathbf{g}_2\}$ and $\{\mathbf{h}_1, \mathbf{h}_2\}$ are unit vectors for the two domains of monolayer graphite. Other spots are double diffractions. For example, $-\mathbf{s}_1 - \mathbf{s}_2 + \mathbf{g}_1$ arrives at the spot A, $2\mathbf{s}_1 - 2\mathbf{s}_2 + 2\mathbf{g}_2$ arrives at the spot B, and $\mathbf{s}_1 - \mathbf{s}_2 + \mathbf{h}_2$ reaches the spot C.

presented by sum vectors of the substrate's and the graphite's reciprocal-lattice vectors. These "satellite" spots are caused probably by the double diffraction. However, some real electronic or structural modulation in the overlayer graphite is possible because the overlayer is incommensurate to the substrate. Such a modulation can result in the same satellite spots. Anyway, the appearance of the satellite spots itself indicates the thinness of the overlayer, which is comparable to or less than the mean free path of electron in the LEED energy region (about 10 Å at most).

AES spectra are shown in Fig. 3.10. On the clean TaC(111), Ta *NVV* and C *KVV* Auger peaks are seen at 160–180 eV and at ~270 eV, respectively. A small Auger peak of Ta appears also at around 330 eV. When the monolayer graphite is formed, the C *KVV* peak increases its intensity compared with the Ta peaks and changes its profile from so-called "carbidic" shape to "graphitic" one.[9] The carbidic peak shows two sub-peaks in the lower energy side of the main peak. The spectrum shown here has such a feature. In the graphite covered surface, this characteristic structure becomes small though not vanishes, and the main peak shows somewhat graphitic feature, which is characterized by the broad single peak with a small structure in lower energy side.

The preliminary experiment was done to examine the appropriate amount of the ethylene exposure. When TaC(111) was exposed to 30×10^{-4} Pa·s of ethylene at 1000°C, graphite spots were already recognized in LEED. This surface was, however, not completely covered by the graphite layer, because some loss peaks appeared around 50–60 meV in the specular EELS spectrum to indicate existence of some adsorbate not on graphite layer but on TaC(111) surface itself. In fact, when the exposure exceeds 100×10^{-4} Pa·s, no loss peak is seen in this energy region under the same condition of EELS. When the ethylene exposure was increased to 1000×10^{-4} Pa·s, any result of LEED, specular or off-specular EELS is not

different from that of the sample grown by 240×10^{-4} Pa·s exposure. These results show that the graphite deposition spontaneously stops when the surface is saturated. About 100×10^{-4} Pa·s ethylene exposure corresponds to the saturation coverage. The amount of the exposure is not critical for the overlayer thickness and the identical graphite-covered surface can be easily reproduced. Here, the exposures of $200–300 \times 10^{-4}$ Pa·s are adopted in order to make the saturation sure.

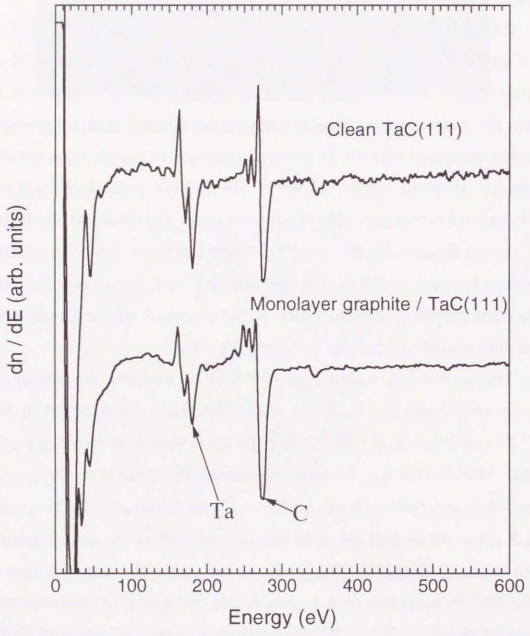

Fig. 3.10 AES spectra of clean and graphite covered TaC(111)

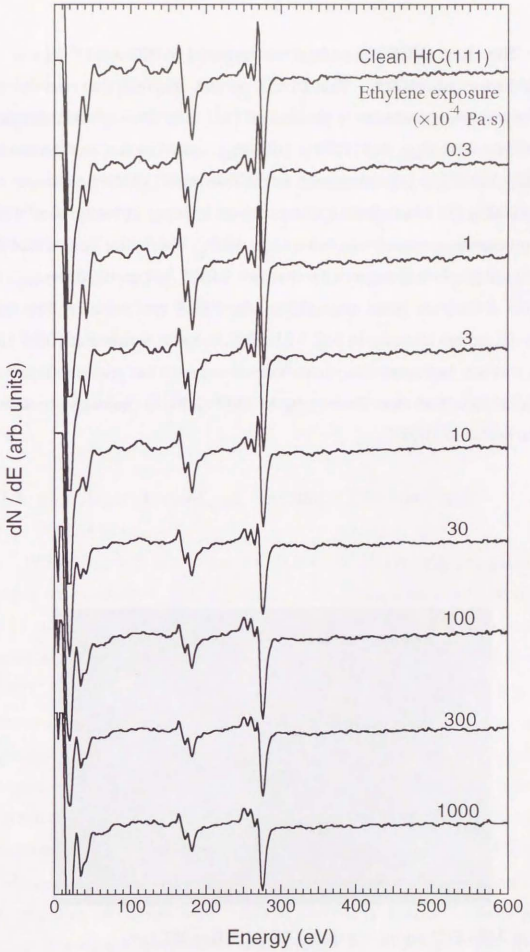

Fig. 3.11 AES change while making monolayer graphite on HfC(111) at 1100°C.

The clean HfC(111) surface was exposed to 200×10^{-4} Pa·s at the temperature of 1100°C. The LEED pattern showed the two-domain overlayer structure similar to the case of TaC(111); Two epitaxial domains ($[10\bar{1}0]_C \parallel [1\bar{1}0]_{HfC}$ and $[11\bar{2}0]_C \parallel [1\bar{1}0]_{HfC}$) coexist but one domain of $[10\bar{1}0]_C \parallel [1\bar{1}0]_{HfC}$ is predominant. In the case of HfC(111), no change was observed in the LEED pattern except for an increase in background when the process temperature was lowered to 950°C. The lattice constant of the overlayer graphite is estimated to be 2.49 ± 0.02 Å from the direction of a double diffraction beam measured by the EELS spectrometer. The AES spectral change is shown in Fig. 3.11. The change is finished at 100×10^{-4} Pa·s, which indicates the saturation coverage. The graphite layer on HfC(111) survives short flashing up to 1500°C, but is thoroughly removed when heated to 1600°C.

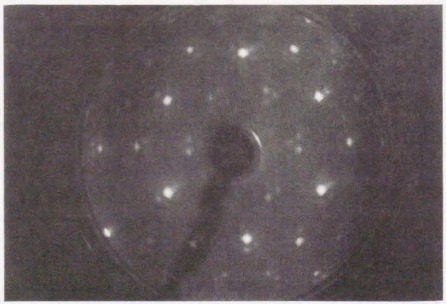

Fig. 3.12 LEED pattern of graphite / TiC(111). E_0 = 202.3 eV.

In the case of TiC(111), graphite layer was formed under the same condition as on HfC(111): 200×10^{-4} Pa·s of C_2H_4 exposure at 1100°C. Only one domain oriented to $[10\bar{1}0]_C \parallel [1\bar{1}0]_{TiC}$ was observed in the LEED pattern with very low background (Fig. 3.12), indicating high quality of the overlayer graphite. Because TiC has a lower melting point than TaC or HfC,[45] the grown crystal has better quality. Probably higher density of defects in TaC and HfC crystals causes the two domain structure in the overlayer graphite. The lattice constant of the graphite on TiC(111) is estimated at 2.50 ± 0.02 Å from the LEED.

NbC(111) was exposed to 300×10^{-4} Pa·s of ethylene at 1100°C. Also in this case, only one domain of graphitic layer was produced, which is oriented to $[10\bar{1}0]_C \parallel [1\bar{1}0]_{NbC}$. The lattice constant was estimated at 2.52 ± 0.02 Å.

3.2.2. Monolayer graphite on TaC(001), HfC(001) and NbC(001)

When TaC(001) was exposed to 200×10^{-4} Pa·s of ethylene gas at the sample temperature of 1100°C, which is the appropriate condition in the (111) surface, no graphite pattern was observed in LEED. No change occurs when the process temperature is varied in the range from 800°C to 1250°C. When the exposure was increased to 5000×10^{-4} Pa·s at the sample temperature of 1250°C, a ring pattern and twelve spots on it appeared in LEED corresponding to an overlayer of graphite. This pattern indicates that the graphite sheet is parallel to the surface, and that the azimuth in the overlayer is partially random and partially epitaxial to the substrate. The epitaxial relationships of the two domains are $[10\bar{1}0]_C \parallel [1\bar{1}0]_{TaC}$ and $[10\bar{1}0]_C \parallel [110]_{TaC}$. In the experiments of HR-EELS and UPS, the condition of 50000×10^{-4} Pa·s at 1500°C is used in order to get a surface thoroughly covered by well-ordered graphite layer. The LEED

pattern is shown in Fig. 3.13. In this sample, the ring became very dilute and only the spots remained, which indicates the overlayer grew almost epitaxially in two domains. The lattice constant a of the overlayer is estimated at 2.46 ± 0.02 Å from the LEED patterns. This value is identical to that of pristine graphite in contrast with the graphite layer on TaC(111). In the LEED pattern, satellite spots are also seen, which again indicate the thinness of the graphite layer.

Fig. 3.13 LEED pattern of graphite covered TaC(001). E_0 = 191.5 eV.

On NbC(001), the graphite layer is successfully formed under the condition: 50000×10^{-4} Pa·s of ethylene exposure at 1250°C. The LEED pattern showed the ring with twelve spots on it. In the case of NbC(001), however, I cannot get the graphite layer by exposing 10000×10^{-4} Pa·s of C_2H_4 at 1500°C. Probably, speed of removing carbon from the surface is

faster on NbC(001) than on TaC(001) at 1500°C. The lattice constant is 2.47 ± 0.01 Å, which is also identical to that of pristine graphite within the error.

In the case of HfC(001), on the contrary, graphite layer is not found in LEED after the exposure of C_2H_4 10000×10^{-4} Pa·s at the temperature of 850°C or 1500°C. When the exposure was increased to 1070000×10^{-4} Pa·s (2.7×10^{-2} Pa for 66 min.) at 1500°C, a diffuse ring pattern was recognized in LEED. This ring had some distribution in the intensity; Namely, the graphite layer is almost randomly oriented although some preferred orientation exists. This sample was examined by ARUPS.

3.2.3. Monolayer graphite on WC(0001) and WC($10\bar{1}0$)

When the as-polished WC(0001) sample was heated in a vacuum, graphite layer was spontaneously formed as mentioned in section 3.1.2. The LEED pattern (Fig. 3.4) shows two-domain incommensurate epitaxial layer of graphite. The epitaxial relationship is $(0001)_C \parallel (0001)_{WC}$ and $[10\bar{1}0]_C \parallel [10\bar{1}0]_{WC}$ for the dominant domain, and $[11\bar{2}0]_C \parallel [10\bar{1}0]_{WC}$ for the minor domain. The lattice constant of the overlayer is estimated at 2.46 Å from the LEED patterns in agreement with pristine graphite. This sample was measured in the HR-EELS experiment.

After cleaning procedure using oxygen gas, WC(0001) shows the $\sqrt{13} \times \sqrt{13}$ (R±13.9°) structure in LEED. By exposing this surface to more than 10000×10^{-4} Pa·s of ethylene at 1000–1500°C, the graphite overlayer can be reproduced and LEED shows the similar pattern to Fig. 3.4.

The clean WC($10\bar{1}0$) showing a 2×2 plus streak pattern in LEED was exposed to ethylene gas at high temperature. When it was exposed to 200×10^{-4} Pa·s of ethylene at 1300°C, the LEED changed a sharp 1×1 pattern. Very weak graphite pattern was recognized in LEED at low energy when the exposure was increased to 1000×10^{-4} Pa·s. Additional

3000×10^{-4} Pa·s ethylene exposure at 1300°C resulted in very complex LEED pattern as shown in Fig. 3.14. This pattern principally consists of substrate fundamentals, two-domain graphite layer's spots and many satellites. The lattice constant is estimated to be 2.47 ± 0.02 Å.

Fig. 3.14 LEED patterns of graphite / WC($10\bar{1}0$). E_0 = 122.8 eV.

There is a complexity in the phonon structure of this sample as described in the section 4.2.4. Two samples were used in the EELS measurement: a sample prepared by exposing 50000×10^{-4} Pa·s of C_2H_4 at 1300°C and a quenched sample after exposing 20000×10^{-4} Pa·s of C_2H_4 at 1500°C. The former shows one set of phonon dispersion curves of the graphite layer but the latter shows two sets simultaneously. When the former sample is flash heated at 1500°C and quenched, it also shows the two sets of phonon. Inversely, when the latter sample is annealed at 1200°C

in a vacuum, one set vanishes and only one set remains. Presumably, the interface structure between the graphite layer and the substrate changes by the heating process. But unfortunately, no difference was recognized in the LEED pattern.

3.2.4. Monolayer graphite on Ni(111) and Ni(001)

In this study, the graphite layer is formed under conditions: 200×10^{-4} Pa·s of C_2H_4 exposure at the sample temperature of 500°C for Ni(111), and 8000×10^{-4} Pa·s at 500°C for Ni(001). As the efficiency of forming graphite on Ni(001) is lower than on Ni(111), more exposure is necessary to form a monolayer on Ni(001). After the exposure, the LEED pattern showed clear 1×1 structure for the C/Ni(111) and diffuse rings around each substrate's fundamental spot for the C/Ni(001) (Fig. 3.15). This comes from the double diffraction, which shows the thinness of the graphite layer.

Fig. 3.15 LEED pattern of graphite / Ni(001). E_0 = 134.6 eV.

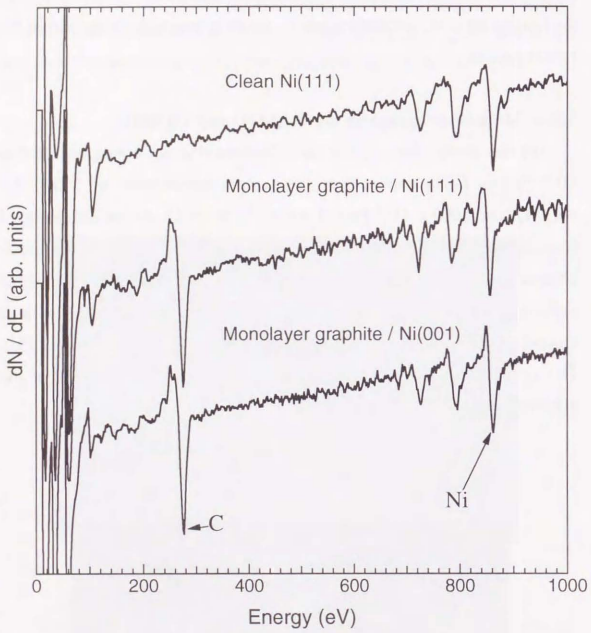

Fig. 3.16 AES spectra of clean and graphite covered Ni surfaces.

The Auger intensity ratio C *KVV* / Ni *LVV* is about 1.6 for Ni(111) and about 1.5 for Ni(001) as shown in Fig. 3.16. The lattice constant of the overlayer is the same as the substrate (a = 2.49 Å) for

C/Ni(111) because of the commensurate structure. In the case of C/Ni(001), the overlayer's lattice constant is estimated at 2.50 ± 0.01 Å from the LEED patterns.

3.2.5. Monolayer graphite on Pt(111)

After cleaning, Pt(111) was exposed to 20×10^{-4} Pa·s of ethylene at the sample temperature of 800°C. Then a ring pattern appeared in LEED, and in AES the peak intensity ratio C/Pt was about 3.0 in the dN/dE spectrum. More 20×10^{-4} Pa·s exposure at 800°C increased the ratio of C/Pt to about 3.8. Even when this surface was exposed to 1000×10^{-4} Pa·s of oxygen gas at room temperature, no trace of oxygen adsorption was observed by AES. The surface is covered by graphite layer completely. The low amount of necessary exposure represents the high efficiency of Pt

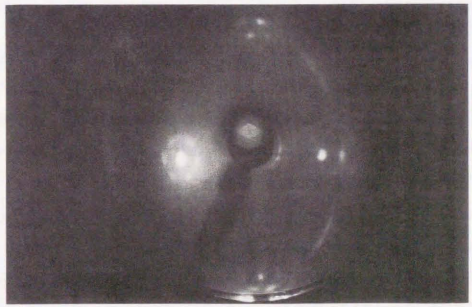

Fig. 3.17 LEED pattern of graphite / Pt(111). E_0 = 75.6 eV.

surface as a catalyst in the cracking reaction.

The ring in the LEED has several segments showing some preferred orientation in the overlayer graphite (Fig. 3.17). It is known that various preferred orientations exist on Pt(111) according to conditions of making graphite layer. The LEED pattern of the sample examined here is the same as that studied by H. Zi-pu *et al.*[22] using LEED intensity analysis. The estimated lattice constant of the graphite layer is 2.46 ± 0.01 Å: identical to that of pristine graphite. Some double diffraction spots are also observed.

3.3. Summary of the graphite formation on metal and TMC surfaces

In summary, Table 3.1 lists the applied conditions to form graphite layer on each substrate, the overlayers' orientations and the lattice constants.

The graphite layer is successfully formed on (111) surfaces of NaCl-type TMC with the exposure to $200–300 \times 10^{-4}$ Pa·s of ethylene at the sample temperatures of 1000-1100°C. On the other hand, it needs 50000×10^{-4} Pa·s on V_a-group TMC(001) [TaC(001) and NbC(001)] and WC(10$\bar{1}$0). For IV_a-group TMC(001) [HfC(001)], so large exposure as 10^2 Pa·s is necessary to make a graphite layer. These differences come from the chemical reactivity of each surfaces. On pure metal surfaces [Pt(111), Ni(111) and Ni(001)], the necessary ethylene exposure is relatively low.

The process temperature is low on the pure metal surfaces because carbon diffuses into the bulk in higher temperature. On the contrary, temperature above 1000°C is appliable on the TMC surfaces. Although the monolayer graphite is producible at lower temperature (~800°C) on the TMC surfaces, a ring pattern: indication of the randomly oriented graphite becomes apparent in LEED patterns. In fact, the graphite layer is oriented randomly on Pt(111) and on Ni(001), which must be produced at such a

Table 3.1 Conditions of graphite formation, orientations and lattice constants.

Substrate	Substrate's lattice constant [Å]	Applied conditions: Temperature [°C]	Applied conditions: Exposure [10^{-4} Pa·s]	Graphite's lattice constant [Å]	Orientation
TaC(111)	3.15	1000	240	2.53 ± 0.02	Two domain ($[10\bar{1}0]_C \parallel [1\bar{1}0]_{TaC}$ / $[11\bar{2}0]_C \parallel [1\bar{1}0]_{TaC}$)
HfC(111)	3.28	1100	200	2.49 ± 0.02	Two domain ($[10\bar{1}0]_C \parallel [1\bar{1}0]_{HfC}$ / $[11\bar{2}0]_C \parallel [1\bar{1}0]_{HfC}$)
NbC(111)	3.16	1100	300	2.52 ± 0.02	Single domain ($[10\bar{1}0]_C \parallel [1\bar{1}0]_{NbC}$)
TiC(111)	3.06	1100	200	2.50 ± 0.02	Single domain ($[10\bar{1}0]_C \parallel [1\bar{1}0]_{TiC}$)
TaC(001)	3.15	1500	50000	2.46 ± 0.02	Two domain ($[10\bar{1}0]_C \parallel [1\bar{1}0]_{TaC}$ / $[10\bar{1}0]_C \parallel [110]_{TaC}$)
HfC(001)	3.28	1500	1×10^6		Random
NbC(001)	3.16	1250	50000	2.47 ± 0.01	Two domain ($[10\bar{1}0]_C \parallel [110]_{NbC}$ / $[10\bar{1}0]_C \parallel [110]_{NbC}$)
WC(0001)	2.91	1500	Spontaneous segregation	2.46 ± 0.03	Two domain ($[10\bar{1}0]_C \parallel [10\bar{1}0]_{WC}$ / $[11\bar{2}0]_C \parallel [10\bar{1}0]_{WC}$)
WC(10$\bar{1}$0)	2.84×2.91	1300	50000	2.47 ± 0.02	Two or four domain
Ni(111)	2.49	500	200	2.49	Commensurate with the substrate ($[11\bar{2}0]_C \parallel [1\bar{1}0]_{Ni}$)
Ni(001)	2.49	500	8000	2.50 ± 0.01	Random
Pt(111)	2.91	800	40	2.46 ± 0.01	Random

low temperature. The high process temperature probably causes the good epitaxy of the monolayer graphite on the TMC surfaces.

4. Phonon dispersion relations of the monolayer graphite on metal and TMC surfaces

4.1. Measurements of phonon dispersion by high-resolution electron energy loss spectroscopy (HR-EELS)

The principle of measuring phonon dispersion by means of HR-EELS is briefly described in this section. Figure 4.1 shows geometry of the process. When an electron having an initial kinetic energy E_0 and an incident angle θ_0 creates one surface phonon whose frequency and wave vector parallel to the surface are ω and $\boldsymbol{k}_{\parallel}$, respectively, the emergent electron's energy E_f and angle θ_f satisfies the energy and momentum conservation laws as follows:

$$\hbar\omega = E_0 - E_f \tag{4.1}$$

and

$$\hbar k_{\parallel} = \sqrt{2mE_0}\sin\theta_0 - \sqrt{2mE_f}\sin\theta_f \ . \tag{4.2}$$

If the surface ordering is so good that the surface phonon dispersion relation $\omega(\boldsymbol{k}_{\parallel})$ is well defined, only electrons having E_f are detected by

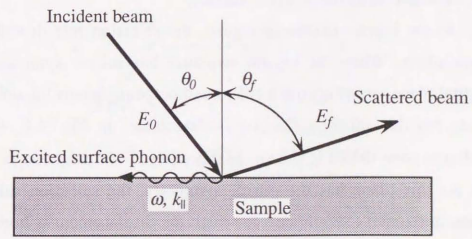

Fig. 4.1 Geometry of the electron energy loss process with creation of one surface phonon.

the analyzer seeing the sample at the fixed angle θ_f and make a so-called "loss peak" in the energy spectrum under the one-phonon creation process. In other words, we can determine experimentally $\omega(k_{\parallel})$ from the EELS spectra. In this study, the incidence angle θ_0 is changed to vary $k_{\parallel}$, while θ_f is fixed at 72°.

In the EELS, two mechanisms are known of the electron scattering by lattice vibrations:[25] dipole scattering and impact scattering. In the dipole scattering regime, electrons are scattered inelastically within a small angle by a vibrating dipole field. The scattered electron can be observed therefore only around the diffraction beams. On the other hand, the impact scattering is caused by the scattering of electrons by individual atoms, and electrons are really scattered to various directions.

To the dipole scattering regime, only dipole active modes are responsive, which means the vibrational modes producing the fluctuation of dipole field perpendicular to the surface. Because the substrate is metallic, microscopic dipole parallel to the surface is compensated by the image charge. In the concrete, the dipole active mode is a long-wavelength (near $\overline{\Gamma}$ in the surface BZ) optical mode in which the displacement has perpendicular component to the surface.

In the impact scattering regime, the selection rule described below takes place. When the crystal structure has mirror symmetry for the sagittal plane, on which the incident and outgoing beams lie, only the even mode for this mirror-reflection is detectable. In Fig. 4.2, the surface Brillouin zone (SBZ) is shown. In this study, $\overline{\Gamma}$–$\overline{M}$ direction is shed light on. As this plane has the mirror symmetry, the selection rule is alive. Shear horizontal (SH) modes, in which the displacement is horizontal and perpendicular to the sagittal plane, are odd for the reflection operation and should not be detected in the experimental condition here.

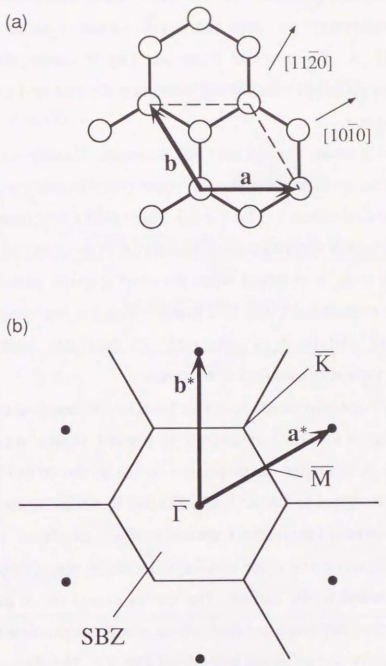

Fig. 4.2 (a) Unit cell and (b) surface Brillouin zone of graphite.

4.2. Experimental results of HR-EELS

4.2.1. Monolayer graphite on TaC(111) and TaC(001)

The measurement was done along [1$\bar{1}$0] of the substrate for graphite on TaC(111). As the graphite layer has two domains, this direction correspond to [10$\bar{1}$0] ($\bar{\Gamma}$–$\bar{M}$) for the dominant domain and [11$\bar{2}$0] ($\bar{\Gamma}$–$\bar{K}$) for the minor one.

Figure 4.3 shows the specular EELS spectra. Usually no loss peak is observed at the specular condition. In some experimental conditions, loss peaks appeared as shown in Fig. 4.3 (b). These peaks are phonon modes of monolayer graphite displaced perpendicularly to the surface. Above 200 meV, no loss peak is observed when the clear graphite pattern is seen in LEED. As is evident from this, C-H bond, which has the stretching energy ranging from 350 meV to 400 meV, is perfectly broken and no hydrocarbon molecule remains on the surface.

In the off-specular conditions, five branches of loss peaks appeared as shown in Fig. 4.4. The loss energy is plotted versus wave numbers calculated by (4.2) to give the dispersion curves as shown in Fig. 4.5. Five branches are assigned as LA, LO, ZA, ZO and R, which mean longitudinal acoustic-like mode, longitudinal optical mode, z-displaced acoustic-like mode, z-displaced optical mode and Rayleigh mode, respectively. Here "z" is the axis normal to the surface. The modes except the R mode are the phonon modes of the graphite layer, whose atomic displacement at $\bar{\Gamma}$ point are schematically shown in the left side of Fig. 4.5. The Rayleigh mode is an acoustic surface phonon mainly localized in the outermost substrate layer.[57] As two carbon atoms exist in one unit cell of the monolayer graphite, six modes may appear. Within the six mode, two transverse mode "SHA" and "SHO" (shear-horizontal acoustic-like mode and shear-horizontal optical mode) is not observed under this experimental condition

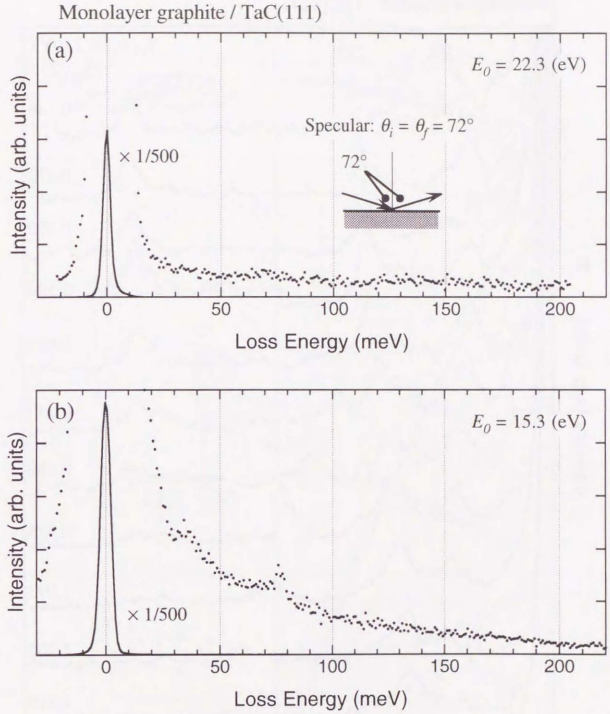

Fig. 4.3 Specular EELS spectra of graphite covered TaC(111).

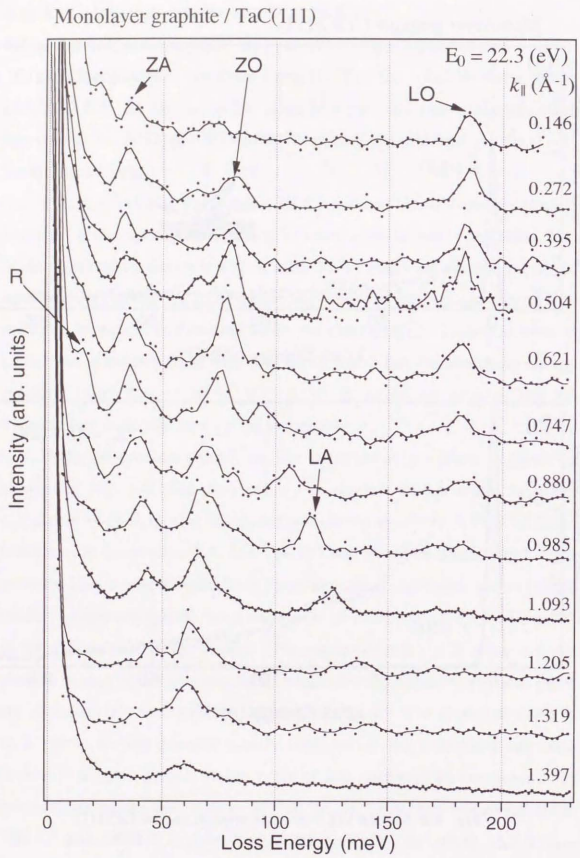

Fig. 4.4 Off-specular EELS spectra for graphite covered TaC(111).

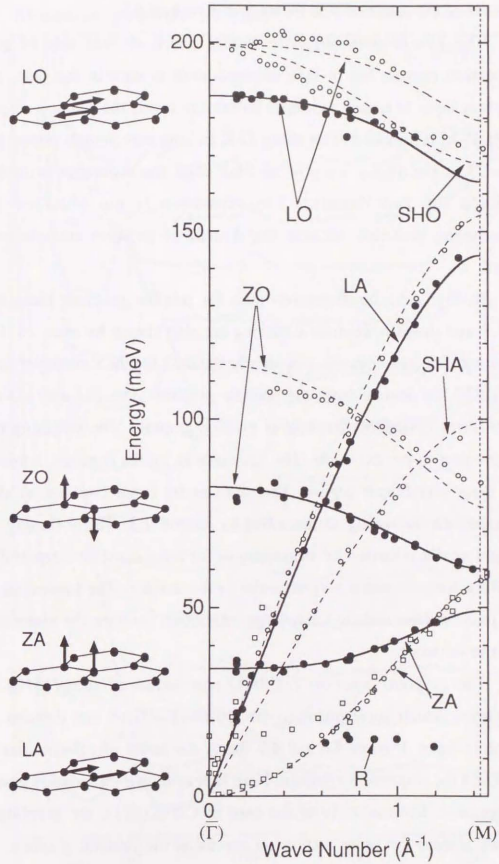

Fig. 4.5 Phonon dispersion relations of monolayer graphite on TaC(111). Experimental data are indicated by dots and solid lines are calculation by the force constant model fitted to the data. Dispersions of bulk graphite are also shown by open circles and broken lines for comparison.

because of the selection rule mentioned in section 4.1.

The two-domain structure should result in two sets of phonon dispersion curves, but in fact, no separation is seen in the data. As the graphite layer is highly isotropic within the layer, the phonon dispersion along $\bar{\Gamma}$–$\bar{M}$ is similar to that along $\bar{\Gamma}$–$\bar{K}$ in long wavelength region (up to 1/2–2/3 of the SBZ). Only at the SBZ edge, the separation would occur between the two domains. The separation is not observed in the experiment, probably because one domain is stronger enough than the other.

In Fig. 4.5, the dispersion data for pristine graphite measured by EELS and inelastic neutron scattering are also shown by open circles and open squares, respectively. Apparently the data for the monolayer graphite on TaC(111) deviate from the pristine graphite. The ZO and LO modes have lower frequency than that of pristine graphite. The softening ratio is the greatest in the ZO mode. The ZA mode is, on the contrary, hardened in the long wavelength region. The analysis by force constant model has revealed the following as described in section 4.3; The softening of the optical modes is caused by weakening of the force constants, especially of a bending force constant perpendicular to the surface. The hardening of the ZA mode corresponds to fairly large interaction between the graphite layer and the substrate.

The graphite layer on TaC(001) was measured along [110] of the substrate, which corresponds to the [$1\bar{1}0$] ($\bar{\Gamma}$–$\bar{M}$) of one domain in the graphite layer. Figures 4.6 and 4.7 shows the series of off-specular EELS data and the dispersion relations. Here is also shown the pristine graphite's dispersions. Contrastively to the case of C/TaC(111), the graphite layer shows almost the same dispersion curves as the pristine graphite. Small differences is seen especially on the ZA mode near the $\bar{M}$ point. This is caused by softening in the long-range force constant like a twisting force

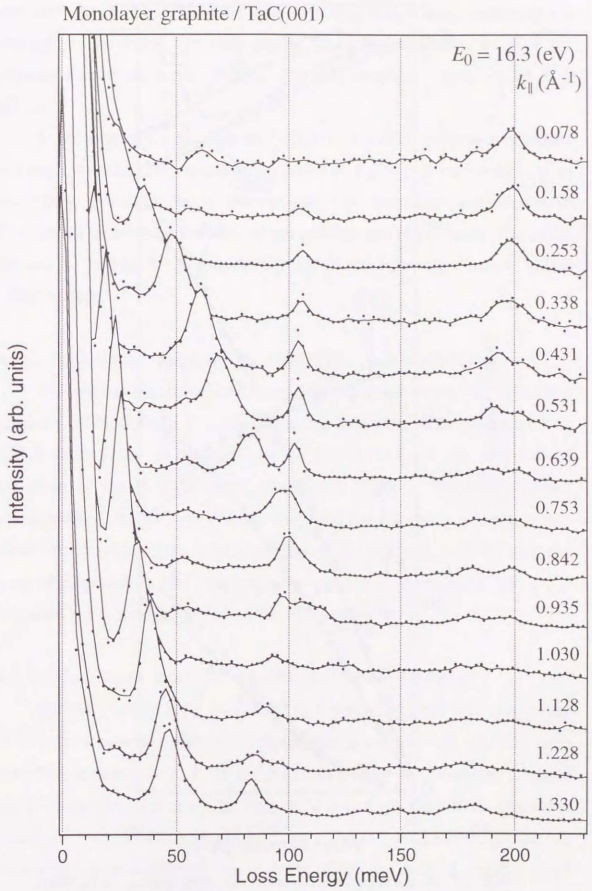

Fig. 4.6 Off-specular EELS spectra of graphite covered TaC(001).

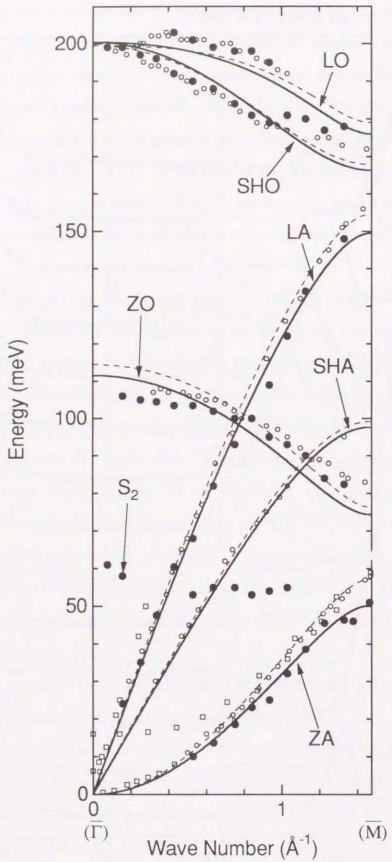

Fig. 4.7 Phonon dispersion relations of monolayer graphite on TaC(001). Experimental data are indicated by dots and solid lines are calculation by the force constant model fitted to the data. Dispersions of bulk graphite are also shown by open circles and broken lines for comparison.

constant. As will be described later, the long range force constants are inclined to be weak generally in the monolayer graphite, even if the phonon dispersion seems to resemble that of pristine graphite at first glance.

In the case of the graphite on TaC(001), the SHO mode was observed although weakly. This mode is inhibited in the EELS under the mirror symmetry. Probably, the mirror symmetry is microscopically broken in this system because of the incommensurability to the substrate. The mode labeled S_2 in Fig. 4.7 is a surface mode of the substrate's carbon called "Wallis mode".[58,59]

4.2.2. Monolayer graphite on NbC(111) and NbC(001)

The similar measurements were done for graphite on NbC(111) and graphite on NbC(001); Phonon dispersion relations were determined by EELS along [1$\bar{1}$0] of the substrate on C/NbC(111), which is the $\bar{\Gamma}$–$\bar{M}$ direction of the graphite layer, and along [110] of NbC(001), which corresponds $\bar{\Gamma}$–$\bar{M}$ for one domain and $\bar{\Gamma}$–$\bar{K}$ for the other domain of the overlayer graphite. The results are shown in Figs. 4.8–4.11. In also the case of graphite on NbC surfaces, the phonon is changed on the (111) substrate but scarcely changed on the (001) substrate.

4.2.3. Monolayer graphite on HfC(111) and TiC(111)

For the graphite layer on HfC(111), the measurement was done along [1$\bar{1}$0] of the substrate. As the graphite layer is two-domain structure, this direction corresponds to $\bar{\Gamma}$–$\bar{M}$ for the main part of the overlayer graphite but $\bar{\Gamma}$–$\bar{K}$ for the other part. In Figs. 4.12 and 4.13, the EELS result and determined phonon dispersions are shown. The softening in the ZO and LO modes also occurs although the quantity of the deviation is slightly small compared with C/TaC(111) and C/NbC(111).

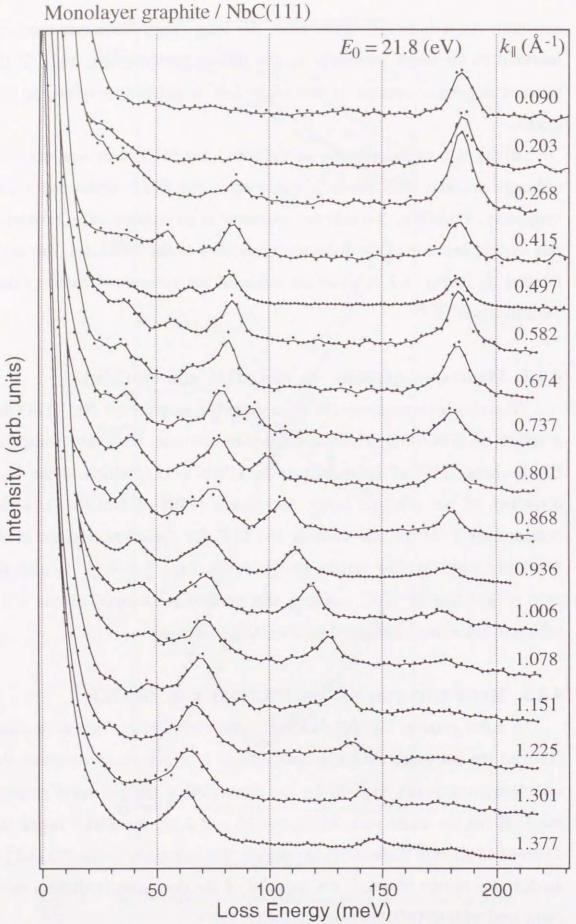

Fig. 4.8 Off-specular EELS spectra of graphite covered NbC(111).

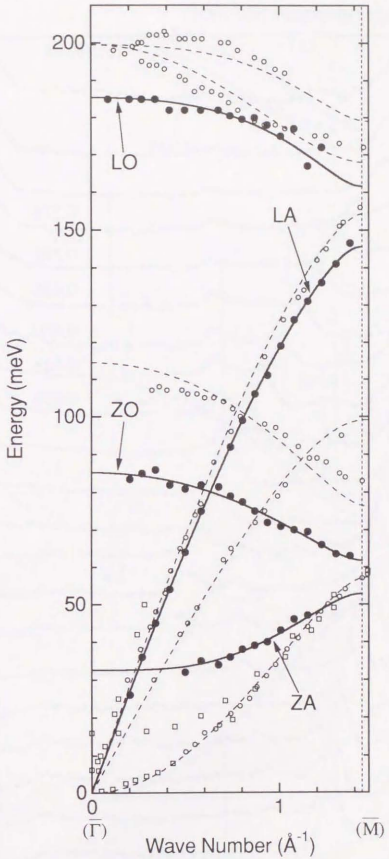

Fig. 4.9 Phonon dispersion relations of monolayer graphite on NbC(111). Experimental data are indicated by dots and solid lines are calculation by the force constant model fitted to the data. Dispersions of bulk graphite are also shown by open circles and broken lines for comparison.

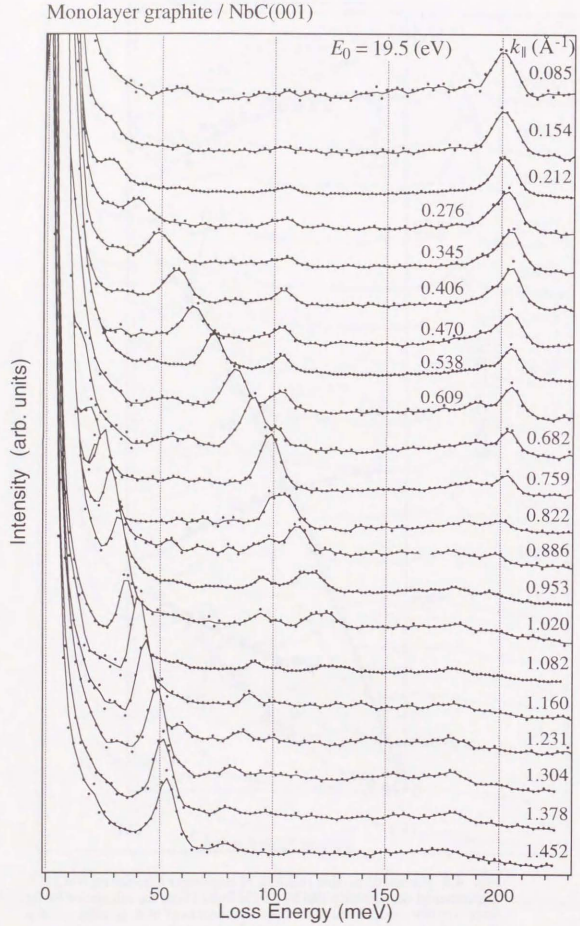

Fig. 4.10 Off-specular EELS spectra of graphite covered NbC(001).

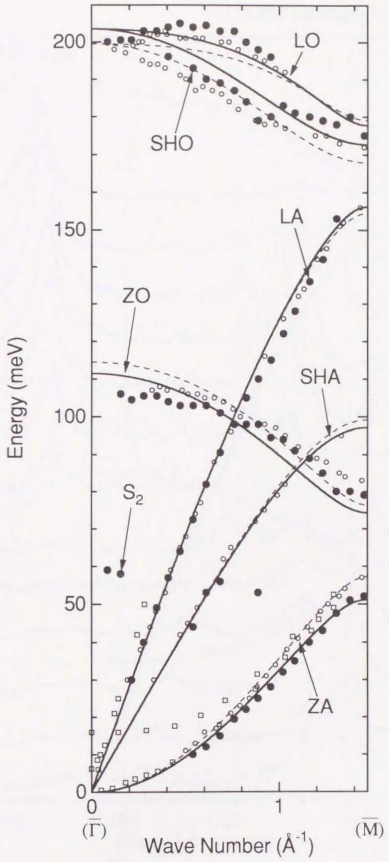

Fig. 4.11 Phonon dispersion relations of monolayer graphite on NbC(001). Experimental data are indicated by dots and solid lines are calculation by the force constant model fitted to the data. Dispersions of bulk graphite are also shown by open circles and broken lines for comparison.

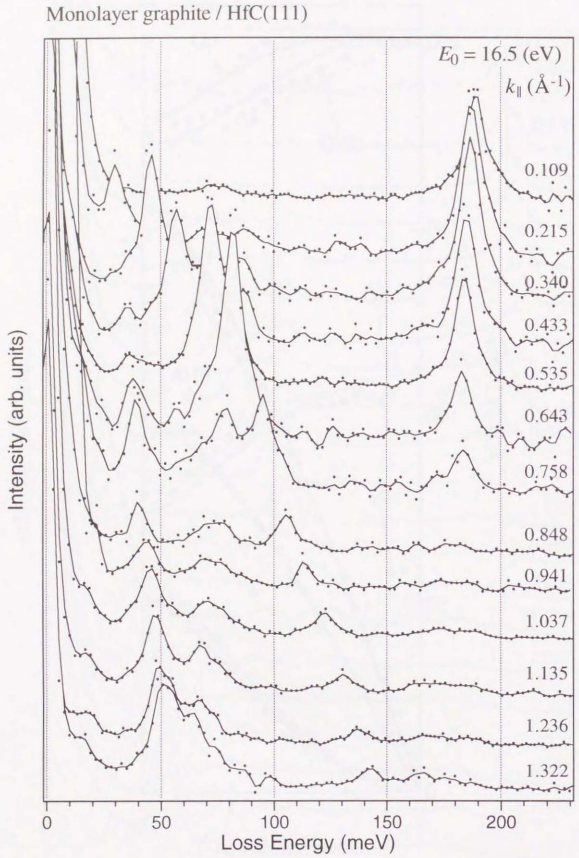

Fig. 4.12 Off-specular EELS spectra of graphite covered HfC(111).

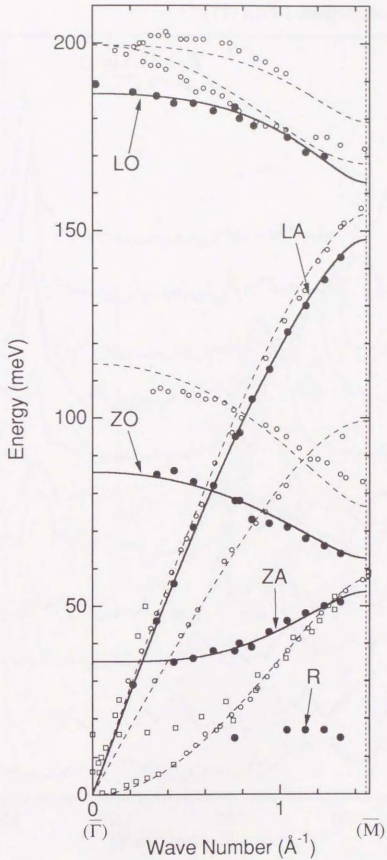

Fig. 4.13 Phonon dispersion relations of monolayer graphite on HfC(111). Experimental data are indicated by dots and solid lines are calculation by the force constant model fitted to the data. Dispersions of bulk graphite are also shown by open circles and broken lines for comparison.

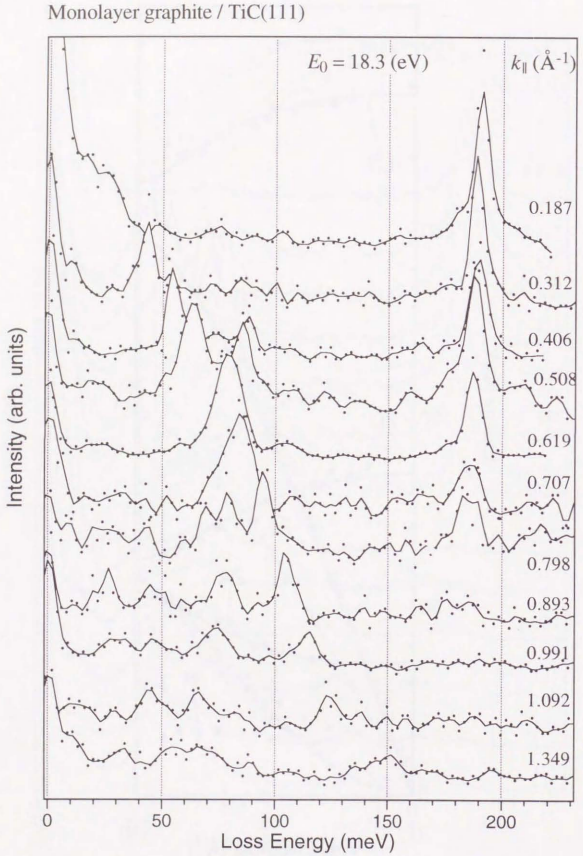

Fig. 4.14 Off-specular EELS spectra of graphite covered TiC(111).

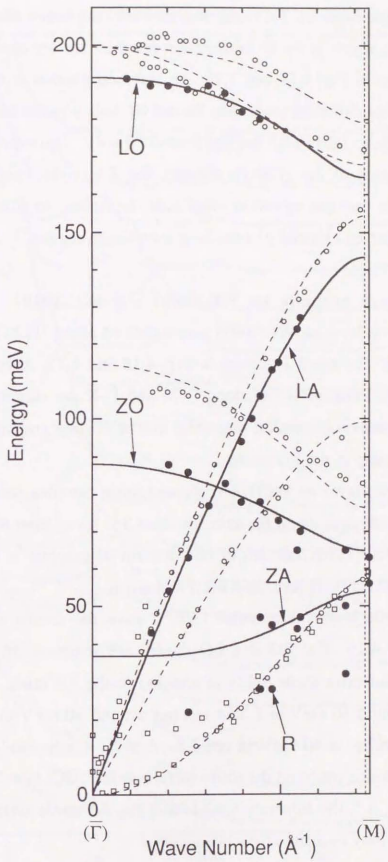

Fig. 4.15 Phonon dispersion relations of monolayer graphite on TiC(111). Experimental data are indicated by dots and solid lines are calculation by the force constant model fitted to the data. Dispersions of bulk graphite are also shown by open circles and broken lines for comparison.

The graphite layer on TiC(111) was similarly measured along [1$\bar{1}$0] of the substrate, which is the $\bar{\Gamma}$–$\bar{M}$ direction for this one-domain graphite layer. As shown in Fig. 4.14 and 4.15, the softened phonon is observed. Because Ti has much lighter mass than Ta and Hf, bulk phonon band of the substrate spreads to fairly high energy around 50 meV. Consequently, the low energy branch of the graphite phonon, the ZA mode, becomes the resonance mode and the vibration amplitude decreases, so that the ZA mode is not observed especially in the long wavelength region.

4.2.4. Monolayer graphite on WC(0001) and WC(10$\bar{1}$0)

The graphite layer on WC(0001) was measured along [11$\bar{2}$0] azimuth of the substrate. The result is shown in Fig. 4.16 and 4.17. According as the two domains exist, both sets along $\bar{\Gamma}$–$\bar{M}$ and $\bar{\Gamma}$–$\bar{K}$ are simultaneously observed. The phonon dispersion resembles that of pristine graphite except for a little softening in the ZO mode.

The graphite layer on WC(10$\bar{1}$0) showed more complex results. The measurement were done along the azimuth about 15° away from the [1$\bar{2}$10] (a-axis), to which [10$\bar{1}$0] azimuth of one domain of graphite is directed; Namely, $\bar{\Gamma}$–$\bar{M}$ direction is measured for that domain.

The graphite layer made under 1300°C gave the results shown in Figs. 4.18 and 4.19. The ZO and LO modes are softened. In the low energy region, an extra mode exists in addition to the ZA mode. The ZA mode starts around 30 meV at $\bar{\Gamma}$ and reaches around 50 meV at $\bar{M}$. The mode which begins at 60 meV is considered to be a substrate's carbon mode like the Wallis mode on the (001) surface of the NaCl-type TMC. At around $k_{\parallel} \sim 1.0$ Å^{-1}, the substrate's mode and the ZA mode interact with each other, and may exchange their characters.

The graphite layer quenched from 1500°C showed more complex

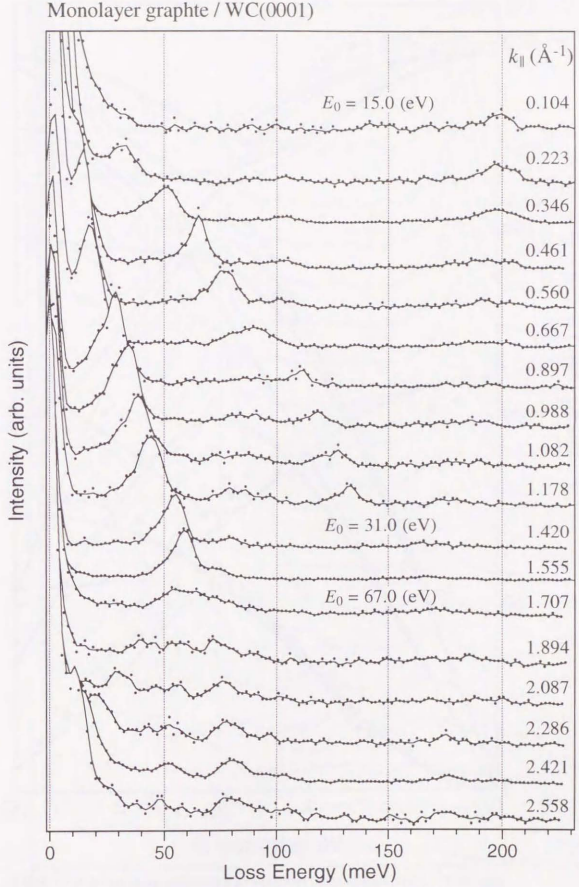

Fig. 4.16 Off-specular EELS spectra of graphite covered WC(0001).

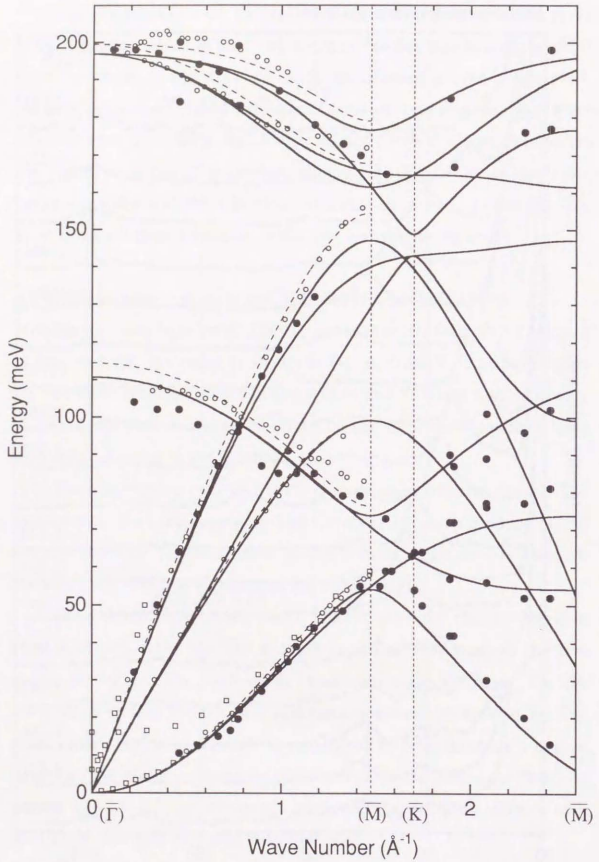

Fig. 4.17 Phonon dispersion relations of monolayer graphite on WC(0001). Experimental data are indicated by dots. Theoretical curves are indicated by solid curves along both Γ̄–M and Γ̄–K–M azimuthes. The data for bulk graphite are also shown for comparison.

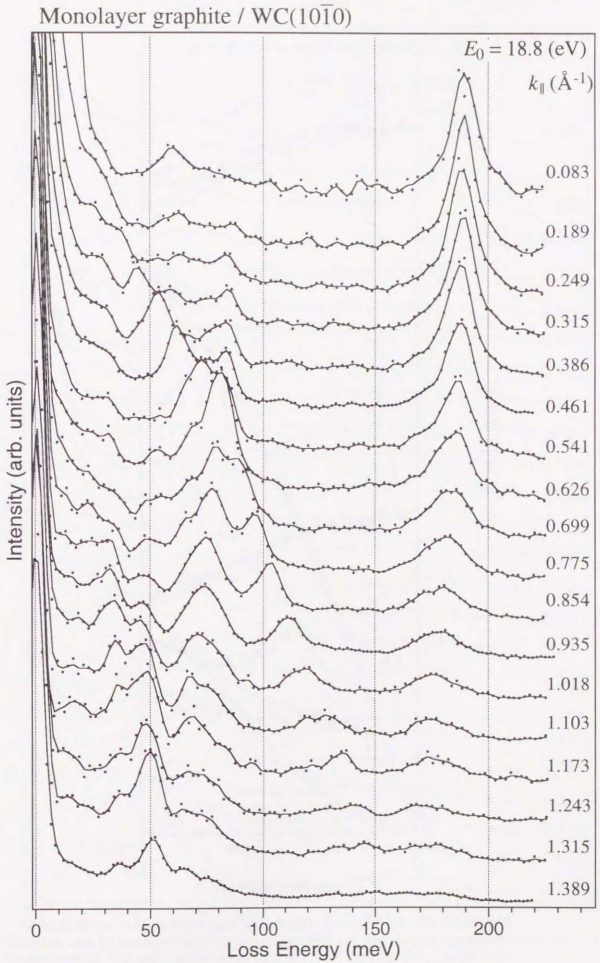

Fig. 4.18 Off-specular EELS spectra of monolayer graphtite on WC(10$\bar{1}$0) made at 1300°C.

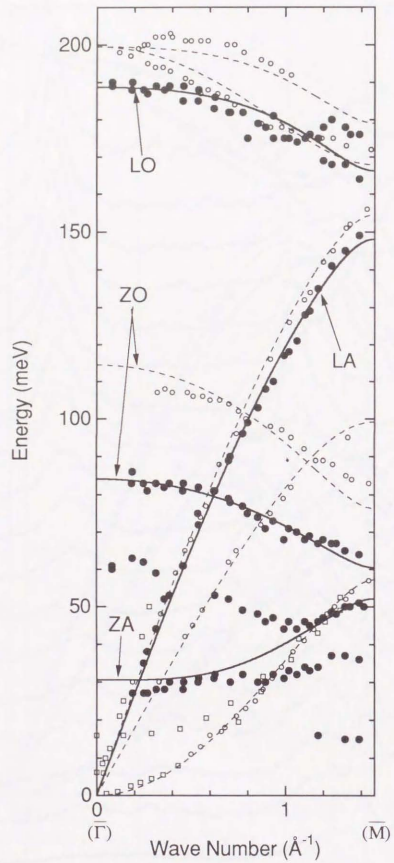

Fig. 4.19 Phonon dispersion relations of monolayer graphite on WC(10$\bar{1}$0). The sample is made at 1300°C. Experimental data are indicated by dots and solid lines are calculation by the force constant model fitted to the data. Dispersions of bulk graphite are also shown by open circles and broken lines for comparison.

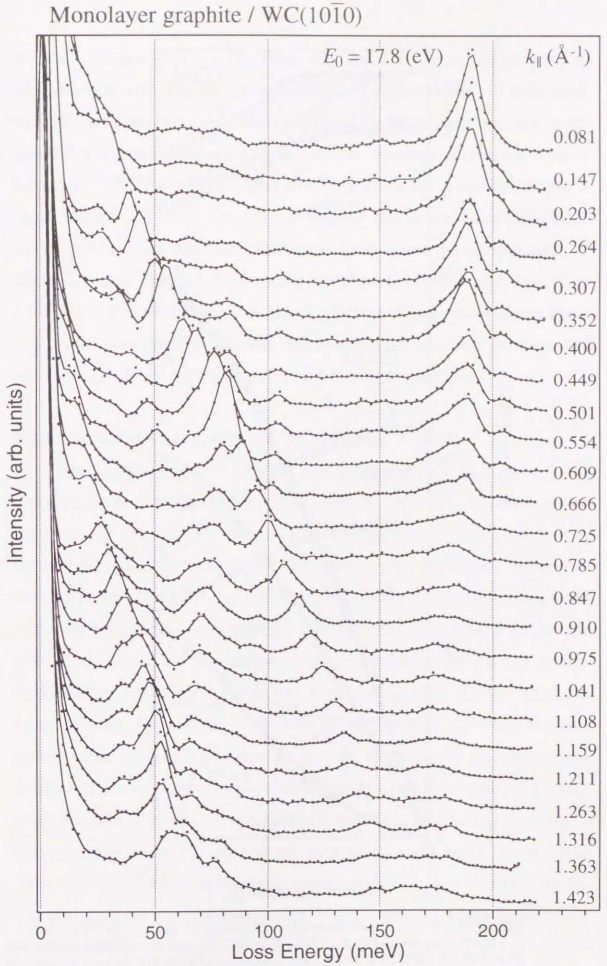

Fig. 4.20 Off-specular EELS spectra of monolayer graphite on WC(10$\bar{1}$0) quenched from 1500°C.

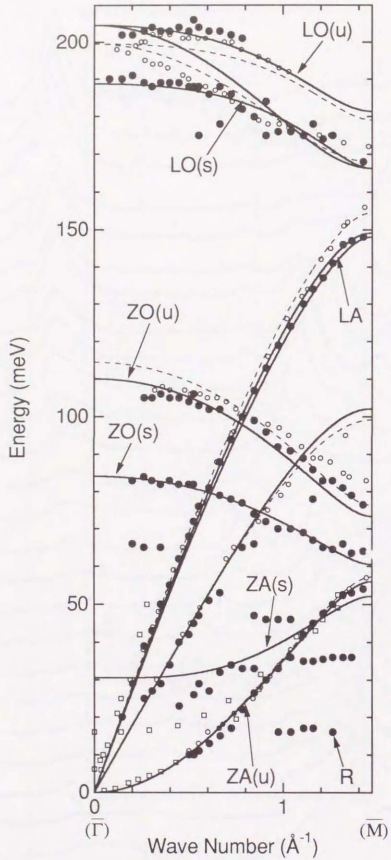

Fig. 4.21 Phonon dispersion relations of monolayer graphite on WC(10$\bar{1}$0). The sample is quenched from 1500°C. Experimental data are indicated by dots and solid lines are calculation by the force constant model fitted to the data. Dispersions of bulk graphite are also shown by open circles and broken lines for comparison.

results. The data are shown in Figs. 4.20 and 4.21. In the EELS spectra, the same softened branches (s) and the unsoftened branches (u) with weak intensity are simultaneously detected. Even the SHA mode appears in the not-softened group. The unsoftened branches disappear after the sample is heated at 1200°C in vacuum, and re-appear when the annealed sample is again flashed at 1500°C for 100 s in vacuum and quenched, although the intensity is weaker than the initial state. Even when the sample made at 1300°C, which shows only the softened phonon branches, are heated to 1500°C for 100 s and quenched, the unsoftened modes appear. From these results, the heat process is considered to affect the interface structure and subsequently the phonon structure in the overlayer graphite.

4.2.5. Monolayer graphite on Ni(111) and Ni(001)

The graphite covered Ni(111) was measured by EELS along [11$\bar{2}$] azimuth of the substrate, which corresponds to [10$\bar{1}$0] ($\bar{\Gamma}$-$\bar{M}$ direction) of the overlayer graphite. For the graphite layer on Ni(001), the azimuth was set to [100] of the substrate, to which direction exists the intense segment of the ring pattern in LEED, i.e. one domain of overlayer graphite having the preferred orientation was aligned to $\bar{\Gamma}$-$\bar{M}$ direction. The results are shown in Fig. 4.22 and 4.23. The phonon dispersion relations are plotted in Fig. 4.24 together. On both substrates, the monolayer graphite shows almost the same phonon dispersions. The SHA mode appears only on Ni(001) probably because the orientation is random. Similarly to the case of the graphite layer on TMC(111) surfaces, the ZO and LO modes are fairly softened. The ZA mode goes into the bulk phonon band, becomes a resonance mode and vanishes in the long wavelength region. In order to consider the substrate effect more exactly, analysis based on a slab model was also done for this commensurate C/Ni(111) system, which is described in section 4.3.5.

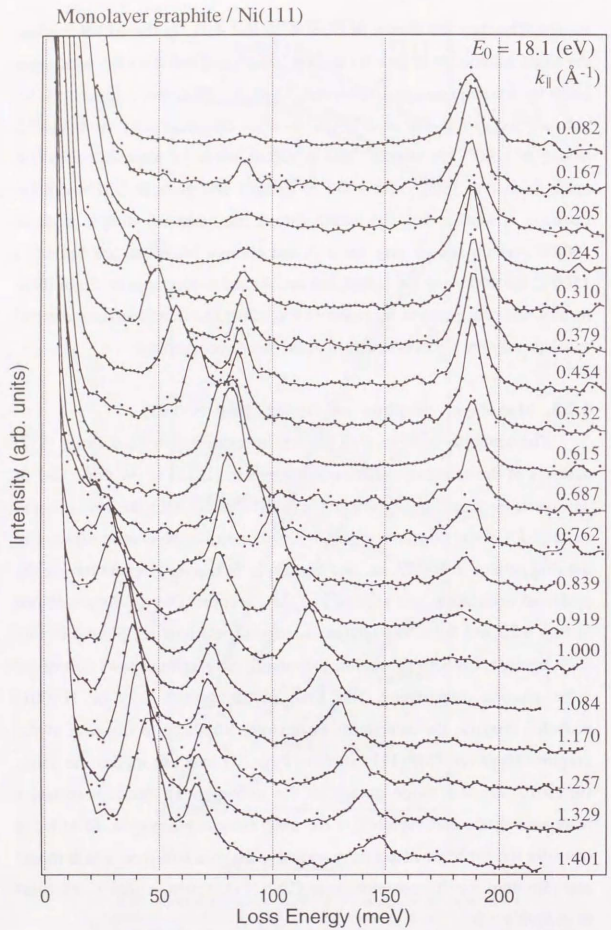

Fig. 4.22 Off-specular EELS spectra of graphite covered Ni(111).

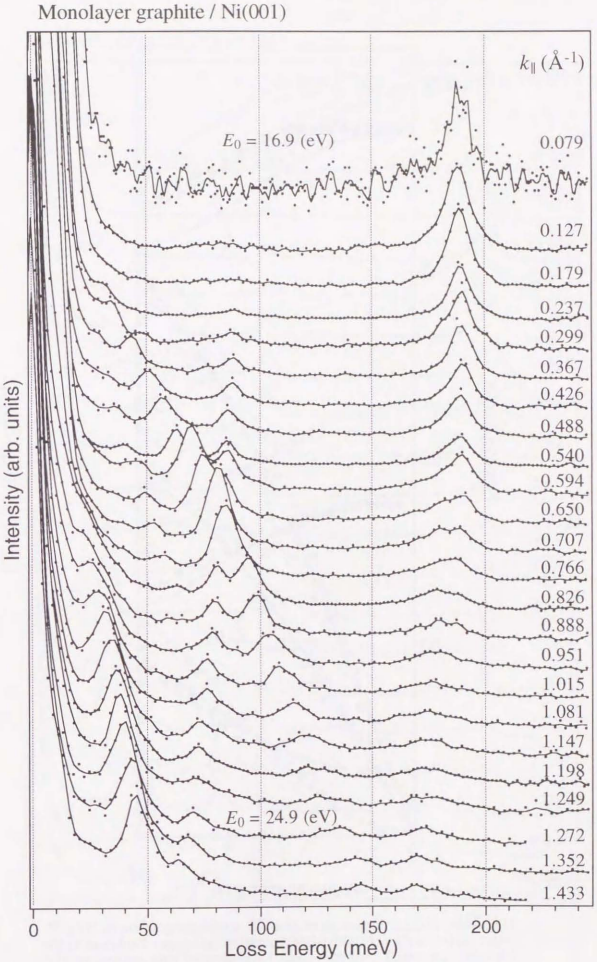

Fig. 4.23 Off-specular EELS spectra of graphite covered Ni(001).

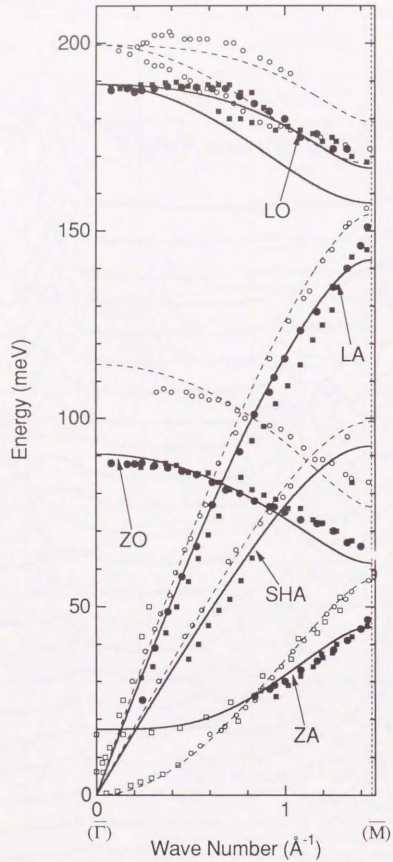

Fig. 4.24 Phonon dispersion relations of monolayer graphite on Ni(111) (solid circles) and on Ni(001) (solid squares). Curves are calculation by the force constant model fitted to the data. Dispersions of bulk graphite are also shown by open marks and broken lines.

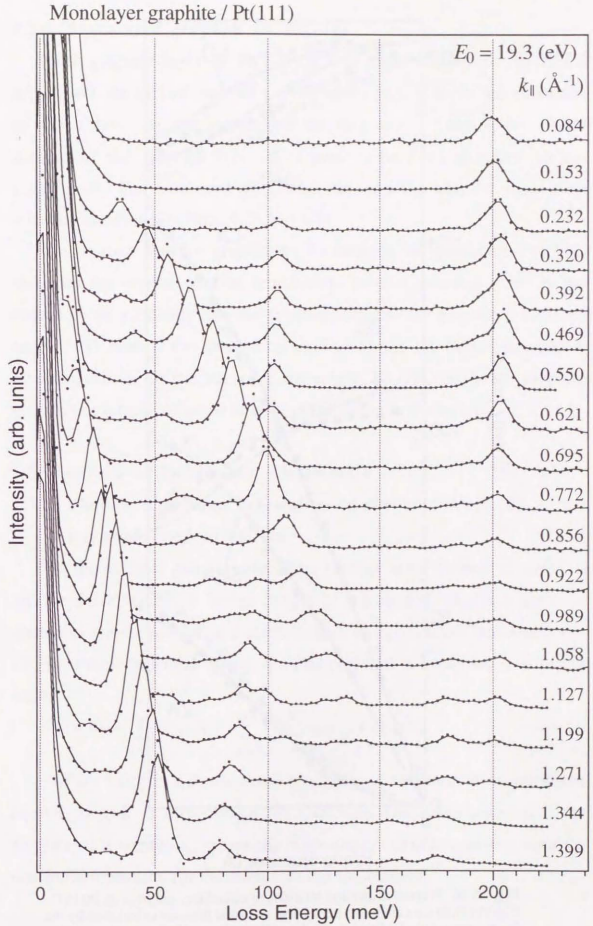

Fig. 4.25 Off-specular EELS spectra of graphite covered Pt(111).

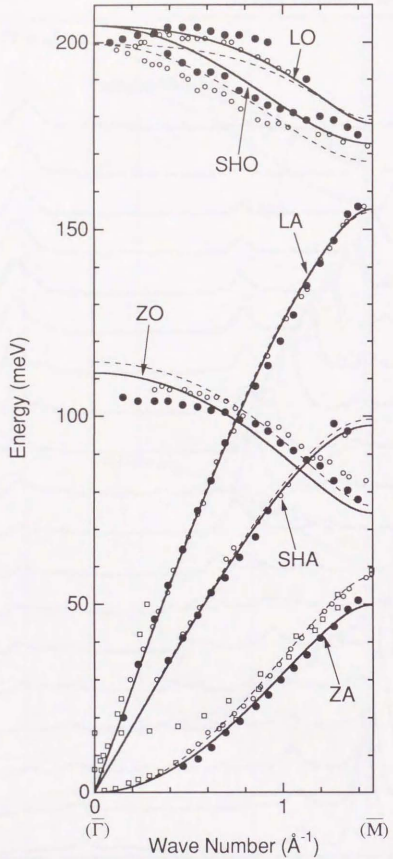

Fig. 4.26 Phonon dispersion relations of monolayer graphite on Pt(111). Experimental data are indicated by dots and solid lines are calculation by the force constant model fitted to the data. Dispersions of bulk graphite are also shown by open circles and broken lines for comparison.

4.2.6. Monolayer graphite on Pt(111)

The graphite layer on Pt(111) is randomly oriented. In the EELS experiment, the azimuth was set to 5–10° away from [1$\bar{1}$0] of the substrate, to which direction one segment of the ring exists. That is, one major domain of the graphite layer is aligned to be $\bar{\Gamma}$–$\bar{M}$ direction in the experiment. The measured EELS spectra and the phonon dispersion relations are shown in Figs. 4.25 and 4.26.

In contrast with the graphite on Ni surfaces, the graphite on Pt(111) indicates the similar phonon structure to pristine graphite. This is not caused by the randomly oriented structure, because the graphite is softened on Ni(001) even if the orientation is random and the lattice constant is incommensurate to the substrate. Inversely, on TaC(001), the graphite layer is not largely softened in spite of the epitaxial formation.

4.3. Analysis of the phonon dispersion

4.3.1. Phonon dispersion calculation in the framework of harmonic approximation

In this section, phonon calculation method using dynamical matrix is briefly described.[60] In lattice dynamics calculation, adiabatic approximation is usually adopted and the electronic energy is taken into account as an interatomic potential energy Φ. This potential is expanded in a Taylor series:

$$\Phi = \Phi_0 + \sum_{i,\alpha} \Phi_{i\alpha} u_{i\alpha} + \sum_{i,\alpha,j,\beta} \Phi_{i\alpha j\beta} u_{i\alpha} u_{j\beta} + O(u^3), \qquad (4.3)$$

where i or j is a discrimination number of the particle in the whole crystal, α or β is direction in the Cartesian coordinates, and **u** is the displacement vector. $u_{i\alpha}$ means the α component of displacement from the equilibrium position for the atom i. In the summations,

$$\Phi_{i\alpha} \equiv \left[\frac{\partial \Phi}{\partial u_{i\alpha}}\right]_0 \tag{4.4}$$

and $$\Phi_{i\alpha j\beta} \equiv \left[\frac{\partial^2 \Phi}{\partial u_{i\alpha} \partial u_{j\beta}}\right]_0 \quad . \tag{4.5}$$

Here the subscript 0 means the value at the equilibrium position. When the crystal is stable, each atom should not accept any force at its equilibrium position, i.e. all $\Phi_{i\alpha}$ should be zero. In the harmonic approximation, the higher order term $O(u^3)$ is neglected. Then the force on the atom i is given:

$$f_{i\alpha} = -\frac{\partial \Phi}{\partial u_{i\alpha}} = -\sum_{j,\beta} \Phi_{i\alpha j\beta} u_{j\beta} \quad . \tag{4.6}$$

Now the equations of motion are:

$$M_i \frac{d^2}{dt^2} u_{i\alpha} = -\sum_{j,\beta} \Phi_{i\alpha j\beta} u_{j\beta} \quad , \tag{4.7}$$

where M_i is the mass of atom i. In the crystal considered here, two-dimensional periodicity takes place, and therefore the normal mode solutions of (4.7) have the form of Bloch functions:

$$\mathbf{u}_i = \frac{\mathbf{v}_k}{\sqrt{M_k}} \exp\{i\,(\mathbf{r}_i \cdot \mathbf{k}_{\parallel} - \omega t)\} \quad , \tag{4.8}$$

where $\mathbf{r}_i$ is the equivalent position of the atom i, $\mathbf{k}_{\parallel}$ is a wave vector parallel to the surface, and ω is the vibration frequency. Eigenvectors $\mathbf{v}_k$ is thought only for different kinds of atoms in a two-dimensional unit cell. In a crystal, $\{\mathbf{r}_i\}$ is periodic points, so that $\{\mathbf{u}_i\}$ is periodic in $\mathbf{k}_{\parallel}$ space. Therefore we consider the first surface BZ in $\mathbf{k}_{\parallel}$ space. In equation (4.7), summation of j spreads all atoms in the crystal. Now we change the summation:

$$\sum_{j \in \text{ crystal}} \rightarrow \sum_{\text{all cells}} \left(\sum_{l \in \text{ unit cell}} \right) \rightarrow \sum_{l \in \text{ unit cell}} \left(\sum_{l \text{ atom in all cells}} \right) . \tag{4.9}$$

Here l denotes the kind of an atom. Applying (4.8) and (4.9) into eq. (4.7), we get:

$$\omega^2 v_{k\alpha} = \sum_{l,\beta} \frac{v_{l\beta}}{\sqrt{M_k M_l}} \sum_{j = l \text{ atom in all cells}} \Phi_{i\alpha j\beta} \exp(i\, \mathbf{r}_{ij} \cdot \mathbf{k}_{\parallel}) \quad , \tag{4.10}$$

where $\mathbf{r}_{ij} = \mathbf{r}_j - \mathbf{r}_i$. The problem has changed to an eigenproblem for the so-called dynamical matrix:

$$D_{k\alpha l\beta} = \frac{1}{\sqrt{M_k M_l}} \sum_{j = l \text{ atom in all cells}} \Phi_{i\alpha j\beta} \exp(i\, \mathbf{r}_{ij} \cdot \mathbf{k}_{\parallel}) \quad . \tag{4.11}$$

As $\Phi_{i\alpha j\beta}$ is invariant for simultaneous translation of the two atoms (i and j) from cell to cell, the atom i can be fixed at any k atom in the crystal.

4.3.2. Model potential

In this section, definitions of the original force constants (FC) describing bonds in graphite are given. Usually, Born-von Karman model (BK model) has been used for phonon analysis. For graphite, some works are found in the literature.[34,61,62] This model works quite well for materials having isotropic interaction between atoms, like fcc metals and inert-gas solid for example. But for covalent solid, many long range FC's are needed to reproduce the measured phonon dispersion relations, because the FC in the BK model is not directional while the real covalent bond is highly directional. It is very difficult to deduce physical meaning from such a lot of parameters. Here I have constructed a phenomenological FC model specific to the monolayer graphite. The parameters in the model have clear physical meanings.

Six FC's are defined to present the bonding nature: a nearest neighbour stretching FC α_1, a second nearest one α_2, an in-plane bond-bending FC γ_1, an out-of-plane bond-bending FC γ_2, a bond-twisting FC δ, and a stretching FC α_s between the carbon and the substrate. Here the substrate is assumed to be a structureless wall having infinite mass. The terms in the model Hamiltonian are defined using the six parameters as follows;

(i) Stretching terms

The stretching FC term between an atom i and an atom j in Fig. 4.27 (a) is expressed:

$$\frac{\alpha}{2}\left\{\frac{(\mathbf{u}_j-\mathbf{u}_i)\cdot\mathbf{r}_{ij}}{|\mathbf{r}_{ij}|}\right\}^2 , \tag{4.12}$$

where α is the nearest-neighbor FC (α_1) when the atoms i and j are the nearest neighbors, and α_2 when the second nearest neighbors. $\mathbf{u}_i$ indicates the displacement vector of the atom i, and $\mathbf{r}_{ij}$ the relative mean-position of the atom j from the atom i. One carbon atom has three nearest neighbors and six second-nearest neighbors. Each terms are expressed in Appendix A.1.

(ii) In-plane bending terms

The term of in-plane bending FC γ_1, which works to keep the angle ∠jik in Fig. 4.27 (b) constant, is expressed:

$$\frac{\gamma_1}{2}\left[\left\{\frac{(\mathbf{u}_j-\mathbf{u}_i)\times\mathbf{r}_{ij}}{|\mathbf{r}_{ij}|^2}\right\}_z - \left\{\frac{(\mathbf{u}_k-\mathbf{u}_i)\times\mathbf{r}_{ik}}{|\mathbf{r}_{ik}|^2}\right\}_z\right]^2 . \tag{4.13}$$

In this model, The bending of nearest neighbor bonds are considered.

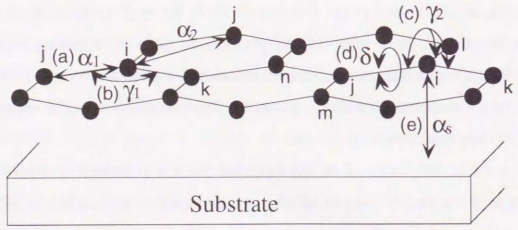

Fig. 4.27 Schematic view of the defined force constants within the graphite lattice.

(iii) Out-of-plane bending terms

For the out-of-plane bond bending, the FC γ_2 corresponds. This is the force to keep flat three nearest neighbor bonds connected to one carbon atom. When three atom j, k, and l are the nearest neighbors of atom i as shown in Fig. 4.27 (c), the potential term becomes:

$$\frac{\gamma_2}{2}\left\{\frac{u_{jz}+u_{kz}+u_{lz}-3u_{iz}}{|\mathbf{r}|}\right\}^2 , \tag{4.14}$$

where $|\mathbf{r}|$ is the nearest neighbor distance: $a/\sqrt{3}$.

(iv) Twisting terms

The potential terms for twisting of the nearest-neighbor bond i–j in Fig. 4.27 (d) is expressed as follows:

$$\frac{\delta}{2}\left\{\frac{(u_{kz}-u_{lz})-(u_{mz}-u_{nz})}{a}\right\}^2 . \tag{4.15}$$

Atoms k and l are the nearest neighbors of atom i. Atoms m and n are those of atom j. Concrete expressions are given in Appendix A.1.

(v) Interaction to the substrate

The stretching FC α_s shown in Fig. 4.27 (e) is taken into account as the interaction to the substrate. This FC works only in the z direction. Because the graphite sheet itself has very strong bonds along the x-y plane, the parallel components of the interaction to the substrate should affect only long-wavelength region of the LA mode to a small extent. Such a low energy part in the long wave-length region was not acquired in the HR-EELS experiment. Moreover, it is very difficult to consider precisely the parallel force in the incommensurate structure. Therefore, the parallel components are neglected in this model, the expression becoming:

$$\frac{\alpha_s}{2}u_{iz}^2 . \tag{4.16}$$

4.3.3. Fitting of the phonon dispersion curves to the experimental results

Once the potential terms are defined, phonon energy (frequency) is calculated as eigen values of the dynamical matrix (4.11) at any wave vector $\mathbf{k}_{||}$. The explicit expressions of the dynamical matrix are given in

Appendix A.2. When the wave vector lies on highly symmetric axis like $\bar{\Gamma}$–$\bar{M}$ and $\bar{\Gamma}$–$\bar{K}$–$\bar{M}$, the eigen value can be calculated analytically as shown in Appendix A.3 and A.4.

The calculated phonon dispersion curves of SH modes (A.52), L modes (A.55) and Z modes (A.58) for the $\bar{\Gamma}$–$\bar{M}$ direction are fitted to the experimental data by the least squares method. For the data of monolayer graphite on WC(0001), the phonon dispersion along $\bar{\Gamma}$–$\bar{K}$ (Appendix A.4) are also taken into account.

In my model, the Z modes are completely isolated from the others. The sum of squares for the Z modes is:

$$S_Z = \sum_{i}^{\substack{\text{all measured} \\ \text{Z mode peaks}}} \left\{ \frac{\hbar\omega_Z(\gamma_2, \delta, \alpha_s; k_i) - E_i}{\Delta E_i} \right\}^2 , \qquad (4.17)$$

where E_i is the loss energy, ΔE_i is the estimated experimental error, k_i is the wave number calculated by (4.2). In order to get the best fit, the minimum point of S_Z is searched by varying γ_2, δ and α_s. The minimizing calculations were done on a personal computer (Apple Computer Inc., Macintosh SE/30) by using the application software ('Wolfram Research Inc., Mathematica ver. 1.2).

In the cases when the phonon is not softened [C/TaC(001), C/NbC(001), C/WC(0001), C/WC(10$\bar{1}$0) (u), and C/Pt(111)], α_s is assumed to be zero from the beginning. In these cases, the ZA mode seems to start at zero energy at $\bar{\Gamma}$ because α_s is so small as in the pristine graphite. In such a low energy region, the assumption that the substrate does not move is not the case. So it is meaningless to estimate α_s as a fitting parameter in this model. As α_s must be very small, the other fitting parameters (γ_2 and δ) are scarcely affected by neglecting α_s. In the case of C/WC(10$\bar{1}$0) (s), the ZA mode is mixed with the substrate branch around $k_{\parallel} \sim 1$ Å^{-1}. In the fitting procedure, the lower branch in $k_{\parallel} < 0.7$ Å^{-1} and

the higher branch in $k_{\parallel} > 1.1$ Å^{-1} are used as data points for the ZA mode.

The SH modes and the L modes are governed by the same set of parameters (α_1, α_2 and γ_1). The sum of squares are:

$$S_{XY} = \sum_{i}^{\substack{\text{all measured} \\ \text{SH mode peaks}}} \left\{ \frac{\hbar\omega_{SH}(\alpha_1, \alpha_2, \gamma_1; k_i) - E_i}{\Delta E_i} \right\}^2 + \sum_{i}^{\substack{\text{all measured} \\ \text{L mode peaks}}} \left\{ \frac{\hbar\omega_L(\alpha_1, \alpha_2, \gamma_1; k_i) - E_i}{\Delta E_i} \right\}^2 . \qquad (4.18)$$

Table 4.1 lists thus fitted FC parameters. The dispersion curves calculated by using the fitted parameters are shown by the solid curves in the dispersion relations from Fig. 4.5 to Fig. 4.26. The agreement seems quite well as a whole. When graphite layer is not softened, fitness of the model is not perfect especially in the LO and ZO modes. For example, in the cases of C/Pt(111), C/NbC(001) and bulk graphite shown in Fig. 4.11 and 4.26, the calculated curve of the LO mode monotonically decreases in energy, although the measured data increases with the wave number and has a maximum around 0.4–0.6 Å^{-1}. Small discrepancy is seen also in the ZO mode in these cases. These discrepancies are caused by the limitation of the model. Probably long-range interactions cannot be neglected in these cases. Inversely saying, excellent agreements of the model with the experimental data in the softened monolayer graphite indicate reduction of such long-range interactions. Some screening mechanism of the long-range interaction may exist in the monolayer graphite having the softened phonon structure.

In the FC's, γ_2 is largely reduced on TaC(111), NbC(111), HfC(111), TiC(111), WC(10$\bar{1}$0) and Ni(111) by 40–55 % compared with the pristine graphite, but is not so changed on TaC(001), NbC(001), WC(0001) or Pt(111). This variety corresponds to the phonon softening on the ZO mode. The in-plane FC's α_1 and γ_1 decrease a little in the former group

Table 4.1 Fitted force constants of monolayer graphite. Numbers in parentheses are deviation from pristine graphite.

Substrate	α_1 [10^5 dyn/cm] ($\Delta\alpha_1$ [%])	α_2 [10^4 dyn/cm] ($\Delta\alpha_2$ [%])	γ_1 [10^{-12} erg] ($\Delta\gamma_1$ [%])	γ_2 [10^{-12} erg] ($\Delta\gamma_2$ [%])	δ [10^{-12} erg] ($\Delta\delta$ [%])	α_s [10^4 dyn/cm]
Pristine graphite	3.64	6.19	8.30	3.38	3.17	0.29[a]
TaC(111)	3.28 (-10)	4.88 (-21)	7.18 (-13)	1.52 (-55)	1.16 (-64)	5.3
HfC(111)	3.46 (-5)	5.20 (-16)	6.49 (-22)	1.61 (-52)	1.74 (-45)	5.7
NbC(111)	3.39 (-7)	4.96 (-20)	6.66 (-20)	1.68 (-50)	1.89 (-40)	4.9
TiC(111)	3.46 (-5)	4.23 (-32)	7.49 (-10)	1.71 (-50)	1.44 (-55)	6.2
TaC(001)	3.63 (±0)	5.04 (-19)	8.53 (+3)	3.21 (-5)	1.98 (-38)	0[b]
NbC(001)	3.94 (+8)	5.59 (-10)	8.20 (-1)	3.23 (-5)	2.16 (-32)	0[b]
WC(0001)	3.36 (-8)	5.41 (-13)	8.70 (+5)	3.16 (-7)	2.75 (-13)	0[b]
WC(10$\bar{1}$0) (s)	3.44 (-5)	5.35 (-14)	6.87 (-17)	1.60 (-53)	1.93 (-39)	4.3
WC(10$\bar{1}$0) (u)	3.59 (-1)	5.09 (-18)	9.61 (+16)	3.15 (-7)	3.14 (-1)	0[b]
Ni(111)	3.24 (-11)	4.72 (-24)	7.75 (-7)	2.08 (-38)	1.45 (-54)	1.4
Pt(111)	3.94 (+8)	5.37 (-13)	8.33 (±0)	3.21 (-5)	1.90 (-40)	0[b]

[a]This value is the inter-layer force constant determined from the neutron data.
[b]These values are not fittted parameters but assumed to be zero at first.

according to the softening of the LO mode, but the softening quantity (–5 – –20 %) is much smaller than the out-of-plane bending FC γ_2. Additionally in the softened group, the FC α_s between the graphite layer and the substrate is 15–20 times greater than the interlayer FC in the bulk graphite. This corresponds to the hardening of the ZA mode in the long wavelength region. The long range FC δ tends to decrease by 30–60 % regardless of the substrate. The similar reduction is seen in α_2 although the deviation is smaller. The reduction of the long range FC's is probably a feature of the monolayer structure itself.

4.3.4. Slab model for the commensurate monolayer graphite on Ni(111)

In the above analysis, the atomic structure of the substrate is not considered because it is too difficult to make a concrete model in the incommensurate structure. This approximation is appropriate when the substrate atom is so heavy that the phonon band is completely separated from the graphite mode in energy. When the substrate atom is lighter, low energy part of the graphite modes (especially ZA mode) must interact with the substrate band to make so called "resonance modes". As the resonance mode is fairly localized in the graphite sheet, the approximation might work well even in such a case. But it indeed remains controversial how graphite modes interact with the substrate and how much the localization is. Fortunately, monolayer graphite makes commensurate structure on Ni(111), and therefore, its atomic structure has already been established; Carbon atoms occupy all three-fold hollow sites at the height of 2.8 Å from the first layer Ni.[11] In this section, the interaction of the ZA mode with the substrate band is studied by using a slab model.

The slab consists of one graphite layer and 30 Ni layers. In addition five intralayer FC's defined above (α_1, α_2, γ_1, γ_2, and δ), a stretching FC

between C and Ni ($\alpha_{C\text{-}Ni}$) and a stretching FC between Ni atoms within the substrate (α_{Ni}) are adopted. In accordance with usual procedure of dynamical calculation,[60] the dynamical matrix of the slab configuration has been made (Appendix B) and diagonalized by a main-frame computer (FACOM M-360). The intra-layer FC's are fixed at those values in Table 4.1, and α_{Ni} is assumed to be 3.79×10^4 [dyn/cm] according to the literature.[63] As one C atom has three nearest neighbor Ni atoms and the C–Ni bond is tilted, three times of the vertical component of $\alpha_{C\text{-}Ni}$ might correspond to the α_s in the previous model:

$$\alpha_s \leftrightarrow 3 \cdot \frac{2.8}{\sqrt{2.8^2 + 2.49^2/3}} \alpha_{C\text{-}Ni} = 2.67\ \alpha_{C\text{-}Ni} \qquad (4.19)$$

At first, let me calculate using this value estimated from (4.19); $\alpha_{C\text{-}Ni} = 5.2 \times 10^3$ dyn/cm.

The resultant dispersion curve is shown in Fig. 4.28. The mode in which the localization in the graphite layer exceeds 0.3 is shown by the thick curves. Below 0.9 $Å^{-1}$, the ZA mode disappears by the mixing with the bulk band. That is, the localization does not exceed 0.3 in any one mode in this region. But in the bulk band, many mode exists in narrow energy range. In the resonance mode, some these modes share the vibrational amplitude in the graphite layer. Even if there is not any highly localized mode, the density of state in the graphite layer is not negligible in such a case. Therefore, the local density of states (LDOS) of the z-displaced vibration: ρ_{zz}, which is defined as $\rho_{zz}(E) = \Sigma\ (v_{C_1z}{}^2 + v_{C_2z}{}^2)\ \delta(E\text{-}\hbar\omega)$ is calculated. Here, δ function is replaced by Lorenzian of 0.8 meV width in order to simulate the finite linewidth of the phonon. The resultant LDOS in the graphite layer is shown in Fig. 4.29 (a). The LDOS in the second layer Ni is also calculated and shown in Fig. 4.29 (b). In the bulk band below 35 meV, the ZA mode is recognized apparently although the linewidth is fairly broadened. The dispersion relation of this resonance mode well

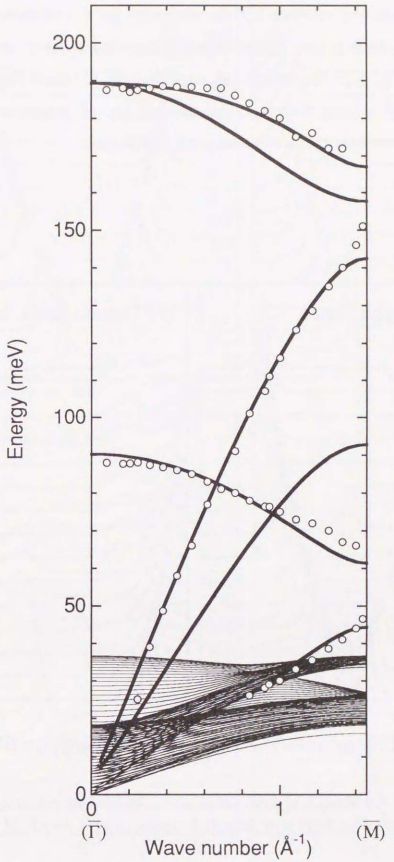

Fig. 4.28 Phonon band of graphite-covered Ni(111) calculated by the slab model. The localized mode is indicated by the thick lines. The experimental data is plotted by the open circles.

corresponds with that calculated in the simple model (solid curves in Fig. 4.24). Indeed, there is less density at that energy in the substrate Ni layer as shown in Fig. 4.29 (b), which indicates that the substrate little moves with the graphite and therefore the assumption of structureless and infinitely-massive substrate well stands even in this case.

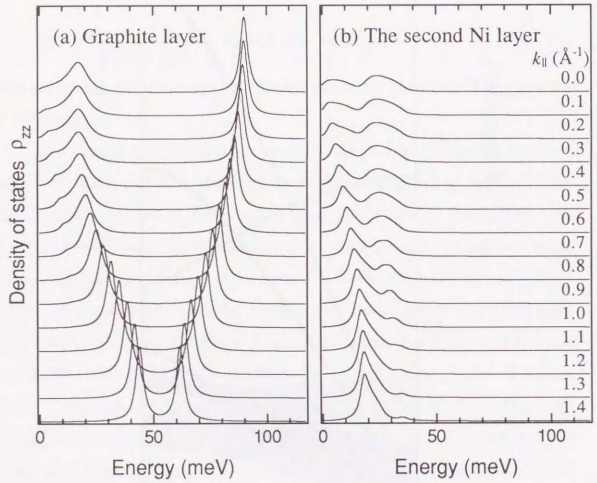

Fig. 4.29 Calculated local density of states of z-displaced phonon (a) in the graphite overlayer and (b) in the Ni layer below it. The wave vector is along Γ–M axis.

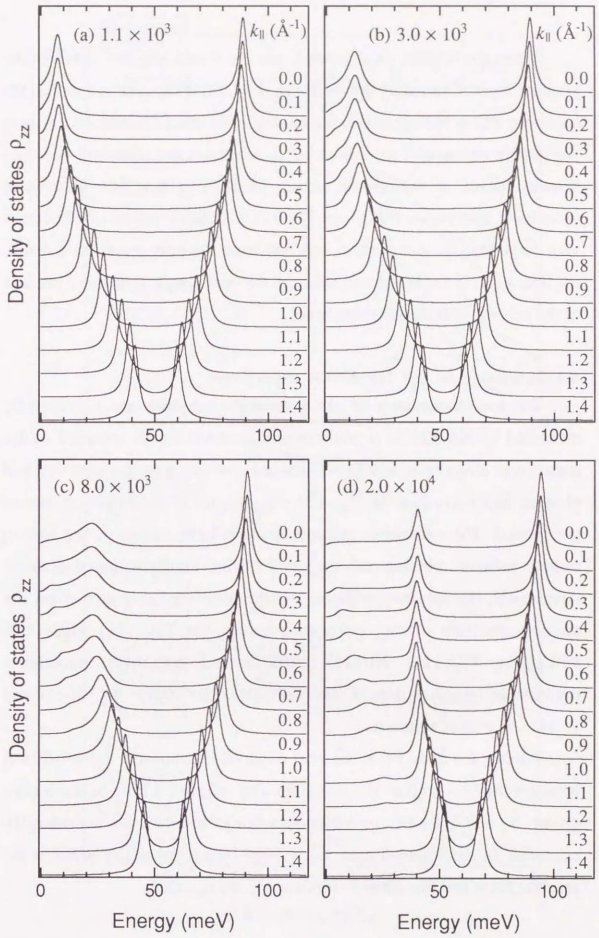

Fig. 4.30 Calculated local density of states in the graphite layer. The interaction between Ni and C ($\alpha_{C\text{-}Ni}$) is indicated in [dyn/cm].

When the interaction between C and Ni is changed, the LDOS in the graphite layer is varied as shown in Fig. 4.30; (a) If $\alpha_{C\text{-}Ni}$ is as small as the interlayer FC in bulk graphite, the mixing is so small that the ZA mode is not largely broadened. (b)–(c) As $\alpha_{C\text{-}Ni}$ increases, the linewidth becomes broader because of the phonon mixing. (d) If $\alpha_{C\text{-}Ni}$ is as large as those in monolayer graphite on NaCl-type TMC(111) surfaces, the mixing becomes very large and the ZA mode is repelled from the bulk band. As a result, the line width is not broadened although the peak height is reduced because of the mixing with the substrate band.

4.4 Summary of the HR-EELS experiment

Phonon dispersions of the monolayer graphite are successfully measured by HR-EELS. A phenomenological FC model specified to the monolayer graphite is newly constructed and fitted to the experimental phonon dispersion data. In Fig. 4.31 the varieties of the fitted parameters are plotted. The monolayer graphite is classifiable into two: one having largely softened phonon and the other having hardly softened phonon. Apparently, the substrate material and the interfacial structure affect the phonon structure of the overlayer graphite; On TaC(111), HfC(111), NbC(111), TiC(111), Ni(111), Ni(001), and WC($10\bar{1}0$), monolayer graphite is largely softened. On TaC(001), NbC(001), WC(0001) and Pt(111), it is little softened.

Among the fitted FC's, the most remarkable contrast is exhibited in γ_2 between the two groups. α_1 and γ_1 are also softened a little in the former group. α_2 and δ tend to be softened although the data are considerably scattered. In the softened case, fairly large interaction exists between the graphite layer and the substrate as shown in the α_s value.

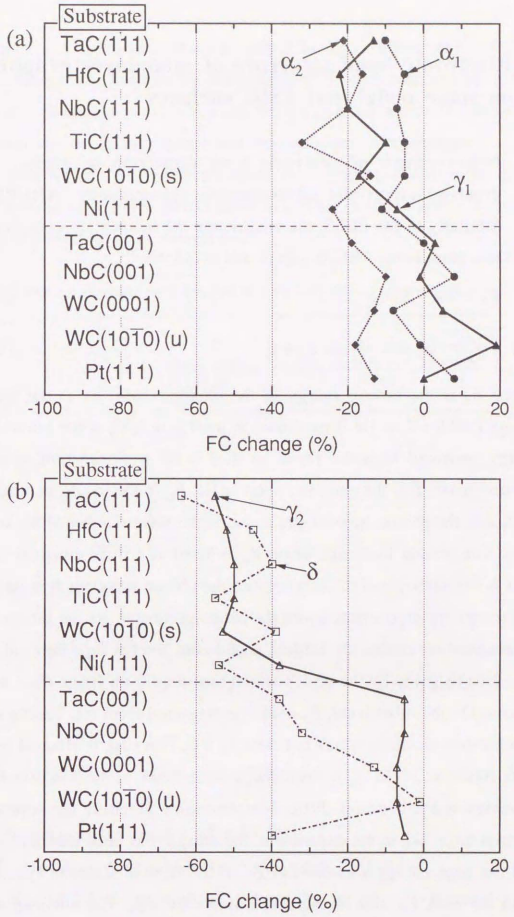

Fig. 4.31 Fitted force constant change from bulk graphite. (a) FC parallel to the plane, and (b) FC perpendicular to the plane.

5. Electronic band structure of monolayer graphite on some metal and TMC surfaces

5.1. Measurements of electronic band dispersion by angle-resolved ultraviolet photoelectron spectroscopy (ARUPS)

Similarly to the EELS, the energy and the momentum conservation law takes place in the ARUPS experiment as follows:[64]

$$E_k = h\nu + E_i - \phi \tag{5.1}$$

and $$\frac{\sqrt{2mE_k}}{\hbar} \sin\theta = \frac{2\pi}{\lambda} \sin\theta_{in} + k_i \quad , \tag{5.2}$$

where E_k is the kinetic energy of the photoelectron, $h\nu$ is the photon energy (40.8 eV of He II excitation is used here), E_i is the initial state energy measured from the Fermi level, ϕ is the work function, m is the electron mass, θ is the emission polar angle, θ_{in} is the incidence angle of light, λ is the photon wavelength, and k_i is the wave number of the initial state. The photon incidence angle θ_{in} is fixed at 45°. In equation (5.2), $2\pi/\lambda$ is negligible (~ 0.02 $Å^{-1}$) because the photon wavelength is large in this energy region compared with the lattice parameter. As the sample and the analyzer are commonly earthed, each Fermi level is kept identical, and E_i is directly given by the peak position measured from Fermi edge in the spectra. On the other hand, E_k could be measured from the leading edge of secondary electrons which indicates $E_k = 0$. This edge is affected by the work function. When E_k is very low, transmittance of the analyzer fairly decreases and it becomes difficult to determine precisely the secondary electron edge. So, in the experiment, the sample was once biased at –8 V and the edge energy was determined in the normal emission spectrum. Then the work function is calculated as $\phi = h\nu + E_i$. The obtained work function values are listed in Table 5.1. E_k, which is necessary to get wave vector k_i, is calculated from E_i and ϕ in the subsequent ARUPS measurement. The energies for the secondary electron edge and the Fermi edge are estimated at 0.2 eV away from the point where the intensity begins to rise up, taking into account the resolution of the analyzer.

Now we can get two-dimensional electronic band dispersion $E_i(k_i)$ from a series of ARUPS spectra taken in various emission angles θ. In this study, θ is changed at an interval of 2°.

Table 5.1 Measured work function of clean and graphite-covered surfaces.

	Φ clean surface [eV]	Φ graphite-covered surface [eV]
TaC(111)	4.7	3.5
HfC(111)	4.9	3.7
TaC(001)	4.3	3.9
HfC(001)	4.5	4.3
WC(10$\bar{1}$0)	4.8	4.2
Ni(111)	5.4	4.2
Pt(111)		4.5

5.2. Experimental results of ARUPS

5.2.1. Monolayer graphite on NaCl-type TMC(111)

Figures 5.1 shows series of the spectra for monolayer graphite on HfC(111) measured along the azimuths of [1$\bar{1}$0] and [11$\bar{2}$] of the substrate,

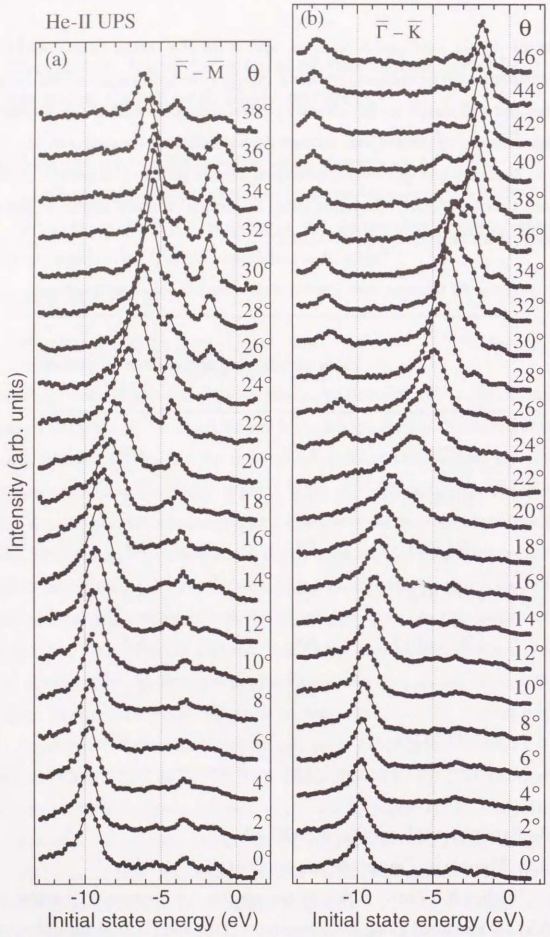

Fig. 5.1 ARUPS spectra of monolayer graphite on HfC(111) along (a) <1$\bar{1}$0> and (b) <11$\bar{2}$> of the substrate.

which are $\bar{\Gamma}$–$\bar{M}$ and $\bar{\Gamma}$–$\bar{K}$ directions for the dominant part in the overlayer graphite, respectively. In the normal emission spectrum, two peaks are clearly recognized at –9.8 eV and –3.5 eV. These peaks shift with the emission angle θ. The dispersion relations are shown in Fig. 5.2. The band located at –9.8 eV on the $\bar{\Gamma}$ point has parabolic dispersion. This band is a π band of the monolayer graphite. It is worth noting that the energy of the π band (-9.8 eV) is lower than that of pristine graphite (–6.8– -8.9 eV).

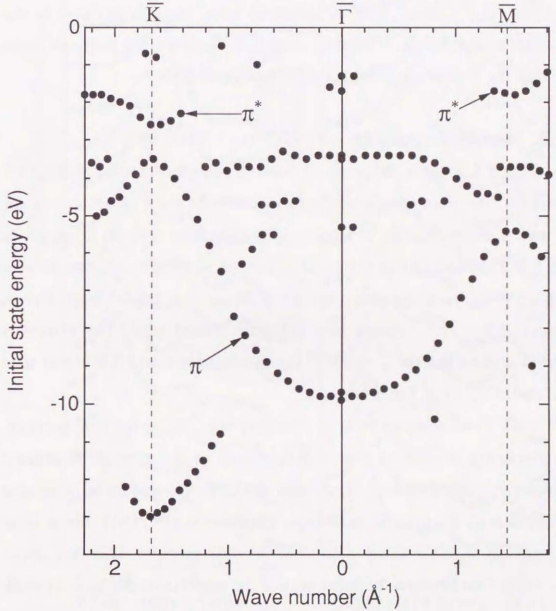

Fig. 5.2 Electronic band dispersion of graphite covered HfC(111).

The band near –3.5 eV is almost dispersionless and may be a substrate-related band. Near the $\overline{K}$ and $\overline{M}$ points, we can see the antibonding π^* band apparently. In the low energy region, the σ band appears around the $\overline{K}$ point.

The monolayer graphite on TaC(111) shows similar results (Figs. 5.3 and 5.4). In this case, however, the peaks are not well resolved in the edge region of SBZ because of the two-domain structure. The π band of the monolayer graphite is also located at –10 eV at the $\overline{\Gamma}$ point. On this surface, almost dispersion-less modes appear around –0.5 eV and –5.5 eV. At about –2 – –2.5 eV, a weak feature is seen. These bands may be the substrate related bands. It must be noted that some mixing seems to occur between the π band and the substrate's band of –5.5 eV.

5.2.2. Monolayer graphite on NaCl-type TMC(001)

Figure 5.5 shows the series of ARUPS spectra measured along [$1\bar{1}0$] of the HfC(001) substrate, which corresponds $\overline{\Gamma}$–$\overline{M}$ and $\overline{\Gamma}$–$\overline{K}$ directions for the two domain graphite overlayer. The dispersion relation is shown in Fig. 5.6. The band having parabolic dispersion is π band of the monolayer graphite. Two bands appearing below –9 eV are its σ bands. Weak feature around –1.5 – –2.5 eV may be a substrate related band. The π band is located at -8.8 eV at the $\overline{\Gamma}$ point. This value is more than 1 eV higher than that on HfC(111) or TaC(111).

Here let us compare with pristine graphite.[65-68] In the bulk graphite, the interlayer interaction causes the splitting of the π band. If isolated monolayer graphite existed, its π band should be the middle of these split bands. But in the case of monolayer graphite on HfC(001), the π band corresponds with the lower π band of the bulk graphite. This fact shows that interaction between the substrate and the graphite overlayer is as weak

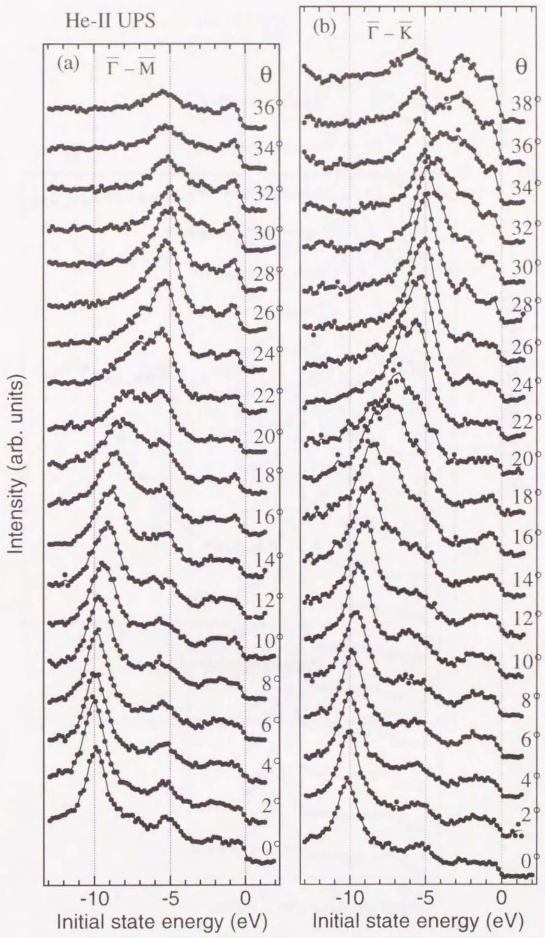

Fig. 5.3 ARUPS spectra of monolayer graphite on TaC(111) along (a) <1$\bar{1}$0> and (b) <11$\bar{2}$> of the substrate.

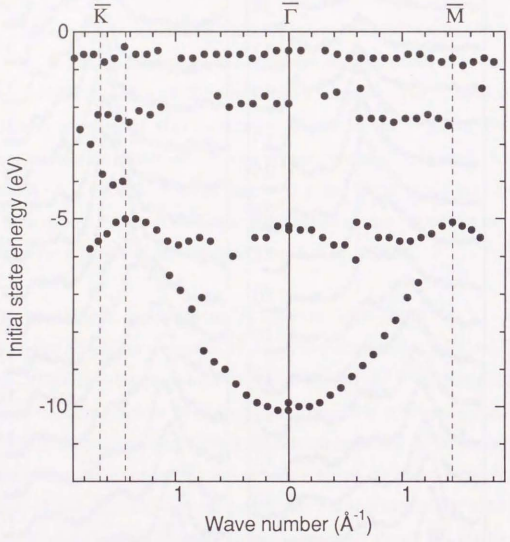

Fig. 5.4 Electronic band dispersion of graphite covered TaC(111).

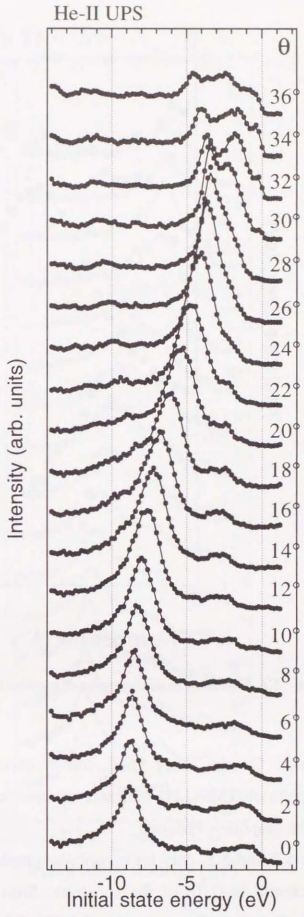

Fig. 5.5 ARUPS spectra of monolayer graphite on HfC(001).

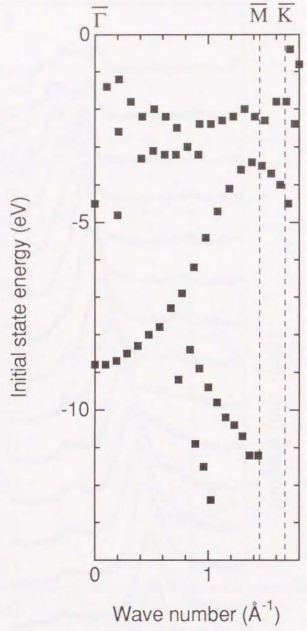

Fig. 5.6 Electronic band dispersion of graphite covered HfC(001).

as bulk graphite. On the other hand, much lower π band energy in monolayer graphite on TMC(111) indicates stronger interaction between the substrate and the graphite overlayer.

In figures 5.7 and 5.8, data for monolayer graphite on TaC(001) are shown. The azimuth is [1$\bar{1}$0] of the substrate. Similarly to the case of HfC(001), the π band has the energy of –8.8 eV at the $\overline{\Gamma}$ point. The band

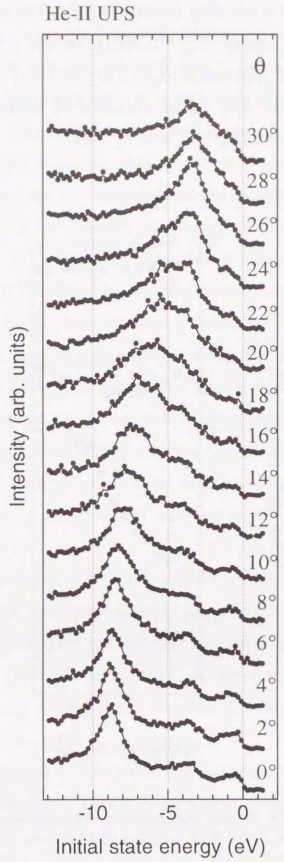

Fig. 5.7 ARUPS spectra of monolayer graphite on TaC(001).

around –3.5 – –4 eV is probably a substrate band. The substrate band has about 1.7 eV lower energy than HfC(001). On the (111) surfaces, the substrate related band appeared at –3.5 eV on HfC(111) and at –5.5 eV on TaC(111). This energy shift can be explained by difference of the total electron number between IV_a-TMC and V_a-TMC.

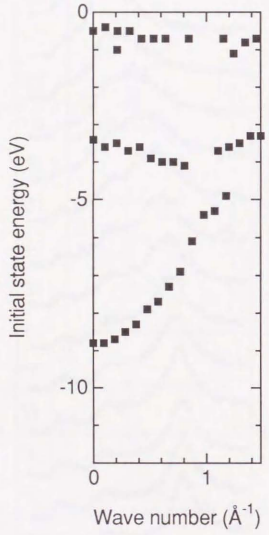

Fig. 5.8 Electron band dispersion of graphite covered TaC(001).

5.2.3. Monolayer graphite on WC(10$\bar{1}$0)

In the phonon structure, the difference occurred with the preparing conditions; When the sample is made at 1300°C or annealed at 1300°C after made at 1500°C, only softened phonon is observed. When the sample is made at 1500°C and is rapidly cooled, two set of phonons (softened and unsoftened modes) are simultaneously observed although the unsoftened mode is very weak. In ARUPS measurement, these two preparation procedures are tried. Figure 5.9 shows the annealed and the quenched samples. Figure 5.10 shows the dispersion relations. Unfortunately, no difference is recognized between the two samples. The unsoftened mode was very weak in the EELS spectra, indicating this area is very small. As UPS spectra have fairly high background, such a weak feature can be lost. Or the cooling rate of the sample in the UPS experiment can be slower than that in the EELS experiment because the sample holder was not the same. When the cooling rate is slow enough, the sample stays around 1200–1300°C for a while, which may cause the same effect of the annealing at 1300°C.

The measurements were done along the direction 15° away from [0001] azimuth. In this case, the graphite overlayer forms four domain structure. Two are stronger and the other two are weaker. Here one of the strong domain is chosen to be aligned $\bar{\Gamma}$–$\bar{M}$ direction in the measurement and the other strong domain $\bar{\Gamma}$–$\bar{K}$. The peak feature therefore spreads in the edge region of the SBZ.

The band located at –10 eV at the $\bar{\Gamma}$ point is the π band of the monolayer graphite. Bands seen at –7 eV and at –2 eV are substrate-related bands. The former one looks to interact with the π band and to be mixed with it around 1 Å^{-1}. The band in –4 – –5 eV near the $\bar{\Gamma}$ point may be the σ band of the monolayer graphite or may be another substrate's band. The

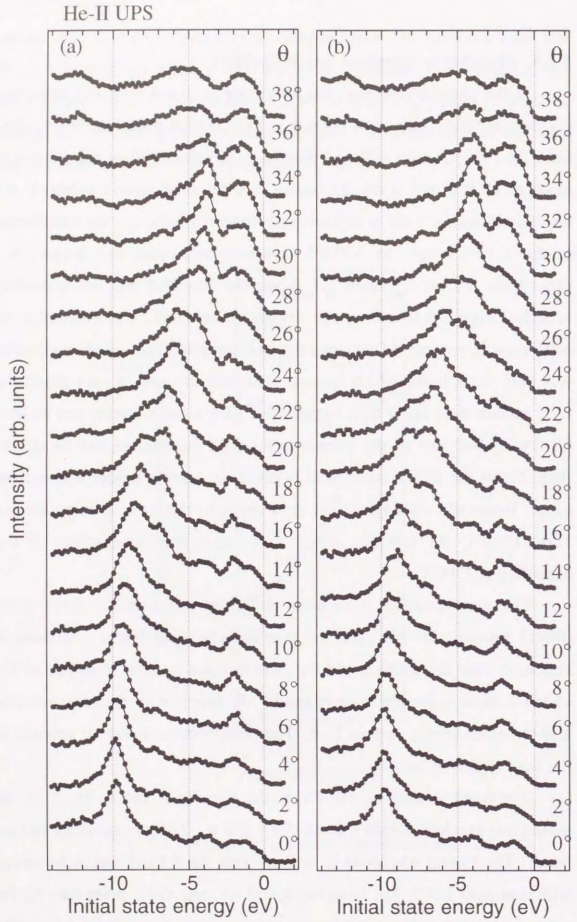

Fig. 5.9 ARUPS spectra of monolayer graphite on WC(10$\bar{1}$0). The samples are (a) annealed at 1300°C and (b) quenched from 1500°C.

π band energy is similar to that of monolayer graphite on TMC(111), which is common in the graphite layer having the softened phonon structure.

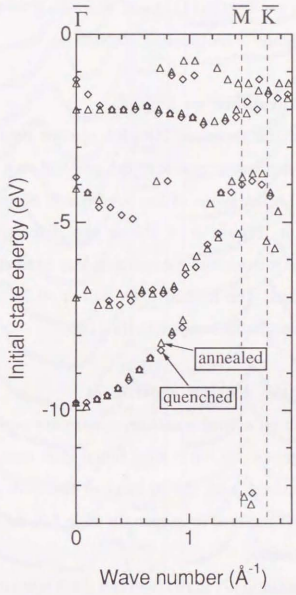

Fig. 5.10 Electronic band dispersion of graphite covered WC(10$\bar{1}$0).

5.2.4. Monolayer graphite on Ni(111)

In Fig. 5.11, ARUPS spectra measured along [11$\bar{2}$] and [1$\bar{1}$0] are shown. The dispersion relations are presented in Fig. 5.12. The π band of the monolayer graphite and a part of the σ band are seen. Bands located at –1 eV and at –2 eV are Ni d-bands, although around the edge region of the SBZ they may be mixed with the antibonding π^* band of the overlayer graphite. The π band energy (–10.1 eV at the $\bar{\Gamma}$ point) is similar to that of monolayer graphite on TMC(111). Such deepening of π band has been reported in the literature[14] for graphite on Ni(001).

5.2.5. Monolayer graphite on Pt(111)

Figure 5.13 is the series of ARUPS spectra measured along the direction toward which one segment of the graphite ring exists in LEED, i.e. one of preferred orientations of the overlayer is aligned $\bar{\Gamma}$–$\bar{M}$ azimuth in the measurement. Figure 5.14 shows the dispersion relations. A parabolic band is the π band, and a dispersion-less band at –0.5 eV may be the substrate's d-band. The π band is located at –8.2 eV at the $\bar{\Gamma}$ point, which is the shallowest in the samples studied here.

5.3. Summary of the ARUPS experiment

In Fig. 5.15, three normal emission spectra are compared with each other. It is unambiguous that the π band initial state energy is different in each sample. Compared with the π band of the bulk graphite, that of monolayer graphite is inclined to deepen. In table 5.2, the π band energy at the $\bar{\Gamma}$ point is summarized.

Here, clear correlation is found between the π band deepening and the phonon softening. In the literature, similar π band shifts are reported for graphite layer on Ni(100),[14] Ni(111),[10,13] Ni(110)[15] and Ru(0001)[19] by

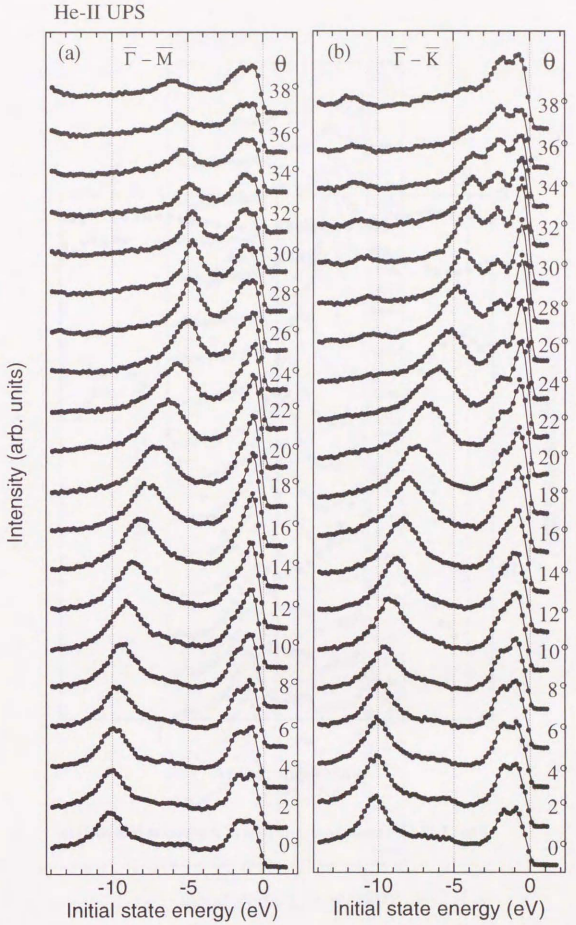

Fig. 5.11 ARUPS spectra of monolayer graphite on Ni(111) along (a) <1$\bar{1}\bar{2}$> and (b) <1$\bar{1}$0> of the substrate.

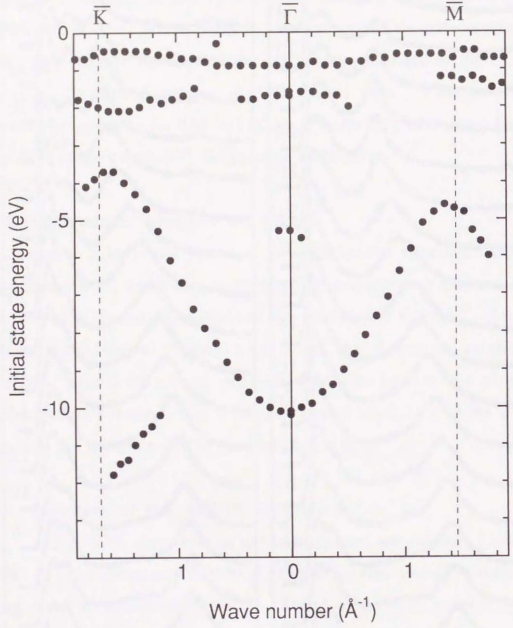

Fig. 5.12 Electronic band dispersion of graphite covered Ni(111).

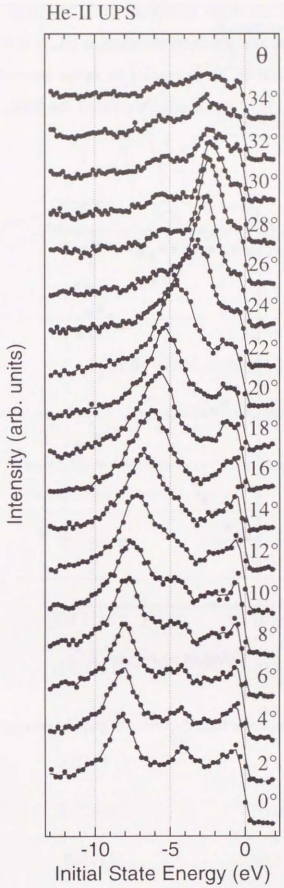

Fig. 5.13 ARUPS spectra of monolayer graphite on Pt(111).

using angle-integrated or angle resolved UPS, although the correlation with another feature has not yet been clarified at all. It is worth noting that antibonding π^* is found to be occupied in some monolayer graphite [C/HfC(111) and C/Ni(111)] in the edge region of the SBZ.

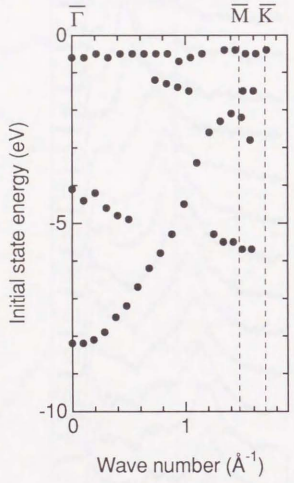

Fig. 5.14 Electronic band dispersion of graphite covered Pt(111).

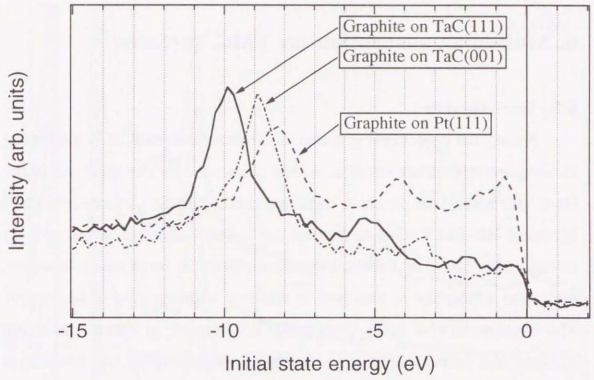

Fig. 5.15 Normal emission UPS for graphite covered TaC(111), TaC(001) and Pt(111).

Table 5.2 Initial state energy of the π band at the $\bar{\Gamma}$ point measured from Fermi level.

Substrate	Initial state energy [eV]
TaC(111)	–10.0
HfC(111)	–9.8
TaC(001)	–8.8
HfC(001)	–8.8
WC($10\bar{1}0$)	–10.0
Ni(111)	–10.1
Pt(111)	–8.2

6. Molecular adsorption on TMC surfaces

6.1. Introduction

Seeing the monolayer graphite as a macro-molecule, it is interesting to compare with other small adsorbed molecules on the same substrate. Here, gas adsorption on some transition-metal-carbide surfaces is studied by using HR-EELS. Gas molecules are usually adsorbed dissociatively (atomic adsorption) at a room temperature (RT). In some cases, however, molecular adsorption is observed in addition with the atomic adsorption. The intra-molecular bond weakening is obtained in these adsorption systems and is compared with the bond weakening in the monolayer graphite.

Waiting for about ten minutes after flash heating to cool the sample to RT, gas was exposed and HR-EELS measurement is done. When the elapsed time after flash heating was so short that the sample temperature was 200 – 300°C, the molecular species was not observed.

6.2. CO, O_2, N_2 and H_2 on NbC(111)

Figure 6.1 shows the EELS spectra of CO exposed NbC(111). The clean surface shows no loss peak. Below 0.5×10^{-4} Pa·s of the CO exposure, two peaks appear at 63 meV and at 74 meV, which can be assigned as atomic C and/or O. Above 1×10^{-4} Pa·s, a new mode grows at 163 meV, which is modified C–O stretching vibration. A large peak around 65 meV is Nb–O vibration for dissociated atoms or Nb–CO vibration of adsorbed CO molecules. Above 10×10^{-4} Pa·s, another molecular peak appears at 243 meV. This CO may adsorb at different site from that for 163 meV. Because no M–C–O bending mode is observed in the specular condition, CO molecule is considered to adsorb

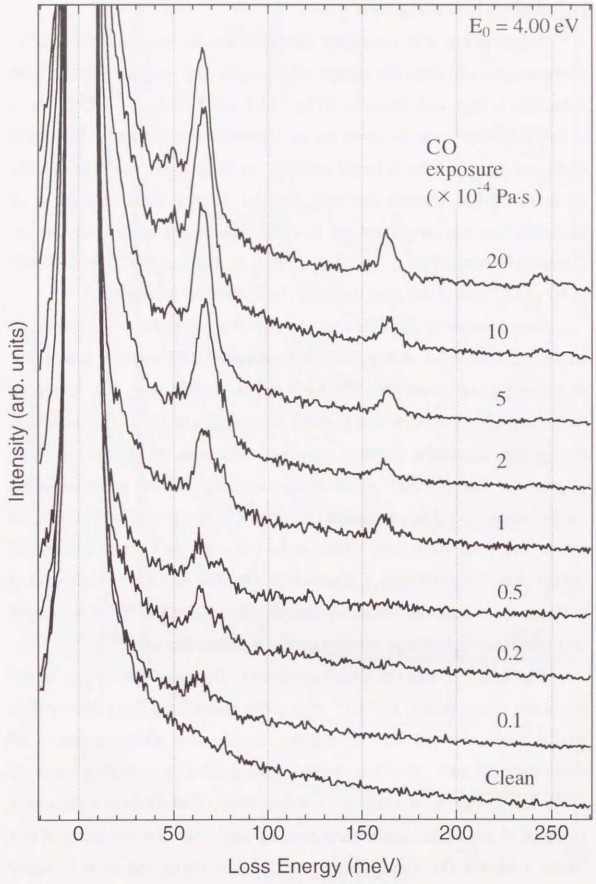

Fig. 6.1 EELS spectra of NbC(111) exposed to CO.

perpendicularly to the surface.

In gas phase, CO stretching vibration has the energy of 266 meV. Comparing with this, the observed energies are very softened. Such softening is common in some CO/metal (Ni,[69-73] Fe,[74,75] Cr,[76] etc.) systems and known as the donation-backdonation mechanism;[77] When CO molecule adsorbed on a metal surface, its highest occupied molecular orbital (HOMO) donates electrons into the metal d band as a result of metal-carbon bonding, and its lowest unoccupied molecular orbital (LUMO) is donated from the metal d band. In the case of CO, the HOMO is 5σ and LUMO is $2\pi^*$, and therefore the C–O bond is weakened.

For example, on Ni surfaces, the stretching frequency is reported to be 247–257 meV for on-top site adsorption, 233–243 meV for adsorption in a bridge site, and 194–226 meV for a hollow site. The observed frequency of 163 meV, which perhaps corresponds to CO in the three-fold hollow site, is much lower than any case on Ni surfaces, showing stronger interaction. The 243 meV mode at high coverage is well assigned to the on-top adsorption. The comparably affected CO is reported on Fe(100), on which the C–O stretching vibration is 141–151 meV in the four-fold hollow site.[75] Additionally, CO molecule adsorbed on alkali-metal-covered surfaces has the similar frequency range (160–180 meV).[78,79] It is thought that relatively high charge transfer occurs on these surfaces.[80]

Figure 6.2 shows the EELS spectra for O_2 dosed NbC(111). In the exposure range below 1×10^{-4} Pa·s, only dissociated O is observed at 61–69 meV. Above 2×10^{-4} Pa·s, two dipole active modes appear at 89 meV and 122 meV. The latter mode is assigned to a stretching mode of O–O. The former mode may be a bending mode of M–O–O or a stretching mode of $M–O_2$. If this mode is the bending mode, the dipole activity of this mode indicates the tilted adsorption. The stretching vibration is fairly softened compared with that of gas phase O_2 (196 meV), similarly to the

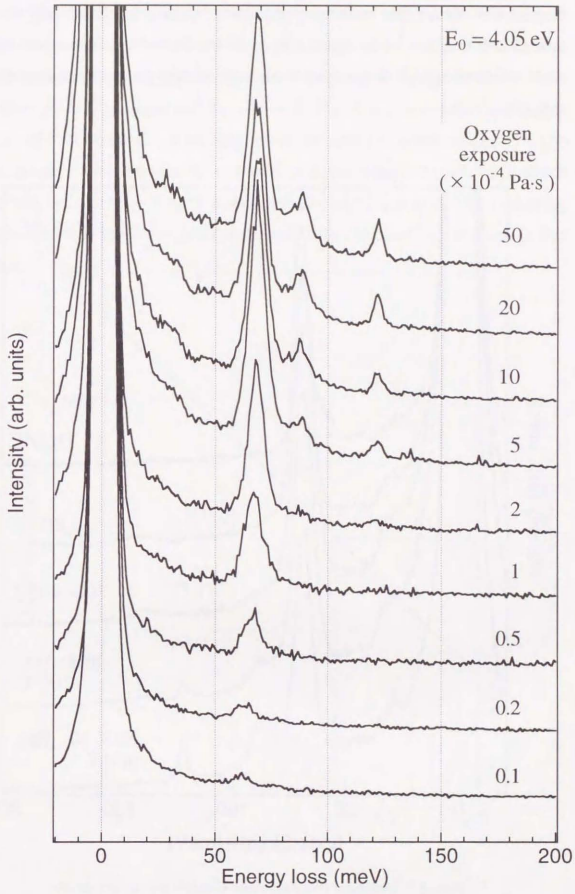

Fig. 6.2 EELS spectra of oxygen exposed NbC(111).

case of CO. When this surface is heated, molecular adsorbate disappears around 300°C as shown in Fig. 6.3. Because the 89 meV mode and the 122 meV mode disappear at the same time, both modes are attributable to the same O_2 species.

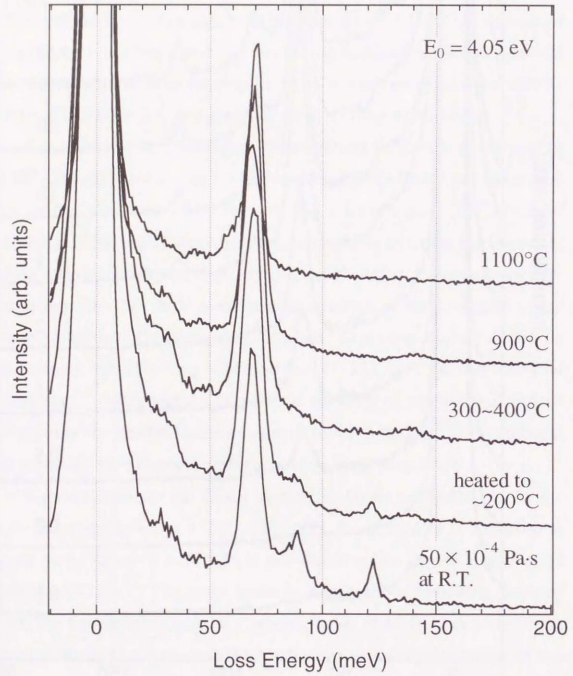

Fig. 6.3 Change of EELS spectrum with heating the sample after oxygen exposure.

The molecular adsorption of oxygen at room temperature is very rare case as long as the author knows. On other metal surfaces, molecular adsorption is reported at low temperature (~ 100 K), where the bond order of O–O is discussed. As shown in Fig. 6.4, linear relationship was reported between the stretching vibration and the bond order.[81-83] The frequency observed here corresponds with the bond order of 1.25, which is between peroxo (O_2^{2-}) and superoxo (O_2^-) species. The softening mechanism is the donation of electrons in the antibonding state also in this case.

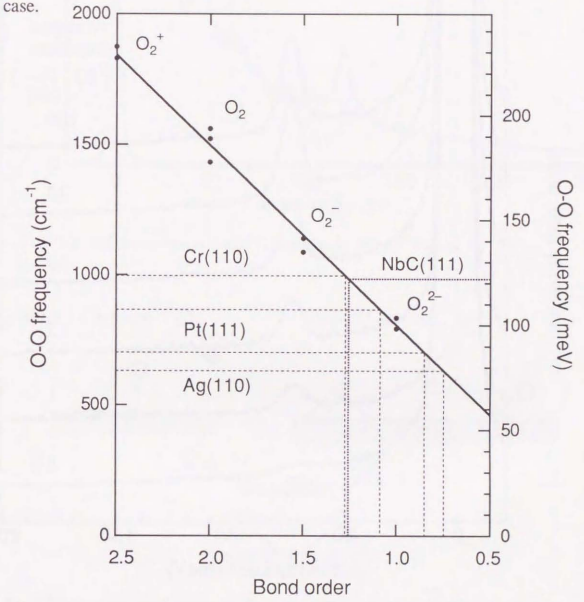

Fig. 6.4 Bond order versus O–O stretching frequency.[84]

Although the molecular species are found in case of O_2 and CO, N_2 and H_2 are clarified to be completely dissociated on NbC(111) at RT. Figures 6.5 and 6.6 show the EELS spectra. When the surface is exposed to N_2, only one peak appears at 73 meV and is saturated at about 30×10^{-4} Pa·s. This is assigned to the atomic adsorbate in the three-fold hollow site. The H saturated surface (exposed to 10×10^{-4} Pa·s of H_2) shows a peak at

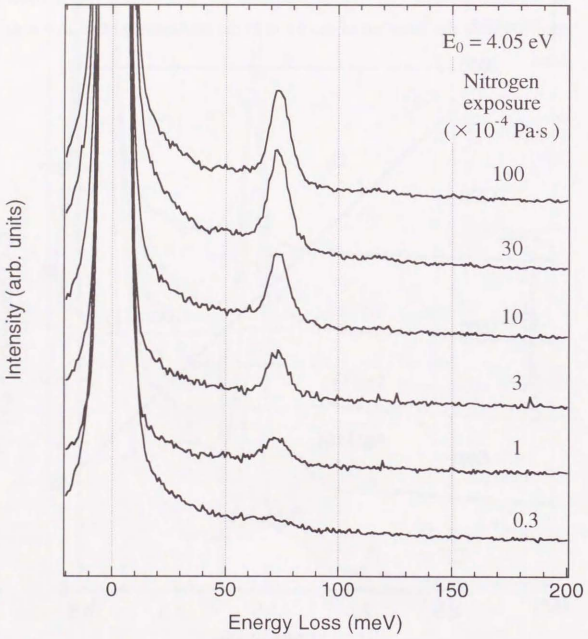

Fig. 6.5 EELS spectra of nitrogen exposed NbC(111).

121 meV corresponding to the hollow-site adsorption. A loss peak around 45 meV may be for carbon impurity.

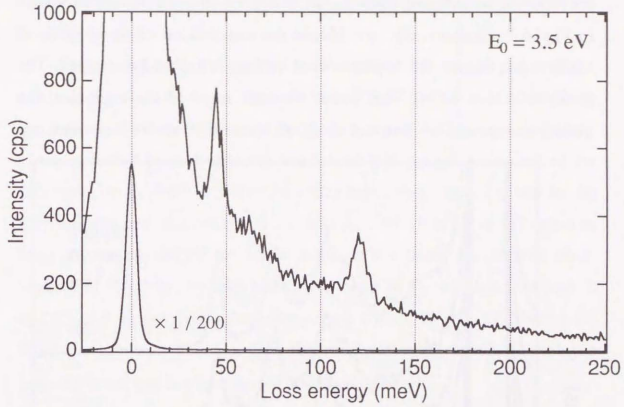

Fig. 6.6 EELS spectrum of NbC(111) exposed to 10×10^{-4} Pa·s of H_2.

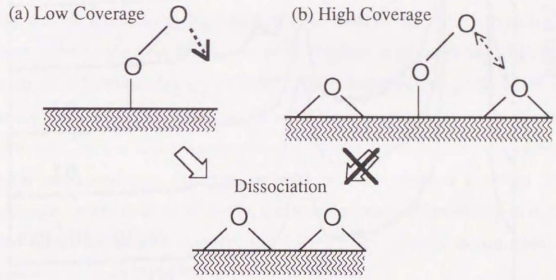

Fig. 6.7 Schematic model of oxygen dissociation and molecular adsorption mechanism.

In the case of CO or O_2 adsorption, the dissociative adsorption occurs prior to the molecular adsorption. Presumably, the atomic adsorbate prevents the neighboring molecule from tipping onto the surface as shown in Fig. 6.7 schematically, and blocks the dissociation of it. In order to confirm this model, the N preadsorbed surface is exposed to oxygen. The result is shown in Fig. 6.8. From the first stage of the exposure, the molecular state can be observed at 120 meV and at 95 meV. The stretching

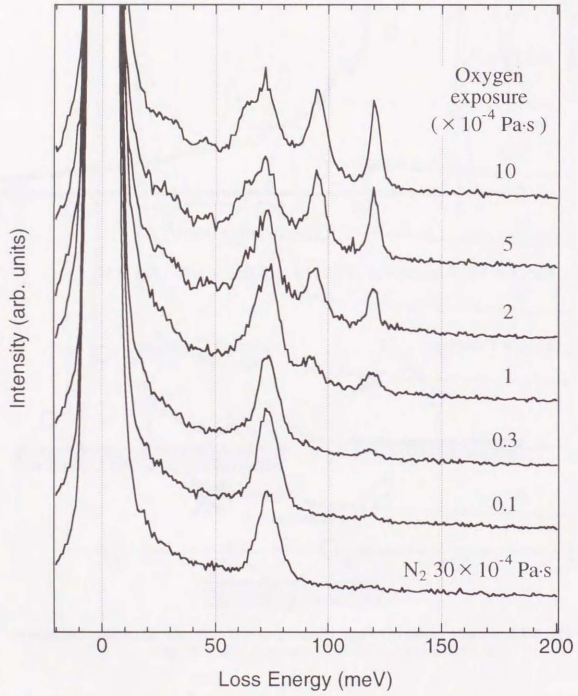

Fig. 6.8 EELS spectral change with exposing oxygen to nitrogen preadsorbed NbC(111).

frequency is a little reduced and the bending frequency is increased. When the molecule is tilted, there may exist some interaction between the upper O and the neighboring N adsorbate, which can cause the difference in the bending frequency.

Comparing with the molecular adsorption, the monolayer graphite seems less softened (from 200 meV to 185 meV). This is attributable to the density of affected bonds on the surface. Even if all three-fold hollow site is occupied by molecule, the bond density is one per a unit cell of the substrate, or 1 / 8.65 $Å^{-2}$. On the other hand, three bonds exists in the graphite unit cell: the density is 3 / 5.50 $Å^{-2}$, which is about 4.7 times as large as the density of molecular bond. If the substrate donates some number of electrons, by which the bond order of O_2 can decrease from 2 to 1.25, that in graphite will decrease only from 1.33 to 1.17. Taking the bond density into account, the observed softening in the monolayer graphite is not smaller than that of adsorbed molecule.

6.3. O_2, N_2 and H_2 on TaC(111)

Similarly to the case of NbC(111), O_2 adsorbs molecularly but N_2 and H_2 adsorb atomically. Figures 6.9 – 6.11 show the EELS results. In contrast with the NbC(111), one peak remains at 60 meV on TaC(111) even after flash-heating up to 2200°C. The origin of this peak is not yet clear. One probable explanation is carbon termination in a domain structure. As ion scattering spectroscopy has not yet detected the carbon-terminated structure, the domain must be very small if it exists. For example, in the case of VC(111), the domain structure consisting of 8×1 for metal terminated surface and $\sqrt{3} \times \sqrt{3}$ for carbon termination is reported by using STM.[84)]

Contrastively with NbC(111), oxygen adsorbs molecularly from the

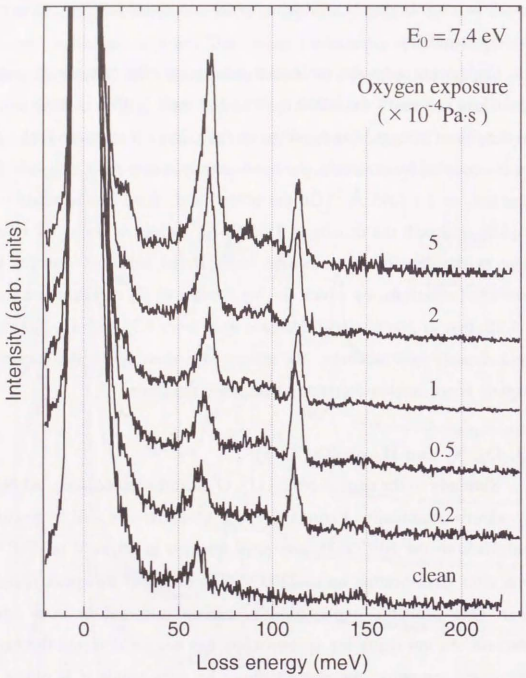

Fig. 6.9 EELS spectra of TaC(111) exposed to oxygen at room temperature.

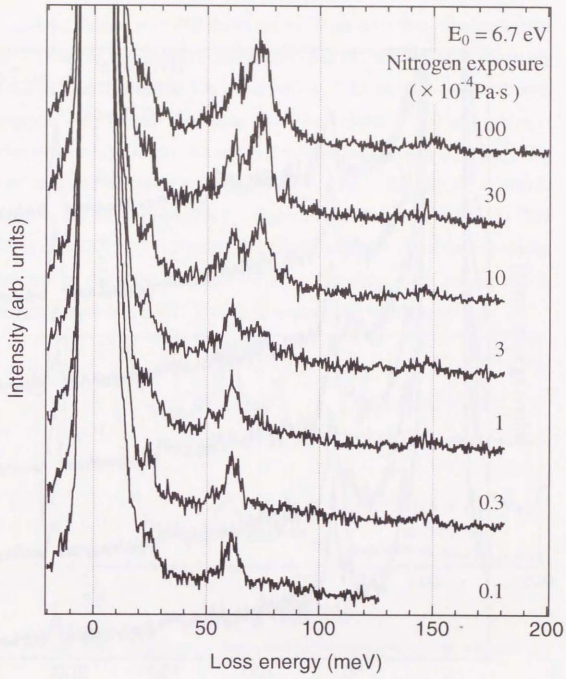

Fig. 6.10 EELS spectra of TaC(111) exposed to nitrogen.

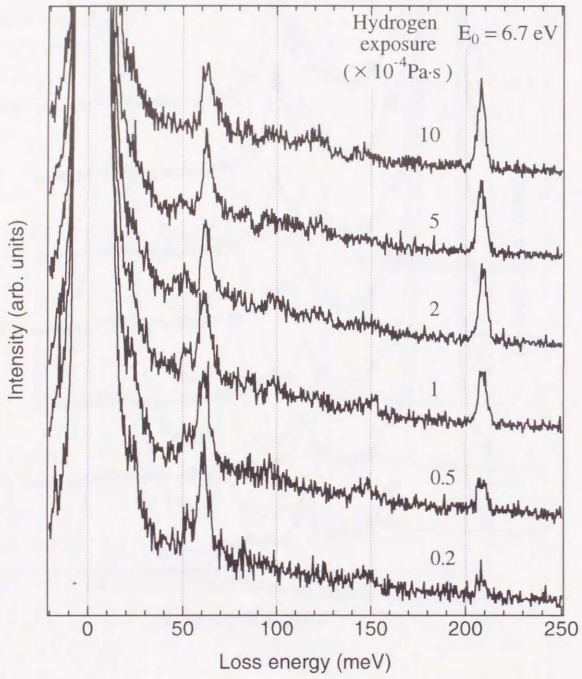

Fig. 6.11 EELS spectra of TaC(111) exposed to hydrogen.

beginning. The molecular state (112 meV) is saturated at about 0.5×10^{-4} Pa·s and the atomic state (65 meV) grows larger after that. The molecular state is changed into another adsorption state (85 meV) under relatively low temperature (~ 300°C) as shown in Fig. 6.12. In the case of nitrogen adsorption, only atomic adsorption state is observed at 75 meV, which is well corresponds to adsorption in the three-fold hollow site. Hydrogen also shows only one vibration state at 208 meV. This is thought to be atomic adsorption but the frequency is too high compared with H/NbC(111) (121 meV) and H/TiC(111) (125 meV)[85] cases in which H atoms are concluded to adsorb in the three-fold hollow site. Probably some interaction is necessary between H and C in order to explain this high frequency.

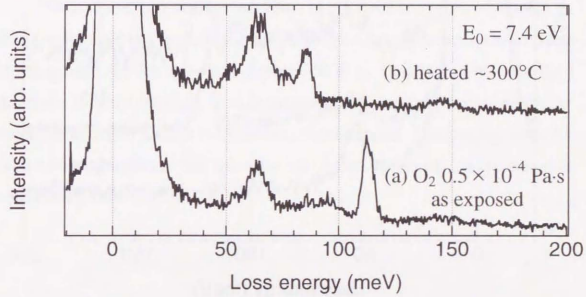

Fig. 6.12 EELS spectral change with mild heating after oxygen exposure.

6.4. O_2 on WC(10$\bar{1}$0)

In this case, molecular species are found at beginning of the adsorption. Figure 6.13 shows the EELS spectra for increased exposure of oxygen. At the beginning, one molecular peak appears at 120 meV and is saturated at 1×10^{-4} Pa·s. Above 2×10^{-4} Pa·s, other peaks appear at 105 meV and at 65 meV. The 120 meV peak shifts to 125 meV as the coverage

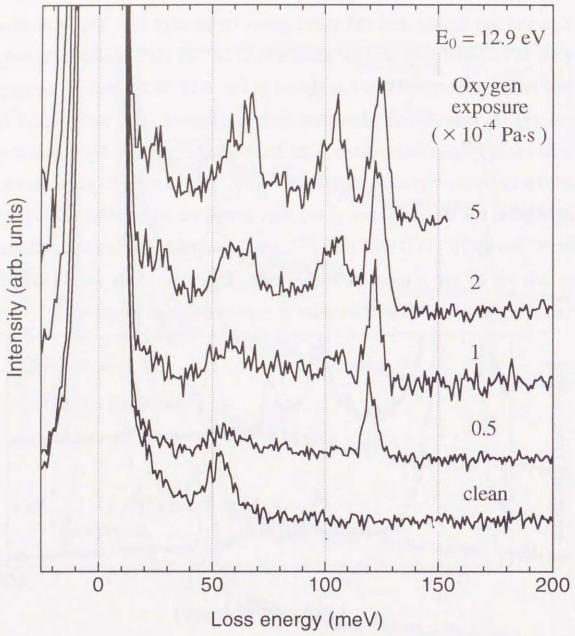

Fig. 6.13 EELS spectra of oxygen exposed WC(10$\bar{1}$0).

is increased, probably because of the dipole-dipole interaction of the adsorbate. Because the substrate has the complex domain structure, which is evident from the mixed LEED pattern (2 × 2 and streak), the two observed adsorption states probably correspond to the different domains. In the 120 meV state, oxygen molecule adsorbs straight to the surface because the bending mode is not observed in the specular EELS, but in the

105 meV state, it might be tilted assuming the 65 meV mode to the bending mode.

In the both adsorption states, the molecular stretching mode is very much softened compared to the gas phase O_2. The higher energy mode is similar to that on NbC(111) corresponding to the bond order of 1.25, while in the lower energy mode, the bond order is estimated at 1.0. Such a low frequency mode was reported in the literature for O_2 molecule adsorbed on Pt(111)[81] or Ag(110)[82] at low temperature. It is surprising that such largely affected oxygen molecule exists at RT on WC(10$\bar{1}$0).

6.5. Summary of the gas adsorption systems

When the clean surface of NbC(111), TaC(111), or WC(10$\bar{1}$0) is exposed to some gas molecule at RT, both atomic and molecular adsorption is recognized. In the molecular adsorption state, bonding in the adsorbed molecule is fairly softened. Such a softening is commonly explained by the electron donation and/or backdonation mechanism. Comparing with the monolayer graphite, the quantity of bond softening is reasonable considering density of the bonds.

7. Discussions

7.1. Phonon softening as the evidence of monolayer

Until now, the reason why graphite overlayers on some metals were concluded to be monolayer has been due to AES intensity and LEED intensity analysis. In this study, I have clarified the phonon softening in the overlayer graphite on some transition-metal carbide surfaces and Ni surfaces. This phonon softening itself proves that the overlayer is monolayer.

In alkaline GIC, "boundary layers": the graphite basal sheets directly touch intercalant are softened, but "interior layers": the other sheets which do not touch intercalant are not so softened and accept indirect effects from the lattice constant change.[86,87] On the analogy of this, the graphite overlayer showing phonon softening must be monolayer. If the overlayer were dilayer or more, not only softened phonon for the layer directly connected to the substrate but also unsoftened phonon for the other layers should be detected by EELS simultaneously. Because the mean-free pass of electrons in EELS is larger than that in LEED in which even the substrate is observed, the electrons can "see" the whole overlayers.

When the overlayer graphite shows the similar phonon structure to pristine graphite as in the case on TMC(001) and Pt(111), the monolayer cannot be confirmed from the phonon structure. But the small deviation in phonon structure, which corresponds to the weakening of the long range FC, strongly suggests the monolayer. Additionally, only one π band appearing in ARUPS indicates the monolayer. Even though the graphite is multilayered, the bottom sheet which directly touches the substrate is hardly softened on such surfaces as TMC(001) and Pt(111). This is the important difference from that on TMC(111) and Ni surfaces.

7.2. Effect of the interface on the phonon softening

The monolayer graphite is classified into the softened and unsoftened ones from the viewpoint of the phonon structure as mentioned in Chapter 4. As found in the cases of TaC and NbC, even when the substrate is the same material, the overlayer graphite changes with the microscopic structure of the substrate. Ion scattering spectroscopy experiments clarified that a clean (111) surface of the NaCl-type TMC is terminated by metal atoms. On the other hand, metal and carbon atoms sit alternately in the same plane on the (001) surface.[50-54] According to this structural difference, the (111) surface is very active to reaction with gases and rather "metallic" compared with the (001) surface.[88-90] Such chemical properties perhaps perturb the intralayer bonds in the overlayer graphite.

For monolayer graphite on Pt(111), a structure model was proposed by Zi-pu *et al.*[22] They analysed the LEED intensity and concluded adsorbate-like carbon between the graphite layer and the substrate Pt layer. The atomic distance suggests that the adsorbate-like carbon and the first-layer Pt makes some carbidic phase. On the other hand, monolayer graphite on Ni(111) is well established to sit directly on Ni layer.[11] This structural difference probably causes the contrast in phonon structure.

In the case of monolayer graphite on NaCl-type TMC, the interface structure is not yet clear. But when we assume the substrate to keep the same structure after the graphite deposition, the phonon softening gives the same tendency as mentioned above; The monolayer graphite is softened on the "metallic" (111) surfaces but not on the "carbidic" (001) surfaces.

On WC($10\bar{1}0$), most part of the monolayer graphite is softened. However, when the sample is quenched from 1500°C, a small part of the graphite changes unsoftened. Some models are possible as shown in Fig. 7.1; (a) One possibility is double-layer graphite. The first layer is directly attached to the substrate and softened, while the second layer is under

(a) Partially double layered

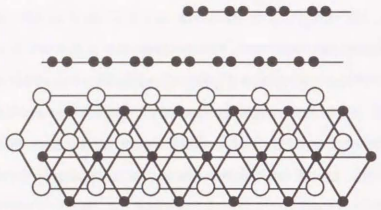

(b) Domain structure in the substrate

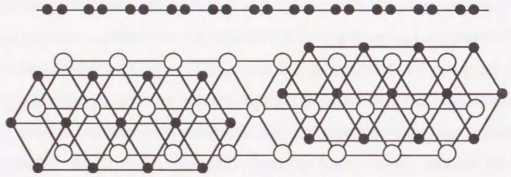

(c) Different interfacial structure caused by the thermal procedures

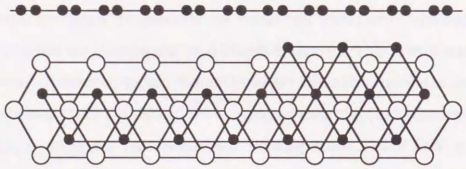

Fig. 7.1 Speculation models of graphite covered WC(10$\bar{1}$0) system.

rather bulk-like environment and should not be softened. (b) Another possibility is due to domains of the substrate. As mentioned in section 3.1.2, the "WC(10$\bar{1}$0)" consists of the two domains of (10$\bar{1}$0) and ($\bar{1}$010). Monolayer graphite on the each domain can show the different phonon structure. However, the dependence on the thermal process is not explained in this model. The interface structure should be different at 1500°C from that at 1300°C in the either domain at least. For example, excess carbon atoms can segregate in the interface at higher or lower temperature. It will partly survive when the temperature is rapidly decreased and makes the different interface structure. This is the other possibility (c). According to the different interfacial structure, different phonon structure will appear.

7.3. Electronic structure of the monolayer graphite

7.3.1. Phonon softening related with the π band shift

As mentioned in section 4.4, the most contrastively affected FC is γ_2. In a graphite sheet, sp^2 hybridized orbital makes the σ bonds in the basal plane and p_z orbital makes the π bonds above and below the plane.[63] Considering this bonding feature in the real space, the π bond should more contribute for FC's related to out-of-plane deformation such as γ_2 and δ than for the other in-plane FC's. From the selective weakening of γ_2, therefore, the following conclusion is deduced; The π bond more interact with the substrate than the σ bond, and it becomes selectively weak.

From the viewpoint of the electronic band structure of monolayer graphite, again, the π band should be firstly affected because it is energetically located around the Fermi level. In fact, the measured electronic band structure shows apparent contrast in the two (phonon-softened and unsoftened) groups. Monolayer graphite having the softened phonon structure has the π band energy about –10 eV at the $\bar{\Gamma}$ point. On the other hand, it is –8 – –9 eV on monolayer graphite having the

unsoftened phonon structure. At first glance, it might sound strange that bonds having greater binding energy is weaker. But this relationship is reasonable in the electronic structure of graphite.

In a pristine graphite sheet, the bonding π band and the antibonding π^* band just connects at the $\overline{K}$ point, at which the Fermi level is located. In the softened monolayer graphite, the binding energy of the π band becomes indeed deeper measured from the Fermi level. But this does not necessarily mean strengthening of the π bond but rather means occupancy of the π^* band which may cause weakening of the π bond. The occupancy of the π^* band is clearly visible in the ARUPS data of monolayer graphite on HfC(111) (Fig. 5.3) for example. The π^* band appears at –2.6 eV at the $\overline{K}$ point and –1.8 eV at the $\overline{M}$ point. Then the π band reaches –3.5 eV at the $\overline{K}$ point and –5.4 eV at the $\overline{M}$ point. The band gap is 3.6 eV at the $\overline{M}$ point and 0.9 eV at the $\overline{K}$ point. As the pristine monolayer should have no gap at the $\overline{K}$ point, the observed gap is an evidence of the interaction with the substrate. Accompanied by this interaction, the π^* band is fairly occupied by electrons, and the Fermi level increases relatively in the band structure. The deepening of the π band is thus explained.

As will be mentioned in the next section, a charge transfer model is often applied in graphite intercalation compounds (GIC's); The host graphite donates/accepts electrons to/from the intercalant without largely changing its band structure. In this model, when electrons are donated into graphite sheet, they occupy inevitably the π^* band, the Fermi level increases and the binding energy measured from the Fermi level becomes uniformly deep. In the monolayer graphite, however, the measured π band drops about 1 eV at the $\overline{\Gamma}$ point, 2–3 eV at the $\overline{M}$ point and 3–4 eV at the $\overline{K}$ point. The shift is not uniform and the band width decreases by 2–3 eV compared with the pristine graphite. Probably this is caused by the lattice expansion and the covalent interaction with the substrate. Such a non-rigid

effect was reported also in LiC_6.[91] The π^* band seems most deformed by the interaction with the substrate. The band is not rigid at all.

Very recently, experimental and theoretical works as for the monolayer graphite on TiC(111) deny large charge-transfer between the graphitic carbon and the substrate metal.[92] Additionally, recent theoretical works deny the complete ionization of the alkaline intercalant in the case of alkaline GIC.[93] They are discussed in section 7.3.3. Thus the simple charge-transfer model is now out of fashion, but still worth discussing because we have several theoretical works dealing with phonon and lattice-constant variations based on the simple charge transfer model. It is discussed in the next section.

7.3.2. Simple charge-transfer model —Comparison with graphite intercalation compounds—

Graphite intercalation compounds (GIC's) have been extensively studied.[4-6] When alkaline metal intercalates, it donates electrons into the graphite host. On the contrary, some ions or molecules such as SO_4^{2-}, $FeCl_3$, Br_2, etc. accept electrons from the host. According to the charge transfer, it is well established from Raman scattering spectroscopy and infrared absorption spectroscopy that boundary layers (graphite layer directly attached to the intercalant) have different vibrational frequency from either pristine graphite or interior layers (graphite layer which is not attached to the intercalant).[4] In these spectroscopy, only zone center modes are detectable. Especially the in-plane vibration corresponding to the LO and the SHO modes in my notation can be clearly observed and has been extensively studied.

Chan *et al.* calculated the phonon frequency from first-principles and discussed the charge transfer effect.[86] Their results showed that the electron-donated graphite layer expands and the phonon frequency

decreases linearly with the charge quantity, while the electron-decreased graphite layer contracts and the phonon frequency increases, in this time, not linearly. In the experimental data, the frequencies of the boundary layer and the interior layer gradually vary with the stage number. They concluded that this shift is caused by the lattice expansion as the secondary effect. The first effect of the charge transfer is restricted in the boundary layer. They calculated the frequency shift caused by the charge transfer within ±0.05 electrons per one carbon atom. In the monolayer graphite on TaC(111), the frequency shift reaches as large as –15 meV (121 cm^{-1}), which is not shown in their graph. Under very rough extrapolation of their graph, the –15 meV shift can be estimated to correspond with the charge transfer of about 0.2 electrons per one carbon atom.

Chan *et al.* also calculated lattice constant change versus charge transfer.[87] From their results, 1 % expansion corresponds to about 0.12 electron donation per one carbon atom. For the 1–3 % expansion of the monolayer graphite, 0.1–0.4 electrons per atom are expected. Considering fairly large error in the LEED estimation, this value well agrees with what expected from the phonon results.

On the other hand, from the viewpoint of electronic band structure, the softened monolayer graphite shows the downward shift of 1–3 eV in the π band. Assuming the rigid band model, energy shift of 1.5 eV corresponds to about 0.1 electrons per atom from the calculated density of states.[102] In fact, the observed π band shows non-rigid-band effect and it is not recommended to estimate the charge transfer from the energy shift. But the order of the transfer might not so much deviate from the true value.

Whole theories discussed above require the electron transfer of 0.1 – 0.3 electrons per one carbon atom to consistently explain the LO phonon softening, lattice expansion and electronic band shift observed in some

monolayer graphite. The necessary charge can come from the substrate. In the case of alkaline GIC, repulsive force between the intercalants restrict the density of intercalants. Accordingly, the transferred charge is 0.16 electrons per atom at most (LiC_6). On the contrary, the substrate under the monolayer graphite makes a lattice by themselves and the atomic density can surpass that of the intercalant in GIC. In fact, the frequency shift of the LO phonon in the monolayer graphite on TaC(111) and on NbC(111) is not less than that of LiC_6. Therefore, in the monolayer graphite system, possibility arises to obtain a new feature of a graphitic layer which has been hidden within the range of charge transfer in GIC.

7.3.3. Mixed band model —Covalent bond formation—

Very recent theoretical work for potassium adsorption on graphite layer[93] reveals that the ionicity of K is not so large when the K density is high. However, the π^* of the graphite layer is moderately occupied, while its σ band occupancy is reduced. This concept of electron redistribution in the adsorbed molecule through the substrate is widely accepted in the molecular adsorption system: for example, CO on metals.[77] The π^* orbital of CO adsorbate interacts with the metal d band and makes a kind of covalent bond. This mixed state has a bonding nature between the molecule and the substrate but antibonding within the molecule. In this mechanism, large electron transfer into the π^* band is possible without largely changing the total charge in the adsorbate. The similar mechanism is expected in the monolayer graphite.

K. Kobayashi *et al.* calculated the electronic structure of the monolayer graphite on TiC(111) by means of discrete variational Xα (DV-Xα) method.[92] As the incommensurate structure is too difficult to be dealt with in the calculation, they enlarged the graphite lattice a little to make the 2×2 periodicity coincide with the $\sqrt{3} \times \sqrt{3}$ (R±30°) lattice of the substrate.

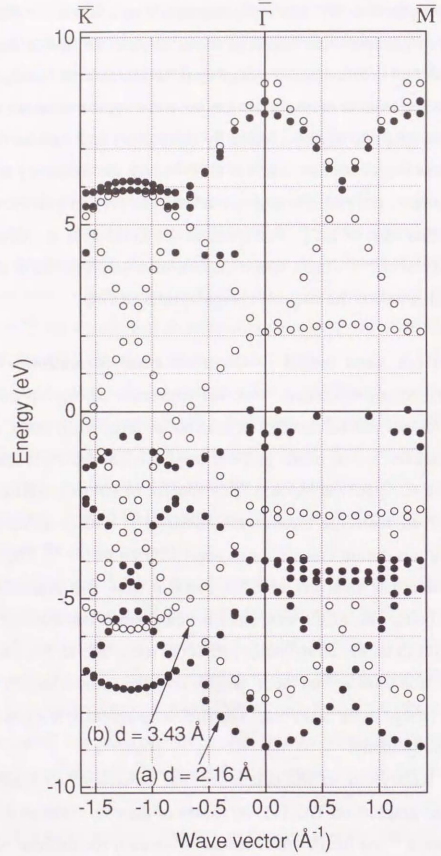

Fig. 7.2 Calculated electronic band structure for monolayer graphite on TiC(111)[92]. The distance between the graphite layer and the substrate Ti layer is (a) d = 2.16 Å and (b) d = 3.43 Å.

They considered the 5 layers slab (one graphite and two Ti and C layers) of that 2×2 lattice. The resultant band structure of the π band is shown in Fig. 7.2. As the unit cell is 2×2, the obtained band structure is expanded in order to compare with the experiment. When the distance between the graphite layer and the substrate Ti layer is as small as in bulk TiC, deepening in the π band energy, narrowing of the π band width, and appearance of the antibonding π^* band near the fermi level are well reproduced in the calculation as shown in Fig. 7.2 (a). Around the Fermi level, the π^* band is considerably mixed with the Ti d-band. When the distance is as large as the interlayer distance in bulk graphite, the band structure is almost the same as free monolayer graphite without substrate [Fig. 7.2 (b)]. Mulliken charge of the graphite layer is, however, scarcely increased from pristine graphite: by 0.01 electrons per one carbon atom even in the case (a). This value is one order less than what is expected in the simple charge transfer model discussed in section 7.3.2. As the Mulliken charge is not shown separately for each orbital, it is not clear whether the σ charge decreases or not. However, the π^* band seems apparently occupied in their band calculation.

A. Nagashima *et al.* measured the monolayer graphite on TiC(111) by ARUPS and XPS.[95,96] The π band energy at the $\bar{\Gamma}$ point was similarly deepened to –9 eV as expected from the phonon softening. However, their XPS shows little chemical shift of C 1s core level in monolayer graphite from that in bulk graphite. They concluded from this fact that the total charge transfer between the graphite and the substrate is very small.

In summary, the π^* band is occupied in the mixed band model as a result of the band mixing with the substrate. Probably this covalent interaction causes relatively large FC values of α_s. It is not important in this model whether the charge transfers or not into the graphite layer as a

total. As the XPS study and the theoretical calculation both deny the large charge transfer expected in the simple charge transfer model, such a total charge transfer is not probable. But in the meaning of charge transfer into the π^* band, it indeed occurs.

7.4. Recent studies for monolayer graphite by other groups

Stimulated by the discovery of the monolayer graphite and its bond softening on the TMC surfaces, some groups recently began studying the monolayer-graphite system experimentally and theoretically. Though the study is now progressing, here let me introduce the recently published results.

7.4.1. Scanning tunneling microscopy (STM) of monolayer graphite on TiC(111)

Graphite is used as a standard material in STM because of its easiness of obtaining a lattice image. In the STM image of pristine graphite, only one atom in the unit cell makes a clear bump, and the image looks like a triangular lattice rather than an expected honeycomb lattice.[97-99] There is the second layer atom below one site but not below the other. This stacking structure and the resultant difference in electronic structure cause the triangular STM image. In the case of monolayer graphite, the stacking structure is completely different, so that it is of great interest to observe the monolayer graphite by STM.

H. Itoh *et al.* have recently challenged this theme;[100] STM investigation of monolayer graphite on TiC(111). In their STM image, the lattice appears in two mixed periodicities of ~5 Å and ~21 Å. These periodicities correspond to the double diffraction spots appearing in the LEED pattern, i.e. the observation is a moire pattern of the two incommensurate lattices: the substrate and the monolayer graphite. Why is only the moire pattern

observed? Why does the graphite lattice itself not appear at all? There are two possibility: One is the modulation in the real atomic structure in the monolayer graphite. The other is the largely modulated electronic structure of the monolayer graphite near the fermi level, the spacial distribution of which is observed in STM. The former is not probable from the viewpoint of the phonon dispersion. If such a modulation occurred in the graphite layer, the interatomic bonds should deviate from the basal plane and the vertical mode such as ZA and ZO modes should be mixed with the horizontal mode LA. In the EELS experiment, no such mixing is detected. Perhaps, some electronic modulation like a charge density wave causes the peculiar STM image. Very recently, such a moire STM image has been reported in monolayer graphite on Pt(111).[101]

The complex STM image shows that the electronic state is not so simple to be described as the rigid band model, at least, near the Fermi level. Simultaneously, it indicates the relatively strong interaction between the substrate and the monolayer graphite. In the next section, the theoretical work concerning this system is briefly reviewed.

7.4.2. Theory of STM image for C/TiC(111) 2×2 system

K. Kobayashi *et al.* calculated the band structure of C/TiC(111) 2×2 system as mentioned in section 7.3.3. Recent theory has clarified that the local density of states (LDOS) at the center of the STM tip is proportional to the conductance of the tunneling current.[102,103] They indicated that the local density of state (LDOS) near the fermi level shows the clear 2×2 pattern in agreement with the short periodicity in the STM image.

7.4.3. Electronic structure calculation of C/Ni(111) by DV-Xα cluster method

K. Yamamoto *et al.* calculated the electronic structure of the

monolayer graphite on Ni(111) by using DV-Xα cluster method.[104] They modeled this system by C_6H_6 on Ni_{10} substrate. Because the monolayer graphite on Ni(111) is commensurate, the adsorption site and height has been clarified experimentally. They found that a bonding orbital between the graphite π^* and the substrate d orbitals appears in occupied states, and resultantly, the charge transfer occurs from the outermost layer of the substrate to the graphite layer. The quantity is about 0.05 electrons per one carbon atom, which is not well enough for the rigid band model. Anyway, they explained the mechanism of π bond softening by the interaction with the substrate.

7.4.4. EELS measurement of two dimensional plasmons in C/TiC(111)

A. Nagashima *et al.* measured the dispersion relations of two plasmon states of the monolayer graphite on TiC(111) by means of EELS.[105] One corresponds with the interband transition and the other with the intraband transition. The dispersions show square root relations, which are characteristic for the two-dimensional electron system. This indicates that the electronic states related with the observed plasmon are indeed localized in the two-dimensional graphite layer. From this point of view, the monolayer graphite system is expected to exhibit a new feature.

7.4.5. ARUPS measurement of monolayer graphite on NbC, ZrC and TiC surfaces

The similar ARUPS measurements for the monolayer graphite on NbC(111), NbC(001),[106] ZrC(111), ZrC(001)[107] and TiC(111)[95,96] were done. The π band is deepened on the (111) surfaces to the similar extent to those on HfC(111) and on TaC(111). The π band on the (001) surfaces is located around at –9 eV, which is also similar to those on HfC(001) and on TaC(001). The correlation of the phonon softening with the π band deepening is again confirmed on these surfaces.

8. Conclusions

In this study, the following have been revealed.

1. A well-ordered graphitic monolayer is produced on some transition-metal carbide surfaces by cracking ethylene.

2. By LEED estimation, the lattice constant of the monolayer graphite is a little expanded on (111) surfaces of NaCl-type TMC and on Ni surfaces.

3. The phonon dispersion relations have been measured by means of HR-EELS. The slightly expanded monolayer graphite mentioned above have softened phonons, especially in the transverse optical mode displaced perpendicularly to the surface.

4. A force constant model is constructed to analyse the phonon dispersion data, and it is found that the vertically bending force constant is most contrastively weakened in the above cases. From the configuration of bonding in the graphite sheet, this weakening indicates the π bond softening.

5. The electronic structure of the monolayer graphite has been measured by means of ARUPS. For the softened monolayer graphite, π band shifts to deeper energy by about 1–2 eV than the unsoftened graphite. In the edge region of the SBZ, occupation of the antibonding state (π^*) is also observed. The phonon softening and the π band deepening apparently correlate with each other.

6. By HR-EELS, molecular (CO and O_2) adsorption is found on the same substrate. On NbC(111), CO stand straightly to the surface, while O_2 is tilted. The intramolecular bond is fairly weakened in both cases.

In the framework of the simple charge transfer model between the substrate and the adsorbate, the observed phonon softening and the π band shift is consistently explained as well as the molecular bond weakening in the adsorbed O_2. On the contrary, recent photoemission and theoretical works prefer the covalent interaction between the substrate and the adsorbate. In this band-mixing model, charge in the adsorbate can be redistributed through the substrate d-band without total ionization. In both models, it is true that the π^* band is moderately occupied, resulting with the characteristic phonon softening and the π band deepening.

Acknowledgements

I deeply appreciate the instruction to EELS study and continuous encouragement by Dr. Chuhei Oshima in National Institute for Research in Inorganic Materials (NIRIM). I also express my great thanks to Dr. Ryutaro Souda, Dr. Shigeki Otani, Dr. Takaho Tanaka and Mr. Wataru Hayami and Dr. Yeon Hwang for a lot of stimulating discussions and collaborations in NIRIM. Dr. Yoshio Ishizawa's encouragement and aids in NIRIM are especially acknowledged. Prof. S. Tanuma of Iwaki Meisei University, Prof. K. Nakao of The University of Tsukuba, Prof. H. Suematsu of The University of Tokyo, and Prof. T. Ichinokawa of Waseda University gave stimulating discussions and are greatly appreciated. I greatly acknowledge the fruitful collaboration on monolayer graphite on Ni surfaces with Prof. K. Tanaka, Dr. T. Yamada and Mr. H. Hirano of The Institute for Solid State Physics (ISSP). I express my thanks to Dr. K. Kobayashi of The University of Tokyo for helpful discussions about the electronic states of the monolayer graphite and informing me his calculation results prior to the publication. I also thanks Mr. H. Itoh and Mr. A. Nagashima of Waseda University for useful discussions and informing me their experimental results prior to the publication. Finally, I deeply appreciate the instruction to surface science and continuous encouragement by Prof. Shozo Ino and Dr. Hiroshi Daimon of The University of Tokyo.

Appendix

A. Calculation of phonon dispersion curves for monolayer graphite

A.1 Potential terms according to the force constant model

According to the here constructed FC model, concrete potential terms in the hamiltonian is calculated as follows. The notation of the atoms are shown in Fig. A.1.

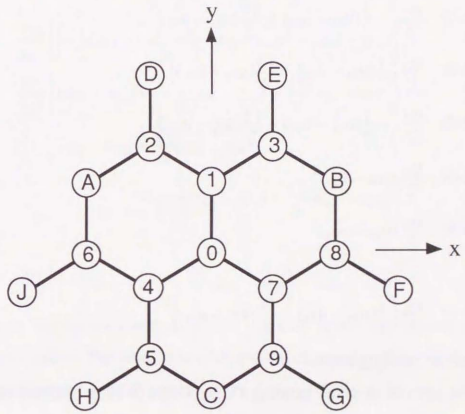

Fig. A.1 Notation of atoms in the force constant model.

(i) Stretching terms

Around the atom 0, three nearest neighbour atoms 1,4 and 7 exist. The terms containing the nearest neighbor stretching FC α_1 and $\mathbf{u}_0$ are;

bond 0–1: $\frac{\alpha_1}{2}(u_{1y}-u_{0y})^2$, (A.1)

bond 0–4: $\frac{\alpha_1}{2}\left|-\frac{\sqrt{3}}{2}(u_{4x}-u_{0x})-\frac{1}{2}(u_{4y}-u_{0y})\right|^2$, (A.2)

and

bond 0–7: $\frac{\alpha_1}{2}\left|\frac{\sqrt{3}}{2}(u_{7x}-u_{0x})-\frac{1}{2}(u_{7y}-u_{0y})\right|^2$. (A.3)

The second nearest atoms are atom 2, 3, 5, 6, 8 and 9. The terms concerning the second nearest neighbor stretching FC α_2 are;

bond 0–2: $\frac{\alpha_2}{2}\left|-\frac{1}{2}(u_{2x}-u_{0x})+\frac{\sqrt{3}}{2}(u_{2y}-u_{0y})\right|^2$, (A.4)

bond 0–3: $\frac{\alpha_2}{2}\left|\frac{1}{2}(u_{3x}-u_{0x})+\frac{\sqrt{3}}{2}(u_{3y}-u_{0y})\right|^2$, (A.5)

bond 0–5: $\frac{\alpha_2}{2}\left|-\frac{1}{2}(u_{5x}-u_{0x})-\frac{\sqrt{3}}{2}(u_{5y}-u_{0y})\right|^2$, (A.6)

bond 0–6: $\frac{\alpha_2}{2}(u_{6x}-u_{0x})^2$, (A.7)

bond 0–8: $\frac{\alpha_2}{2}(u_{8x}-u_{0x})^2$, (A.8)

and

bond 0–9: $\frac{\alpha_2}{2}\left|\frac{1}{2}(u_{9x}-u_{0x})-\frac{\sqrt{3}}{2}(u_{9y}-u_{0y})\right|^2$. (A.9)

(ii) In-plane bending terms

The term of in-plane bending FC γ_1 works to keep constant the angle between nearest neighbor bonds. The terms which contain $\mathbf{u}_0$ are the following nine;

$\angle 012$: $\frac{3\gamma_1}{2a^2}\left[(u_{0x}-u_{1x})-\left\{-\frac{1}{2}(u_{2x}-u_{1x})-\frac{\sqrt{3}}{2}(u_{2y}-u_{1y})\right\}\right]^2$, (A.10)

$\angle 013$: $\frac{3\gamma_1}{2a^2}\left[(u_{0x}-u_{1x})-\left\{-\frac{1}{2}(u_{3x}-u_{1x})+\frac{\sqrt{3}}{2}(u_{3y}-u_{1y})\right\}\right]^2$, (A.11)

$\angle 046$: $\frac{3\gamma_1}{2a^2}\left[\left\{-\frac{1}{2}(u_{0x}-u_{4x})+\frac{\sqrt{3}}{2}(u_{0y}-u_{4y})\right\}-\left\{-\frac{1}{2}(u_{6x}-u_{4x})-\frac{\sqrt{3}}{2}(u_{6y}-u_{4y})\right\}\right]^2$, (A.12)

$\angle 045$: $\frac{3\gamma_1}{2a^2}\left[\left\{-\frac{1}{2}(u_{0x}-u_{4x})+\frac{\sqrt{3}}{2}(u_{0y}-u_{4y})\right\}-(u_{5x}-u_{4x})\right]^2$, (A.13)

$\angle 078$: $\frac{3\gamma_1}{2a^2}\left[\left\{-\frac{1}{2}(u_{0x}-u_{7x})-\frac{\sqrt{3}}{2}(u_{0y}-u_{7y})\right\}-\left\{-\frac{1}{2}(u_{8x}-u_{7x})+\frac{\sqrt{3}}{2}(u_{8y}-u_{7y})\right\}\right]^2$, (A.14)

$\angle 079$: $\frac{3\gamma_1}{2a^2}\left[\left\{-\frac{1}{2}(u_{0x}-u_{7x})-\frac{\sqrt{3}}{2}(u_{0y}-u_{7y})\right\}-(u_{9x}-u_{7x})\right]^2$, (A.15)

$\angle 104$: $\frac{3\gamma_1}{2a^2}\left[(u_{0x}-u_{1x})-\left\{-\frac{1}{2}(u_{0x}-u_{4x})+\frac{\sqrt{3}}{2}(u_{0y}-u_{4y})\right\}\right]^2$, (A.16)

$\angle 407$: $\left[\left\{-\frac{1}{2}(u_{0x}-u_{4x})+\frac{\sqrt{3}}{2}(u_{0y}-u_{4y})\right\}-\left\{-\frac{1}{2}(u_{0x}-u_{7x})-\frac{\sqrt{3}}{2}(u_{0y}-u_{7y})\right\}\right]^2$, (A.17)

and

$\angle 701$: $\frac{3\gamma_1}{2a^2}\left[\left\{-\frac{1}{2}(u_{0x}-u_{7x})-\frac{\sqrt{3}}{2}(u_{0y}-u_{7y})\right\}-(u_{0x}-u_{1x})\right]^2$, (A.18)

where a is the lattice constant of the graphite layer: the second nearest neighbor distance. The nearest neighbor distance equals $a/\sqrt{3}$.

(iii) Out-of-plane bending terms

For the out-of-plane bond bending, the FC γ_2 corresponds. This is the force to keep flat three nearest neighbor bonds connected to one carbon atom. The terms containing $\mathbf{u}_0$ are:

around 1: $\frac{3\gamma_2}{2a^2}(u_{0z}+u_{2z}+u_{3z}-3u_{1z})^2$, (A.19)

around 4: $\frac{3\gamma_2}{2a^2}(u_{0z}+u_{5z}+u_{6z}-3u_{4z})^2$, (A.20)

around 7: $\frac{3\gamma_2}{2a^2}(u_{0z}+u_{8z}+u_{9z}-3u_{7z})^2$, (A.21)

and

around 0: $\frac{3\gamma_2}{2a^2}(u_{1z} + u_{4z} + u_{7z} - 3u_{0z})^2$. (A.22)

(iv) Twisting terms

The potential terms for twisting of the nearest neighbor bonds containing $\mathbf{u}_0$ are:

bond 1–2: $\frac{\delta}{2a^2}\{(u_{3z} - u_{0z}) - (u_{Dz} - u_{Az})\}^2$, (A.23)

bond 1–3: $\frac{\delta}{2a^2}\{(u_{2z} - u_{0z}) - (u_{Ez} - u_{Bz})\}^2$, (A.24)

bond 4–6: $\frac{\delta}{2a^2}\{(u_{5z} - u_{0z}) - (u_{Jz} - u_{Az})\}^2$, (A.25)

bond 4–5: $\frac{\delta}{2a^2}\{(u_{6z} - u_{0z}) - (u_{Hz} - u_{Cz})\}^2$, (A.26)

bond 7–8: $\frac{\delta}{2a^2}\{(u_{9z} - u_{0z}) - (u_{Fz} - u_{Bz})\}^2$, (A.27)

and

bond 7–9: $\frac{\delta}{2a^2}\{(u_{8z} - u_{0z}) - (u_{Gz} - u_{Cz})\}^2$. (A.28)

(v) Interaction term to the substrate

As the interaction to the substrate, the stretching FC α_s is taken into account. This FC works only in the z direction. In the model hamiltonian, the term containing $\mathbf{u}_0$ is only the next one:

$\frac{\alpha_s}{2} u_{0z}^2$. (A.29)

A.2 Dynamical matrix

In the monolayer graphite, the unit cell contains two carbon atoms: 0 and 1 in Fig. A.1. Now one carbon atom 0 is taken as the origin, and the dynamical matrix is calculated:

$M_C D_{0x0x}$

$$= \frac{3\alpha_1}{2} + \frac{\alpha_2}{4}(12 - e^{i\mathbf{r}_{02}\mathbf{k}} - e^{i\mathbf{r}_{03}\mathbf{k}} - 4e^{i\mathbf{r}_{06}\mathbf{k}} - e^{i\mathbf{r}_{05}\mathbf{k}} - e^{i\mathbf{r}_{09}\mathbf{k}} - 4e^{i\mathbf{r}_{08}\mathbf{k}})$$

$$+ \frac{3\gamma_1}{a^2}\left(\frac{15}{2} + \frac{1}{2}e^{i\mathbf{r}_{02}\mathbf{k}} + \frac{1}{2}e^{i\mathbf{r}_{03}\mathbf{k}} - \frac{1}{4}e^{i\mathbf{r}_{06}\mathbf{k}} + \frac{1}{2}e^{i\mathbf{r}_{05}\mathbf{k}} - \frac{1}{4}e^{i\mathbf{r}_{08}\mathbf{k}} + \frac{1}{2}e^{i\mathbf{r}_{09}\mathbf{k}}\right) , \quad (A.30)$$

$$M_C D_{0x0y} = \frac{\sqrt{3}}{4}\alpha_2 (e^{i\mathbf{r}_{02}\mathbf{k}} - e^{i\mathbf{r}_{03}\mathbf{k}} - e^{i\mathbf{r}_{05}\mathbf{k}} + e^{i\mathbf{r}_{09}\mathbf{k}})$$

$$+ \frac{3\gamma_1}{a^2}\left\{\frac{\sqrt{3}}{2}(e^{i\mathbf{r}_{02}\mathbf{k}} - e^{i\mathbf{r}_{03}\mathbf{k}}) + \frac{\sqrt{3}}{4}(e^{i\mathbf{r}_{08}\mathbf{k}} - e^{i\mathbf{r}_{06}\mathbf{k}})\right\} , \quad (A.31)$$

$$M_C D_{0y0y} = \frac{3}{2}\alpha_1 + \frac{3}{4}\alpha_2 (4 - e^{i\mathbf{r}_{02}\mathbf{k}} - e^{i\mathbf{r}_{03}\mathbf{k}} - e^{i\mathbf{r}_{05}\mathbf{k}} - e^{i\mathbf{r}_{09}\mathbf{k}})$$

$$+ \frac{3\gamma_1}{a^2}\left\{\frac{15}{2} + \frac{3}{4}(e^{i\mathbf{r}_{06}\mathbf{k}} + e^{i\mathbf{r}_{08}\mathbf{k}})\right\} , \quad (A.32)$$

$$M_C D_{0y0x} = \frac{\sqrt{3}}{4}\alpha_2 (e^{i\mathbf{r}_{02}\mathbf{k}} - e^{i\mathbf{r}_{03}\mathbf{k}} - e^{i\mathbf{r}_{05}\mathbf{k}} + e^{i\mathbf{r}_{09}\mathbf{k}})$$

$$+ \frac{3\gamma_1}{a^2}\left\{\frac{\sqrt{3}}{2}(e^{i\mathbf{r}_{09}\mathbf{k}} - e^{i\mathbf{r}_{05}\mathbf{k}}) - \frac{\sqrt{3}}{4}(e^{i\mathbf{r}_{08}\mathbf{k}} - e^{i\mathbf{r}_{06}\mathbf{k}})\right\}$$

$$= M_C D^*_{0x0y} , \quad (A.33)$$

$$M_C D_{0x1x} = -\frac{3}{4}\alpha_1 (e^{i\mathbf{r}_{04}\mathbf{k}} + e^{i\mathbf{r}_{07}\mathbf{k}})$$

$$+ \frac{3\gamma_1}{a^2}(-6e^{i\mathbf{r}_{01}\mathbf{k}} - \frac{3}{2}e^{i\mathbf{r}_{04}\mathbf{k}} - \frac{3}{2}e^{i\mathbf{r}_{07}\mathbf{k}}) , \quad (A.34)$$

$$M_C D_{0x1y} = -\frac{3}{4}\alpha_1 (e^{i\mathbf{r}_{04}\mathbf{k}} - e^{i\mathbf{r}_{07}\mathbf{k}}) + \frac{3\gamma_1}{a^2}\frac{3\sqrt{3}}{2}(e^{i\mathbf{r}_{04}\mathbf{k}} - e^{i\mathbf{r}_{07}\mathbf{k}}) , \quad (A.35)$$

$$M_C D_{0y1y} = -\frac{1}{4}\alpha_1 (4e^{i\mathbf{r}_{01}\mathbf{k}} + e^{i\mathbf{r}_{04}\mathbf{k}} + e^{i\mathbf{r}_{07}\mathbf{k}})$$

$$- \frac{3\gamma_1}{a^2}\frac{9}{2}(e^{i\mathbf{r}_{04}\mathbf{k}} + e^{i\mathbf{r}_{07}\mathbf{k}}) , \quad (A.36)$$

$$D_{0y1x} = D_{0x1y} , \quad (A.37)$$

$$M_C D_{0z0z} = \frac{3\gamma_2}{a^2}\,(12 + e^{i\,r_{02}k} + e^{i\,r_{03}k} + e^{i\,r_{05}k} + e^{i\,r_{06}k} + e^{i\,r_{08}k} + e^{i\,r_{09}k}) + \alpha_s$$

$$+ \frac{\delta}{a^2}\,(6 - e^{i\,r_{02}k} - e^{i\,r_{03}k} - e^{i\,r_{05}k} - e^{i\,r_{06}k} - e^{i\,r_{08}k} - e^{i\,r_{09}k})\,, \quad \text{(A.38)}$$

and

$$M_C D_{0z1z} = -\frac{18\gamma_2}{a^2}\,(e^{i\,r_{01}k} + e^{i\,r_{04}k} + e^{i\,r_{07}k})$$

$$+ \frac{\delta}{a^2}\,(e^{i\,r_{0D}k} + e^{i\,r_{0E}k} + e^{i\,r_{0F}k} + e^{i\,r_{0G}k} + e^{i\,r_{0H}k} + e^{i\,r_{0J}k}.$$

$$- 2e^{i\,r_{0A}k} - 2e^{i\,r_{0B}k} - 2e^{i\,r_{0C}k})\,. \quad \text{(A.39)}$$

In order to take the other atom (atom 1) in the unit cell as the origin, think 180° rotation of Fig. A.1. The atom 1 then takes the same position as the atom 0 in the original except that the wave vector $\mathbf{k}_{\parallel}$ is inverted; Namely, the all matrix elements are complex conjugates of the corresponding terms:

$$D_{1x1x} = D_{0x0x}\,, \quad \text{(A.40)}$$

$$D_{1x1y} = D^{*}_{0x0y}\,, \quad \text{(A.41)}$$

$$D_{1y1y} = D_{0y0y}\,, \quad \text{(A.42)}$$

$$D_{1y1x} = D_{0x0y}\,, \quad \text{(A.43)}$$

$$D_{1x0x} = D^{*}_{0x1x}\,, \quad \text{(A.44)}$$

$$D_{1x0y} = D^{*}_{0x1y}\,, \quad \text{(A.45)}$$

$$D_{1y0x} = D^{*}_{0x1y}\,, \quad \text{(A.46)}$$

$$D_{1y0y} = D^{*}_{0y1y}\,, \quad \text{(A.47)}$$

$$D_{1z1z} = D_{0z0z}\,, \quad \text{(A.48)}$$

$$\text{and } D_{1z0z} = D^{*}_{0z1z}\,. \quad \text{(A.49)}$$

The other matrix elements are all zero.

A.3 Phonon dispersion curves along $\overline{\Gamma}$–$\overline{M}$ axis

Considering the phonon dispersion curves along $\overline{\Gamma} - \overline{M}$ direction, k_x equals zero and k_y moves from 0 to $\frac{\pi}{a\cos 30°}$. Namely, the sagittal plane is y-z plane. When k_x becomes zero, D_{0x0y} and D_{0x1y} become always zero, and the dynamical matrix separates into three parts; The first one is $\begin{pmatrix} D_{0x0x} & D_{0x1x} \\ D_{1x0x} & D_{1x1x} \end{pmatrix}$ where

$$D_{0x0x} = D_{1x1x}$$

$$= \frac{1}{M_C}\left\{\frac{3}{2}\alpha_1 + \alpha_2(1 - \cos\frac{\sqrt{3}}{2}ak_y) + \frac{3\gamma_1}{a^2}\,(7 + 2\cos\frac{\sqrt{3}}{2}ak_y)\right\} \quad \text{(A.50)}$$

and

$$D_{0x1x} = D^{*}_{1x0x}$$

$$= \frac{1}{M_C}\left[-\frac{3}{2}\alpha_1 \exp\left(-i\,\frac{\sqrt{3}}{6}ak_y\right) - \frac{9\gamma_1}{a^2}\left\{2\exp\left(i\,\frac{ak_y}{\sqrt{3}}\right) + \exp\left(-i\,\frac{\sqrt{3}}{6}ak_y\right)\right\}\right]. \quad \text{(A.51)}$$

This 2×2 hermite matrix determines the dispersion of x-displaced modes: shear horizontal (SH) modes. The eigen value is given as:

$$\omega^2_{SH} = D_{0x0x} \pm |\,D_{0x1x}\,|\,. \quad \text{(A.52)}$$

The second part $\begin{pmatrix} D_{0y0y} & D_{0y1y} \\ D_{1y0y} & D_{1y1y} \end{pmatrix}$ consists of:

$$D_{0y0y} = D_{1y1y} = \frac{1}{M_C}\left\{\frac{3}{2}\alpha_1 + 3\alpha_2(1 - \cos\frac{\sqrt{3}}{2}ak_y) + \frac{27\gamma_1}{a^2}\right\} \quad \text{(A.53)}$$

and $D_{0y1y} = D^{*}_{1y0y}$

$$= \frac{1}{M_C}\left[-\frac{1}{2}\alpha_1\left\{2\exp\left(i\,\frac{ak_y}{\sqrt{3}}\right) + \exp\left(-i\,\frac{\sqrt{3}}{6}ak_y\right)\right\} - \frac{27\gamma_1}{a^2}\exp\left(-i\,\frac{\sqrt{3}}{6}ak_y\right)\right]. \quad \text{(A.54)}$$

This part determines the dispersion of the longitudinal (L) modes:

$$\omega^2_{L} = D_{0y0y} \pm |\,D_{0y1y}\,|\,. \quad \text{(A.55)}$$

The last part $\begin{pmatrix} D_{0z0z} & D_{0z1z} \\ D_{1z0z} & D_{1z1z} \end{pmatrix}$, where

$D_{0z0z} = D_{1z1z}$

$$= \frac{1}{M_C}\left\{\frac{3\gamma_2}{a^2}(14 + 4\cos\frac{\sqrt{3}}{2}ak_y) + \alpha_s + \frac{4\delta}{a^2}(1 - \cos\frac{\sqrt{3}}{2}ak_y)\right\} \quad \text{(A.56)}$$

and $D_{0z1z} = D^*_{1z0z} = \frac{1}{M_C}\left[-\frac{18\gamma_2}{a^2}\left\{\exp\left(i\frac{ak_y}{\sqrt{3}}\right) + 2\exp\left(-i\frac{\sqrt{3}}{6}ak_y\right)\right\}\right.$

$$\left. + \frac{2\delta}{a^2}\left\{\exp\left(i\frac{5\sqrt{3}}{6}ak_y\right) + \exp\left(-i\frac{ak_y}{2\sqrt{3}}\right) - 2\exp\left(i\frac{ak_y}{\sqrt{3}}\right)\right\}\right], \quad \text{(A.57)}$$

determines dispersion relations of the z-displaced (Z) modes, and its frequency is:

$$\omega^2_Z = D_{0z0z} \pm |D_{0z1z}| . \quad \text{(A.58)}$$

A.4 Phonon dispersion curves along $\bar{\Gamma}$–$\bar{K}$–$\bar{M}$ axis

When we consider the phonon dispersion curve along $\bar{\Gamma}$–$\bar{K}$–$\bar{M}$ direction, put k_y zero and move k_x from 0 to $4\pi / 3a$ ($\bar{K}$) and $2\pi / a$ ($\bar{M}$). The dynamical matrix separates into two parts; The first one is

$$\begin{pmatrix} D_{0x0x} & D_{0x0y} & D_{0x1x} & D_{0x1y} \\ D_{0y0x} & D_{0y0y} & D_{0y1x} & D_{0y1y} \\ D_{1x0x} & D_{1x0y} & D_{1x1x} & D_{1x1y} \\ D_{1y0x} & D_{1y0y} & D_{1y1x} & D_{1y1y} \end{pmatrix} , \quad \text{(A.59)}$$

where

$$D_{0x0x} = \frac{1}{M_C}\left\{\frac{3}{2}\alpha_1 + \alpha_2(3 - \cos\frac{ak_x}{2} - 2\cos ak_x) + \frac{3\gamma_1}{2a^2}(15 + 4\cos\frac{ak_x}{2} - \cos ak_x)\right\} , \quad \text{(A.60)}$$

$$D_{0x0y} = \frac{1}{M_C}\frac{3\gamma_1 i}{2a^2}(-2\sqrt{3}\sin\frac{ak_x}{2} + \sqrt{3}\sin ak_x) , \quad \text{(A.61)}$$

$$D_{0y0y} = \frac{1}{M_C}\left\{\frac{3}{2}\alpha_1 + 3\alpha_2(1 - \cos\frac{ak_x}{2}) + \frac{3\gamma_1}{2a^2}(15 + 3\cos ak_x)\right\} , \quad \text{(A.62)}$$

$$D_{0x1x} = \frac{1}{M_C}\left\{-\frac{3}{2}\alpha_1\cos\frac{ak_y}{2} + \frac{9\gamma_1}{a^2}(-2 - \cos\frac{ak_y}{2})\right\} , \quad \text{(A.63)}$$

$$D_{0x1y} = \frac{1}{M_C}(\frac{\sqrt{3}}{2}\alpha_1 i\sin\frac{ak_x}{2} - \frac{9\sqrt{3}\gamma_1 i}{a^2}\sin\frac{ak_x}{2}) , \quad \text{(A.64)}$$

$$D_{0y1y} = \frac{1}{M_C}\left\{-\frac{1}{2}\alpha_1(2 + \cos\frac{ak_x}{2}) - \frac{27\gamma_1}{a^2}\cos\frac{ak_x}{2}\right\} . \quad \text{(A.65)}$$

The other matrix elements are given in (A.33), (A.37) and (A.40)–(A.47). Diagonalyzing this dynamical matrix gives four xy-displaced modes. They are:

$$\omega^2 = \frac{1}{2M_C}[2\alpha_1 + 6\alpha_2 + 63g_1 + (\alpha_1 - 4\alpha_2 - 12g_1)\cos\frac{ak_x}{2} + (-2\alpha_1 + 3g_1)\cos ak_x \pm\{\alpha_1^2 + 36\alpha_1 g_1 + 324g_1^2 + (4\alpha_1^2 + 4\alpha_1\alpha_2 + 156\alpha_1 g_1 + 72\alpha_2 g_1 + 1512g_1^2)\cos\frac{ak_x}{2} + (4\alpha_1^2 + 8\alpha_1\alpha_2 + 4\alpha_2^2 + 168\alpha_1 g_1 + 168\alpha_2 g_1 + 1764g_1^2)\cos^2\frac{ak_x}{2} + (-4\alpha_1\alpha_2 - 12\alpha_1 g_1 - 72\alpha_2 g_1 - 216g_1^2)\cos ak_x + (-8\alpha_1\alpha_2 - 8\alpha_2^2 - 24\alpha_1 g_1 - 192\alpha_2 g_1 - 504g_1^2)\cos\frac{ak_x}{2}\cos ak_x + (4\alpha_2^2 + 24\alpha_2 g_1 + 36g_1^2)\cos^2 ak_x + (3\alpha_1^2 - 144\alpha_1 g_1 + 1728g_1^2)\sin^2\frac{ak_x}{2} + (18\alpha_1 g_1 - 432g_1^2)\sin\frac{ak_x}{2}\sin ak_x + 27g_1^2\sin^2 ak_x\}^{1/2}] \quad \text{(A.66)}$$

and

$$\omega^2 = \frac{1}{2M_C}\left[4\alpha_1 + 6\alpha_2 + 27g_1 - (\alpha_1 + 4\alpha_2 - 24g_1)\cos\frac{ak_x}{2}\right.$$
$$+ (-2\alpha_1 + 3g_1)\cos ak_x$$
$$\pm\{\alpha_1^2 + 36\alpha_1 g_1 + 324 g_1^2$$
$$+ (4\alpha_1^2 - 4\alpha_1\alpha_2 + 132\alpha_1 g_1 - 72\alpha_2 g_1 + 1080 g_1^2)\cos\frac{ak_x}{2}$$
$$+ (4\alpha_1^2 - 8\alpha_1\alpha_2 + 4\alpha_2^2 + 120\alpha_1 g_1 - 120\alpha_2 g_1 + 900 g_1^2)\cos^2\frac{ak_x}{2}$$
$$+ (4\alpha_1\alpha_2 + 12\alpha_1 g_1 + 72\alpha_2 g_1 + 216 g_1^2)\cos ak_x$$
$$+ (8\alpha_1\alpha_2 - 8\alpha_2^2 + 24\alpha_1 g_1 + 96\alpha_2 g_1 + 360 g_1^2)\cos\frac{ak_x}{2}\cos ak_x$$
$$+ (4\alpha_2^2 + 24\alpha_2 g_1 + 36 g_1^2)\cos^2 ak_x + (3\alpha_1^2 - 72\alpha_1 g_1 + 432 g_1^2)\sin^2\frac{ak_x}{2}$$
$$\left.+ (-18\alpha_1 g_1 + 216 g_1^2)\sin\frac{ak_x}{2}\sin ak_x + 27 g_1^2 \sin^2 ak_x\}^{1/2}\right] . \qquad (A.67)$$

Here, $g_1 = \gamma_1 / a^2$.

The other part is $\begin{pmatrix} D_{0z0z} & D_{0z1z} \\ D_{1z0z} & D_{1z1z} \end{pmatrix}$, where

$$D_{0z0z} = D_{1z1z} = \frac{1}{M_C}\left\{\frac{3\gamma_2}{a^2}(12 + 4\cos\frac{ak_x}{2} + 2\cos ak_x) + \alpha_s \right.$$
$$\left. + \frac{\delta}{a^2}(6 - 4\cos\frac{ak_x}{2} - 2\cos ak_x)\right\} \qquad (A.68)$$

and

$$D_{0z1z} = D^*_{1z0z} = \frac{1}{M_C}\left\{-\frac{18\gamma_2}{a^2}(1 + 2\cos\frac{ak_x}{2})\right.$$
$$\left. + \frac{2\delta}{a^2}(-1 + \cos\frac{ak_x}{2} - \cos ak_x + \cos\frac{3ak_x}{2})\right\} , \qquad (A.69)$$

which determines dispersion relations of the z-displaced modes. Its frequency is:

$$\omega^2_Z = D_{0z0z} \pm |D_{0z1z}| . \qquad (A.70)$$

B. Construction of a dynamical matrix of monolayer graphite on Ni(111) slab

In this appendix, expression of the dynamical matrix for the slab configuration is presented.[60] A unit cell of the slab model contains two carbon atoms in the graphite layer and one Ni atom in every substrate layer. At first, let me express the dynamical matrix as follows:

$$\begin{pmatrix} C_1C_1 & C_1C_2 & C_1N_1 & C_1N_2\cdots \\ C_2C_1 & C_2C_2 & C_2N_1 & C_2N_2\cdots \\ N_1C_1 & N_1C_2 & N_1N_1 & N_1N_2\cdots \\ N_2C_1 & N_2C_2 & N_2N_1 & N_2N_2\cdots \\ & & \vdots & \end{pmatrix} . \qquad (B.1)$$

Each element is a 3×3 small matrix as follows:

$$AB = \begin{pmatrix} D_{AxBx} & D_{AxBy} & D_{AxBz} \\ D_{AyBx} & D_{AyBy} & D_{AyBz} \\ D_{AzBx} & D_{AzBy} & D_{AzBz} \end{pmatrix} . \qquad (B.2)$$

Here C_1 and C_2 means the two carbon atoms in the unit cell and N_n expresses the Ni atom in the n-th substrate layer.

Without the interaction $\alpha_{C\text{-}Ni}$, the left-upside of (B.1) is the same as in the model defined in Chapter 4. In the substrate, only the nearest neighbor stretching FC α_{Ni} is considered. Namely, the potential energy of one bond i-j is:

$$\Phi = \frac{\alpha_{Ni}}{2}\{\mathbf{t}_{ij}\cdot(\mathbf{u}_j - \mathbf{u}_i)\}^2 , \qquad (B.3)$$

where $\mathbf{t}_{ij} = (\mathbf{r}_j - \mathbf{r}_i) / |\mathbf{r}_j - \mathbf{r}_i|$. Accordingly, every considering the nearest neighbor pair, add

$$\begin{pmatrix} \frac{\partial\Phi}{\partial u_{ixix}} & \frac{\partial\Phi}{\partial u_{ixiy}} & \frac{\partial\Phi}{\partial u_{ixiz}} \\ \frac{\partial\Phi}{\partial u_{iyix}} & \frac{\partial\Phi}{\partial u_{iyiy}} & \frac{\partial\Phi}{\partial u_{iyiz}} \\ \frac{\partial\Phi}{\partial u_{izix}} & \frac{\partial\Phi}{\partial u_{iziy}} & \frac{\partial\Phi}{\partial u_{iziz}} \end{pmatrix} = \alpha_{Ni}\begin{pmatrix} t_x^2 & t_xt_y & t_xt_z \\ t_xt_y & t_y^2 & t_yt_z \\ t_xt_z & t_yt_z & t_z^2 \end{pmatrix} \qquad (B.4)$$

to N_lN_l and N_mN_m and add

$$\begin{pmatrix} \frac{\partial\Phi}{\partial u_{ixjx}} & \frac{\partial\Phi}{\partial u_{ixjy}} & \frac{\partial\Phi}{\partial u_{ixjz}} \\ \frac{\partial\Phi}{\partial u_{iyjx}} & \frac{\partial\Phi}{\partial u_{iyjy}} & \frac{\partial\Phi}{\partial u_{iyjz}} \\ \frac{\partial\Phi}{\partial u_{izjx}} & \frac{\partial\Phi}{\partial u_{izjy}} & \frac{\partial\Phi}{\partial u_{izjz}} \end{pmatrix} \exp(i\mathbf{k}\cdot\mathbf{r}_{ij})$$

$$= -\alpha_{Ni}\begin{pmatrix} t_x^2 & t_xt_y & t_xt_z \\ t_xt_y & t_y^2 & t_yt_z \\ t_xt_z & t_yt_z & t_z^2 \end{pmatrix} \exp(i\mathbf{k}\cdot\mathbf{r}_{ij}) \qquad \text{(B.5)}$$

to N_lN_m and its complex conjugate to N_mN_l if the atom i and j are in the neighbored layer, l and m, respectively. If the pairing atoms are in the same layer l, add

$$\alpha_{Ni}\begin{pmatrix} t_x^2 & t_xt_y & t_xt_z \\ t_xt_y & t_y^2 & t_yt_z \\ t_xt_z & t_yt_z & t_z^2 \end{pmatrix} \{1 - \exp(i\mathbf{k}\cdot\mathbf{r}_{ij})\} \qquad \text{(B.6)}$$

to N_lN_l. Considering the 12 nearest neighbor bonds in the FCC crystal, the resultant dynamical matrix becomes as follows;

N_lN_l. equals

$$\alpha_{Ni}\begin{pmatrix} \frac{1}{2} + 2\,(1\text{-}\cos ak_x) & \sqrt{3}\,\sin a\frac{k_x}{2}\sin a\frac{\sqrt{3}}{2}k_y & 0 \\ \quad + (1 - \cos a\frac{k_x}{2}\cos a\frac{\sqrt{3}}{2}k_y) & & \\ \frac{\sqrt{3}}{2}\,\sin a\frac{k_x}{2}\sin a\frac{\sqrt{3}}{2}k_y & \frac{1}{2} + 3(1 - \cos a\frac{k_x}{2}\cos a\frac{\sqrt{3}}{2}k_y) & 0 \\ 0 & 0 & 2 \end{pmatrix}, \qquad \text{(B.7)}$$

N_iN_i $(i \geq 2)$ becomes

$$\alpha_{Ni}\begin{pmatrix} 1 + 2\,(1\text{-}\cos ak_x) & \sqrt{3}\,\sin a\frac{k_x}{2}\sin a\frac{\sqrt{3}}{2}k_y & 0 \\ \quad + (1 - \cos a\frac{k_x}{2}\cos a\frac{\sqrt{3}}{2}k_y) & & \\ \frac{\sqrt{3}}{2}\,\sin a\frac{k_x}{2}\sin a\frac{\sqrt{3}}{2}k_y & 1 + 3(1 - \cos a\frac{k_x}{2}\cos a\frac{\sqrt{3}}{2}k_y) & 0 \\ 0 & 0 & 4 \end{pmatrix}, \qquad \text{(B.8)}$$

and N_iN_{i-1} $(i \geq 2)$ becomes

$$\alpha_{Ni}\begin{pmatrix} -\frac{1}{2}\cos\frac{ak_x}{2}e^{ia\frac{k_y}{2\sqrt{3}}} & -\frac{i}{2\sqrt{3}}\sin\frac{ak_x}{2}e^{ia\frac{k_y}{2\sqrt{3}}} & -\frac{2i}{\sqrt{3}}\sin\frac{ak_x}{2}e^{ia\frac{k_y}{2\sqrt{3}}} \\ -\frac{i}{2\sqrt{3}}\sin\frac{ak_x}{2}e^{ia\frac{k_y}{2\sqrt{3}}} & -\frac{1}{6}\cos\frac{ak_x}{2}e^{ia\frac{k_y}{2\sqrt{3}}} - \frac{1}{3}e^{-ia\frac{k_y}{\sqrt{3}}} & -\frac{\sqrt{2}}{3}\cos\frac{ak_x}{2}e^{ia\frac{k_y}{2\sqrt{3}}} + \frac{\sqrt{2}}{3}e^{-ia\frac{k_y}{\sqrt{3}}} \\ -\frac{2i}{\sqrt{3}}\sin\frac{ak_x}{2}e^{ia\frac{k_y}{2\sqrt{3}}} & -\frac{\sqrt{2}}{3}\cos\frac{ak_x}{2}e^{ia\frac{k_y}{2\sqrt{3}}} + \frac{\sqrt{2}}{3}e^{-ia\frac{k_y}{\sqrt{3}}} & -\frac{4}{3}\cos\frac{ak_x}{2}e^{ia\frac{k_y}{2\sqrt{3}}} - \frac{2}{3}e^{-ia\frac{k_y}{\sqrt{3}}} \end{pmatrix}. \qquad \text{(B.9)}$$

$N_{i-1}N_i$ is the complex conjugate of N_iN_{i-1}. The other N_iN_j are all zero.

When $\alpha_{C\text{-}Ni}$ is taken into account, according to the similar procedure, we add

$$\frac{\alpha_{C\text{-}Ni}}{\frac{a^2}{3} + d^2}\begin{pmatrix} \frac{a^2}{2} & 0 & 0 \\ 0 & \frac{a^2}{2} & 0 \\ 0 & 0 & 3d^2 \end{pmatrix} \qquad \text{(B.10)}$$

to C_lC_l and C_2C_2, and two times of (B.10) to N_lN_l. C_lN_l becomes

$$\frac{\alpha_{C\text{-}Ni}}{\frac{a^2}{3} + d^2}\begin{pmatrix} -\frac{a^2}{2}\cos\frac{ak_x}{2}e^{-ia\frac{k_y}{2\sqrt{3}}} & \frac{a^2i}{2\sqrt{3}}\sin\frac{ak_x}{2}e^{-ia\frac{k_y}{2\sqrt{3}}} & -adi\sin\frac{ak_x}{2}e^{-ia\frac{k_y}{2\sqrt{3}}} \\ \frac{a^2i}{2\sqrt{3}}\sin\frac{ak_x}{2}e^{-ia\frac{k_y}{2\sqrt{3}}} & -\frac{a^2}{6}\cos\frac{ak_x}{2}e^{-ia\frac{k_y}{2\sqrt{3}}} - \frac{a^2}{3}e^{ia\frac{k_y}{\sqrt{3}}} & \frac{ad}{\sqrt{3}}(\cos\frac{ak_x}{2}e^{-ia\frac{k_y}{2\sqrt{3}}} - e^{ia\frac{k_y}{\sqrt{3}}}) \\ -adi\sin\frac{ak_x}{2}e^{-ia\frac{k_y}{2\sqrt{3}}} & \frac{ad}{\sqrt{3}}(\cos\frac{ak_x}{2}e^{-ia\frac{k_y}{2\sqrt{3}}} - e^{ia\frac{k_y}{\sqrt{3}}}) & -d^2(2\cos\frac{ak_x}{2}e^{-ia\frac{k_y}{2\sqrt{3}}} + e^{ia\frac{k_y}{\sqrt{3}}}) \end{pmatrix} \qquad \text{(B.11)}$$

and C_2N_l becomes

$$\frac{\alpha_{C\text{-}Ni}}{\frac{a^2}{3}+d^2}\begin{pmatrix} -\frac{a^2}{2}\cos\frac{ak_x}{2}e^{i\,a\frac{k_y}{2\sqrt{3}}} & -\frac{a^2 i}{2\sqrt{3}}\sin\frac{ak_x}{2}e^{i\,a\frac{k_y}{2\sqrt{3}}} & -adi\sin\frac{ak_x}{2}e^{i\,a\frac{k_y}{2\sqrt{3}}} \\ -\frac{a^2 i}{2\sqrt{3}}\sin\frac{ak_x}{2}e^{i\,a\frac{k_y}{2\sqrt{3}}} & -\frac{a^2}{6}\cos\frac{ak_x}{2}e^{i\,a\frac{k_y}{2\sqrt{3}}}-\frac{a^2}{3}e^{-i\,a\frac{k_y}{\sqrt{3}}} & -\frac{ad}{\sqrt{3}}(\cos\frac{ak_x}{2}e^{i\,a\frac{k_y}{2\sqrt{3}}}-e^{-i\,a\frac{k_y}{\sqrt{3}}}) \\ -adi\sin\frac{ak_x}{2}e^{i\,a\frac{k_y}{2\sqrt{3}}} & -\frac{ad}{\sqrt{3}}(\cos\frac{ak_x}{2}e^{i\,a\frac{k_y}{2\sqrt{3}}}-e^{-i\,a\frac{k_y}{\sqrt{3}}}) & -d^2(2\cos\frac{ak_x}{2}e^{i\,a\frac{k_y}{2\sqrt{3}}}+e^{-i\,a\frac{k_y}{\sqrt{3}}}) \end{pmatrix}. \tag{B.12}$$

N_1C_1 and N_1C_2 are the complex conjugate of C_1N_1 and C_2N_1, and all the other matrix elements are zero in this model. Here, a and d denote the two-dimensional lattice constant and the interlayer distance between graphite and substrate, respectively. In the calculation, values of a = 2.49 Å and d = 2.80 Å are used.

List of published papers

[1] T. Aizawa, R. Souda, S. Otani, Y. Ishizawa and C. Oshima, "Anomalous Bond of Monolayer Graphite on Transition-Metal Carbide Surfaces", Phys. Rev. Lett. **64**, 768 (1990).

[2] T. Aizawa, R. Souda, S. Otani, Y. Ishizawa and C. Oshima, "Bond softening in monolayer graphite formed on transition-metal carbide surfaces", Phys. Rev. B **42**, 11469 (1990). (Erattum: Phys. Rev. B **43**, 12060 (1991).

[3] T. Aizawa, R. Souda, Y. Ishizawa, H. Hirano, T. Yamada and C. Oshima, "Phonon dispersion in monolayer graphite formed on Ni(111) and Ni(001)", Surf. Sci. **237**, 194 (1990).

[4] T. Aizawa, Y. Hwang, W. Hayami, R. Souda, S. Otani and Y. Ishizawa, "Phonon dispersion of monolayer graphite on Pt(111) and NbC surfaces: bond softening and interface structures", Surf. Sci. **260**, 311 (1992).

[5] 相澤　俊, 「単原子層グラファイト」, 表面科学**11**, 398 (1990).

[6] 相澤　俊, 石沢芳夫, 「遷移金属炭化物表面上の単原子層グラファイトとフィールドエミッターへの応用」, 炭素 **155**, 335 (1992).

References

1) C. L. Mantell, "*Carbon and Graphite Handbook*" (Interscience Publishers, John Wiley & Sons, New York, 1968).

2) H. W. Kroto, J. R. Heath,.S. C. Brien, R. F. Curl and R. E. Smalley, Nature **318**, 162 (1985).

3) S. Iijima, Nature **354**, 56 (1991).

4) M. S. Dresselhaus and G. Dresselhaus, Advan. Phys. **30**, 139 (1981).

5) 渡辺信淳 編著 "グラファイト層間化合物" (近代編集社 1986).

6) H. Zabel and S. A. Solin (eds.), "Graphite Intercalation Compounds I" (Springer Verlag, Berlin Heidelberg 1990).

7) J. P. Coad and J. C. Rivière, Surf. Sci. **25**, 609 (1971).

8) M. Eizenberg and J. M. Blakely, Surf. Sci. **82**, 228 (1979).

9) D. W. Goodman, R. D. Kelley, T. E. Madey and J. T. Yates, Jr. J. Catal. **63**, 226 (1980).

10) R. Rosei, S. Modesti, F. Sette, C. Quaresima, A. Savoia and P. Perfetti, Solid State Commun. **46**, 871 (1983).

11) R. Rosei, M. De Crescinzi, F. Sette, C. Quaresima, A. Savoia and P. Perfetti, Phys. Rev. B **28**, 1161 (1983).

12) L. Papagno and S. Caputi, Phys. Rev. B **29**, 1483 (1984).

13) R. Rosei, S. Modesti, F. Sette, C. Quaresima, A. Savoia and P. Perfetti, Phys. Rev. B **29**, 3416 (1984).

14) C. F. McConville, D. P. Woodruff and S. D. Kevan, Surf. Sci. **171**, L447 (1986).

15) L. Papagno, M. Conti, L. S. Caputi, J. Anderson and G. J. Lapeyre, Surf. Sci. **219**, L565 (1989).

16) J. Nakamura, H. Hirano, M. Xie, I. Matsuo, T. Yamada and K. Tanaka, Surf. Sci. **222**, L809 (1989).

17) J. C. Hamilton and J. M. Blakely, Surf. Sci. **91**, 199 (1980).

18) D. G. Castner, B. A. Sexton and G. A. Somorjai, Surf. Sci. **71**, 519 (1978).

19) F. J. Himpsel, K. Chrisstmann, P. Heimann, D. E. Eastman and P. J. Feibelman, Surf. Sci. **115**, L159 (1982).

20) N. A. Kholin, E. V. Rut'kov and A. Y. Tontegode, Surf. Sci. **139**, 155 (1984).

21) N. R. Gall', S. N. Mikhaĭlov, E. V. Rut'kov and A. Ya. Tontegode, Fiz. Tverd. Tela (Leningrad) **27**, 2351 (1985) [Sov. Phys. Solid State **27**, 1410 (1985)].

22) H. Zi-pu, D. F. Ogletree, M. A. Van Hove and G. A. Somorjai, Surf. Sci. **180**, 433 (1987).

23) F. M. Propst and Th. C. Piper, J. Vac. Sci. Technol. **4**, 53 (1967).

24) H. Ibach, J. Vac. Sci. Technol. **9**, 713 (1971).

25) H. Ibach and D. L. Mills, "*Electron Energy Loss Spectrocvopy and Surface Vibrations*" (Academic Press, New York, 1982).

26) S. Andersson, Solid State Commun. **20**, 229 (1976).

27) S. Andersson, Surf. Sci. **79**, 385 (1979).

28) W. Ho, J. Vac. Sci. Technol. **A 3**, 1432 (1985).

29) B. A. Gurney, W. Ho, L. J. Richter and J. S. Villarrubia, Rev. Sci. Instrum. **59**, 22 (1988).

30) H. Ibach, "*Electron Energy Loss Spectrometers - The Technology of High Performance*", (Springer Verlag, Berlin Heidelberg 1991).

31) H. Ibach, M. Balden, D. Bruchmann and S. Lehwald, Surf. Sci. **269/270**, 94 (1992).

32) C. Oshima, R. Franchy and H. Ibach, Rev. Sci. Instrum. **54**, 1042 (1983).

33) C. Oshima, R. Souda, M. Aono and Y. Ishizawa, Rev. Sci. Instrum. **56**, 227 (1985).

34) R. Nicklow, N. Wakabayashi and H. G. Smith, Phys. Rev. B **5**, 4951 (1972).

35) G. Benedek, G. Brusdeylins, C. Heimlich, J. P. Toennies and U. Valbusa, Surf. Sci. **178**, 545 (1986).

36) R. J. Nemalich, G. Lucovky and S. A. Splin, Solid State Commun. **23**, 117 (1977).

37) Y. Sato, J. Phys. Soc. Japan **24**, 489 (1968).

38) F. Tuinstra and J. L. Koenig, J. Chem. Phys. **53**, 1126 (1970).

39) C. Oshima, T. Aizawa, R. Souda, Y. Ishizawa and Y. Sumiyoshi, Solid State Commun. **65**, 1601 (1988).

40) J. L. Wilkes, R. E. Palmer and R. F. Willis, J. Elec. Spectr. Rel. Phen. **44**, 355 (1987).

41) Y. Ishizawa, M. Koizumi, C. Oshima and S. Otani, J. Physique **48**, C6-9 (1987), Y. Ishizawa, S. Aoki, C. Oshima and S. Otani, J. Phys. D: Appl. Phys. **22**, 1763 (1989), Y. Ishizawa, T. Aizawa and S. Otani, Appl. Surf. Sci. **67**, 36 (1993).

42) D. Roy and J.-D. Carette, Can. J. Phys. **49**, 2138 (1971).

43) P. Bryce, R. L. Dalglish and J. C. Kelly, Can. J. Phys. **51**, 574 (1973).

44) W. Steckelmacher, J. Phys. E: Sci. Instrum. **6**, 1061 (1973).

45) L. E. Toth, "*Transition Metal Carbides and Nitrides*" (Academic Press, New York, 1971).

46) S. Otani and T. Tanaka, J. Cryst. Growth **51**, 381 (1981).

47) S. Otani, T. Tanaka and Y. Ishizawa, J. Cryst. Growth **55**, 431 (1981).

48) S. Otani, S. Honma, T. Tanaka and Y. Ishizawa, J. Cryst. Growth **61**, 1 (1983).

49) S. Otani, T. Tanaka, Y. Ishizawa, J. Cryst. Growth **97**, 522 (1989).

50) C. Oshima, M. Aono, T. Tanaka, S. Kawai, S. Zaima and Y. Shibata, Surf. Sci. **102**, 312 (1981).

51) M. Aono, C. Oshima, S. Zaima, S. Otani and Y. Ishizawa, Jpn. J. Appl. Phys. **21**, L670 (1982).

52) R. Souda, T. Aizawa, S. Otani and Y. Ishizawa, Surf. Sci. **232**, 219 (1990).

53) W. Hayami, R. Souda, T. Aizawa, S. Otani and Y. Ishizawa, Surf. Sci. **276**, 299 (1992).

54) W. Hayami, R. Souda, T. Aizawa, S. Otani and Y. Ishizawa, Phys. Rev. B **47**, 13752 (1993).

55) T. Tanaka, S. Otani and Y. Ishizawa, J. Material Sci. **23**, 665 (1988).

56) P. M. Stefan, M. L. Shek, I. Lindau, W. E. Spicer, L. I. Johansson, F. Herman, R. V. Kasowski and G. Brogen, Phys. Rev. B **29**, 5423 (1984).

57) L. Rayleigh, Proc. London Math. Soc. **17**, 4 (1887).

58) R. F. Wallis, Phys. Rev. **105**, 540 (1957).

59) C. Oshima, R. Souda, M. Aono, S. Otani and Y. Ishizawa, Phys. Rev. Lett. **56**, 240 (1986).

60) R. E. Allen, G. P. Alldredge and F. W. de Wette, Phys. Rev. B **4**, 1648 (1971).

61) M. Maeda, Y. Kuramoto and C. Horie, J. Phys. Soc. Japan **47**, 337 (1979).

62) E. de Rouffignac, G. P. Alldredge and F. W. de Wette, Phys. Rev. B **23**, 4208 (1981).

63) S. Lehwald, F. Wolf, H. Ibach, B. M. Hall and D. L. Mills, Surf. Sci. **192**, 131 (1987).

64) E. W. Plummer and W. Eberhardt, Adv. Chem. Phys. **49**, 533 (1982).

65) A. R. Law, J. J. Barry and H. P. Hughes, Phys. Rev. B **28**, 5332 (1983).

66) T. Takahashi, H. Tokailin and T. Sagawa, Solid State Commun. **52**, 765 (1984).

67) T. Takahashi, H. Tokailin and T. Sagawa, Phys. Rev. B **32**, 8317 (1985).
68) J.-C. Charlier, X. Gonze and J.-P. Michenaud, Phys. Rev. B **43**, 4579 (1991), and references therein.
69) J. C. Bertolini, G. Dalmai-Imelik and J. Rousseau, Surf. Sci. **68**, 539 (1977).
70) J. C. Campuzano and R. G. Greenler, Surf. Sci. **83**, 301 (1979).
71) W. Erly, H. Ibach, S. Lehwald and H. Wagner, Surf. Sci. **83**, 585 (1979).
72) J. C. Bertolini and B. Tardy, Surf. Sci. **102**, 131 (1981).
73) R. Maruca, T. Kusuma, V. Hicks and A. Companion, Surf. Sci. **236**, 210 (1990), and references therein.
74) C. E. Bartosch, L. J. Whitman and W. Ho, J. Chem. Phys. **85**, 1052 (1986).
75) P. B. Merrill and R. J. Madix, Surf. Sci. **271**, 81 (1992).
76) N. D. Shinn and T. E. Madey, Phys. Rev. Lett. **53**, 2481 (1984).
77) G. Blyholder, J. Phys. Chem. **68**, 2772 (1964) and J. Phys. Chem. **79**, 756(1975).
78) R. A. dePaola, J. Hrbek and F. M. Hoffmann, J. Chem. Phys. **82**, 2484 (1985).
79) L. Zhu, S. Bao, C. Y. Xu and Y. B. Xu, Surf. Sci. **260**, 267 (1992).
80) H. P. Bonzel, J. Vac. Sci. Technol. **A 2**, 866 (1984).
81) J. L. Gland, B. A. Sexton and G. B. Fisher, Surf. Sci. **95**, 587 (1980).
82) B. A. Sexton and R. J. Madix, Chem. Phys. Lett. **76**, 294 (1980).
83) N. D. Shinn and T. E. Madey, Surf. Sci. **176**, 635 (1986), and references therein.
84) M. Hammar, C. Törnevik, J. Rundgren, Y. Gauthier, S. A. Flodström, K. L. Håkansson, L. I. Johansson and J. Häglund, Phys. Rev. B **45**, 6118 (1992).

85) C. Oshima, M. Aono, S. Otani and Y. Ishizawa, Solid State Commun. **48**, 911 (1983).
86) C. T. Chan, K. M. Ho and W. A. Kamitakahara, Phys. Rev. B **36**, 3499 (1987).
87) C. T. Chan, W. A. Kamitakahara, K. M. Ho and P. C. Eklund, Phys. Rev. Lett. **58**, 1528 (1987).
88) C. Oshima, M. Aono, S. Zaima, Y. Shibata and S. Kawai, J. Less-Common Met. **82**, 69 (1981).
89) I. Kojima, M. Orita, E. Miyazaki and S. Otani, Surf. Sci. **160**, 153 (1985).
90) K. Edamoto, T. Anazawa, E. Shiobara, M. Hatta, E. Miyazaki, H. Kato and S. Otani, Phys. Rev. B **43**, 3871 (1991).
91) W. Eberhardt, I. T. McGovern, E. W. Plummer and J. E. Fisher, Phys. Rev. Lett. **44**, 200 (1980).
92) F. Ancilotto and F. Toigo, Phys. Rev. B **47**, 13713 (1993).
93) K. Kobayashi, Y. Souzu, N. Isshiki and M. Tsukada, Appl. Surf. Sci. **60/61**, 443 (1992).
94) S. B. Trickey, F. Müller-Plathe, G. H. F. Diercksen and J. C. Boettger, Phys. Rev. B **45**, 4460 (1992).
95) A. Nagashima, K. Nuka, H. Itoh, T. Ichinokawa, S. Otani, Y. Ishizawa, H. Kasamura, M. Kudo and C. Oshima, 表面科学 **13**, 163 (1992).
96) A. Nagashima, K. Nuka, H. Itoh, T. Ichinokawa, C. Oshima and S. Otani, Surf. Sci. **291**, 93 (1993).
97) G. Binnig, H. Fuchs, Ch. Gerber, H. Rohrer, E. Stoll and E. Tosatti, Europhys. Lett. **1**, 31 (1986).
98) D. Tomanek, S. G. Louie, Phys. Rev. B **37**, 8327 (1988).
99) S. Gwo and C. K. Shih, Phys. Rev. B **47**, 13059 (1993) and references therein.

100) H. Itoh, T. Ichinose, C. Oshima, T. Ichinokawa and T. Aizawa, Surf. Sci. **254**, L437 (1991).

101) T. A. Land, T. Michely, R. J. Behm, J. C. Hemminger and G. Comsa, Surf. Sci. **264**, 261 (1992).

102) J. Tersoff and D. R. Hamann, Phys. Rev. B **31**, 805 (1985).

103) M. Tsukada and N. Shima, J. Phys. Soc. Jpn. **56**, 2875 (1987).

104) K. Yamamoto, M. Fukushima, T. Osaka and C. Oshima, Phys. Rev. B **45**, 11358 (1992).

105) A. Nagashima, K. Nuka, H. Itoh, T. Ichinokawa, C. Oshima, S. Otani and Y. Ishizawa, Solid State Comunn. **83**, 581 (1992).

106) Y. Hwang, T. Aizawa, W. Hayami, S. Otani, Y. Ishizawa and S. J. Park, Solid State Commun. **81**, 397 (1992).

107) Y. Hwang, T. Aizawa, W. Hayami, S. Otani, Y. Ishizawa and S. J. Park, Surf. Sci. **271**, 299 (1992).